NASA TECHNICAL NOTE

NASA TN D-8187

WING-SURFACE—JET INTERACTION CHARACTERISTICS OF AN UPPER-SURFACE BLOWN MODEL WITH RECTANGULAR EXHAUST NOZZLES AND A RADIUS FLAP

Alvin M. Bloom, William C. Hohlweg, and William C. Sleeman, Jr.

Langley Research Center
Hampton, Va. 23665

NATIONAL AERONAUTICS AND SPACE ADMINISTRATION • WASHINGTON, D. C. • DECEMBER 1976

1. Report No.	2. Government Accession No.	3. Recipient's Catalog No.
NASA TN D-8187		

4. Title and Subtitle
WING-SURFACE—JET INTERACTION CHARACTERISTICS OF AN UPPER-SURFACE BLOWN MODEL WITH RECTANGULAR EXHAUST NOZZLES AND A RADIUS FLAP

5. Report Date
December 1976

6. Performing Organization Code

7. Author(s)
Alvin M. Bloom, William C. Hohlweg, and William C. Sleeman, Jr.

8. Performing Organization Report No.
L-10410

10. Work Unit No.
505-10-41-03

9. Performing Organization Name and Address
NASA Langley Research Center
Hampton, VA 23665

11. Contract or Grant No.

13. Type of Report and Period Covered
Technical Note

12. Sponsoring Agency Name and Address
National Aeronautics and Space Administration
Washington, DC 20546

14. Sponsoring Agency Code

15. Supplementary Notes
Alvin M. Bloom and William C. Hohlweg: The George Washington University.
William C. Sleeman, Jr.: Langley Research Center.

16. Abstract

An investigation of the wing-surface—jet interaction characteristics of an upper-surface blown transport configuration was conducted in the Langley V/STOL tunnel. Velocity profiles at the inboard engine center line were measured for several chordwise locations, and chordwise pressure distributions on the flap were obtained. The model used in this investigation represented a four-engine arrangement having relatively high-aspect-ratio rectangular spread exhaust nozzles and a simple trailing-edge radius flap.

17. Key Words (Suggested by Author(s))
Powered-lift aerodynamics
Upper-surface blowing
Jet flows

18. Distribution Statement
Unclassified – Unlimited
Subject Category 02

19. Security Classif. (of this report)	20. Security Classif. (of this page)	21. No. of Pages	22. Price*
Unclassified	Unclassified	80	$4.75

* For sale by the National Technical Information Service, Springfield, Virginia 22161

WING-SURFACE—JET INTERACTION CHARACTERISTICS OF AN UPPER-SURFACE BLOWN MODEL WITH RECTANGULAR EXHAUST NOZZLES AND A RADIUS FLAP

Alvin M. Bloom,* William C. Hohlweg,* and William C. Sleeman, Jr.
Langley Research Center

SUMMARY

An investigation of the wing-surface—jet interaction characteristics of an upper-surface blown transport configuration was conducted in the Langley V/STOL tunnel. The model used in this investigation represented a four-engine arrangement having relatively high-aspect-ratio rectangular spread exhaust nozzles and a simple trailing-edge radius flap.

Test results, obtained in surveys of velocity profiles at the inboard engine center line for several chordwise locations, indicated no velocity decay or jet thickening from the nozzle exit to the flap. However, some velocity decay and thickening of the jet did occur downstream of the flap knee. Two-dimensional flow separation points on the radius flap were estimated by the Stratford method from chordwise pressure distributions on the flap. These estimates showed good agreement, at the highest jet exit velocities, with the three-dimensional static turning angles obtained from force data.

INTRODUCTION

Considerable research attention has been given recently to the use of powered lift to improve the landing and take-off performance of transport aircraft. Most of these powered-lift concepts use turbofan engine exhaust as a source of high-energy flow that interacts with the airplane wing and high-lift flap system to produce very high lift coefficients. The upper-surface blown (USB) powered-lift concept impinges the exhaust flow on the wing upper surface by use of a suitably shaped nozzle, located well forward on the wing upper surface. Powered lift on USB configurations is obtained by Coanda turning of the attached flow over a properly shaped, trailing-edge, high-lift flap. Recent emphasis on noise reduction for all transport aircraft has led to increased interest in the upper-surface blown concept because the wing partially shields the ground flyover plane from the noise radiated by the engine exhaust.

---

*The George Washington University.

Recent wind-tunnel research investigations of USB powered-lift configurations have demonstrated the potential for achieving very good powered-lift performance (refs. 1 to 4). The results of these investigations showed that a variety of nozzle-wing-flap configurations could be tailored to achieve good static turning of the exhaust flows and good aerodynamic performance; however, the problem of defining optimal nozzle-flap parameters has not been addressed. The details of nozzle and flap design parameters have implications in other areas such as structures and noise as well as low-speed aerodynamics; therefore, some understanding of the design requirements in these related areas is needed. For example, the noise-shielding effect of the wing was found to increase with nozzle aspect ratio only if the flow run length from the exit to the flap trailing edge was suitably long (ref. 5). These acoustic results may be considered to imply that the jet velocity at the flap trailing edge must be sufficiently decayed so that the strength of the trailing-edge noise source is suitably small.

The present lack of parametric design information on nozzle-wing-flap relationships for good aerodynamic performance highlights the need for gaining an understanding of the flow mechanisms of jet velocity decay and aerodynamic turning of the exhaust flow of upper-surface blown configurations. The present investigation was undertaken, therefore, to study the wing-surface—jet interaction characteristics of a nozzle-wing-flap USB configuration and to determine the jet-turning-angle and jet-velocity variations from the nozzle exit to the flap trailing edge. These tests were an extension of the aerodynamic performance work reported in reference 4.

The model used in this investigation was a general research model that had been previously tested with pylon-mounted nacelles in a conventional under-the-wing engine installation to represent both externally blown flap (ref. 6) and deflected-thrust (ref. 7) powered-lift concepts. The present model represented a four-engine upper-surface blown transport configuration having rectangular-shaped exhaust nozzles that spread the exhaust flow over the upper surface of the wing.

Tests were conducted in the Langley V/STOL tunnel, and most of the data were obtained from a survey rake that measured the jet velocity profiles along the engine center line at several chordwise locations from the nozzle exit to the rear part of the 90° radius flap. Surface pressures over the radius flap were also measured after tests with the survey rake. Data were obtained over a range of thrust coefficients for static (no tunnel flow) and wind-on conditions with the model at angles of attack of 0°, 8°, and 16°. Aerodynamic tests with the wind on were conducted at a dynamic pressure of 766 Pa, and the test Reynolds number was 7.02×10^5, based on the wing mean aerodynamic chord of 0.2899 m.

SYMBOLS

Measurements and calculations were made in the U.S. Customary Units. They are presented in the International System of Units (SI) except in the table and the data figures where they are given in both systems for additional information. The reference axis system for the force data taken on the model is given in figure 1.

C_D drag coefficient, $\frac{\text{Drag}}{qS}$

C_L lift coefficient, $\frac{\text{Lift}}{qS}$

C_p pressure coefficient based on jet velocity, $\frac{p - p_\infty}{\frac{1}{2}\rho U_{exit}^2}$

C_μ thrust coefficient, $\frac{\text{Thrust}}{qS}$

h nozzle height, cm

l distance from nozzle exit to knee of flap, cm

p static pressure on upper surface of radius flap, Pa

p_t total pressure, Pa

$p_{t,a}$ atmospheric total pressure, Pa

p_∞ free-stream static pressure, Pa

q free-stream dynamic pressure, Pa

R radius of radius flap, cm

S wing area, m^2

T thrust, N

U jet velocity, m/sec

x axial coordinate measured downstream of nozzle exit, cm

y normal coordinate measured from surface of wing or flap, cm

$y_{1/2}$ jet half-height (distance from wing or flap surface to height for which jet velocity decreased to 1/2 of maximum), cm

α angle of attack of fuselage reference line, deg

Δ_j jet static separation angle, deg

δ_f radius-flap deflection angle (included angle of the sector between the tangent point on the wing and the trailing edge), deg (see fig. 3)

δ_j jet static turning angle, $\tan^{-1} \frac{\text{Normal force}}{\text{Axial force}}$, deg

η jet static thrust-recovery efficiency, $\sqrt{\frac{(\text{Resultant force})^2}{(\text{Thrust force})^2}}$

ρ air density, kg/cm^3

χ internal roof angle of nozzle exit, deg

Subscripts:

exit nozzle exit

max maximum

ref reference value at nozzle exit plane

MODEL AND APPARATUS

Model Description

The model used in this investigation was the same model that was tested in the investigation of reference 4 with the 90^o radius flap (figs. 2 and 3) and the rectangular nozzles. A drawing and general description of the model are given in figure 2(a), and details of nacelles and exhaust nozzles are given in figure 2(b). A photograph of the model configuration tested in the present investigation is shown in figure 2(c). The model wing had an aspect ratio of 7.48 and a leading-edge sweep angle of 33.6^o. The high-lift system consisted of a 15-percent-chord leading-edge slat that extended across the wing span from the side of the fuselage (12.7 percent semispan) to the wing tip, except between the nacelles, and a 90^o radius flap that extended from the side of the fuselage to approximately 70.4 percent of the wing semispan. The radius flap was tangent to the upper

surface of the wing along the 75.5-percent-chord line. Deflections of the radius flap were defined as the included angle of the sector between the tangent point on the wing and the trailing edge. The arc length of the radius flap was 47.1 percent of the local wing chord and the radius of the flap was 30 percent of the local wing chord of the basic planform.

The engine nacelles were mounted on the wing upper surface in a manner that would provide attached engine exhaust flow over the midchord sections of the wing ahead of the flaps. The relatively high internal roof angle of 23° at the nozzle exit provided impingement of the exhaust flow on the wing surface. Engine flow simulation was provided by four separately mounted air ejectors connected to a high-pressure air supply. The engine nacelle center lines were located at 25.4 and 41.7 percent of the wing semispan. Each engine simulator had two individual air supply lines from the fuselage plenum and control valves to permit simulation of the exhaust-flow characteristics of turbofan engines. Only the outer flow from the fan section was used in the present tests; there was no primary flow through the gas-generator section of the engine simulator. Early tests of the model in the investigation of reference 4 revealed appreciable external flow separation of the spread flow from the inboard nozzles, which impinged on the side of the outboard nozzle. This flow-separation problem was alleviated by the addition of wedges in the inboard nozzles, which eliminated the side flare as shown in figure 2(b). These wedges were in place for the present investigation.

All survey-rake data for the present investigation were obtained at different chordwise stations from the nozzle exit downstream (fig. 3(a)) in the vertical plane of the inboard nacelle center line. The various geometric parameters applicable to the model at the spanwise location of the survey rakes were as follows: the distance l from the nozzle exit to the knee of the flap was 14.54 cm, the flap radius r was 9.94 cm, and the nozzle height was 2.77 cm. The nozzle width with the internal wedge installed was 15.68 cm, which provided a nozzle aspect ratio (width-height ratio) of 5.66. The numerical definitions of the survey-rake stations are given in table I.

Apparatus

A schematic drawing of the survey rake is shown in figure 4. The rake consisted of 25 total-pressure tubes and 2 static-pressure tubes. The total-pressure tubes were nominally 0.076 cm in diameter, and the static-pressure tubes were 0.15 cm in diameter with spherical end caps. The static-pressure tubes were located 8 tube diameters from the nose and in line with the total-pressure tubes. Pressure tubes 1 to 5 were spaced 0.05 cm apart, tubes 6 to 17 were spaced 0.25 cm apart, and tubes 18 to 27 were spaced 0.10 cm apart. These spacing dimensions were set before each test and checked at the end of the test, and some differences were frequently observed, depending upon the test conditions and the location of the rake on the model. The spacing dimensions given are

therefore considered to be nominal values, particularly for tests at high thrust. Static-pressure tubes 6 and 17 were used to determine the static pressure in the external flow and in the jet flow, respectively.

The radius flap was instrumented with 20 static-pressure tubes 0.10 cm in diameter and approximately equal distances apart. Standard scanner-valve instrumentation was used to acquire the surface-pressure data for both the survey rake and radius flap.

The model was mounted on a variable-angle support sting. The geometric angle of attack of the model was obtained from an electronic angle-of-attack sensor mounted inside the model fuselage.

TESTS AND CORRECTIONS

The investigation was conducted in the Langley V/STOL tunnel. Aerodynamic tests were conducted at a dynamic pressure of 766 Pa, and the test Reynolds number was 7.02×10^5, based on the wing mean aerodynamic chord of 0.2899 m. Tests were conducted at angles of attack of 0°, 8°, and 16°.

Thrust Calibrations

Static-thrust calibrations made for the tests of reference 4 were used in the present investigation. All static-thrust calibrations were made with the engines installed on the model and with the wing flaps and trailing edge aft of the 75.5-percent-chord line removed. Static-thrust calibrations for all four engines together were made after the thrusts of the individual engines were calibrated and balanced, based on the individual engine calibrations and the net yawing moment of the model with all engines operating. The static thrust from the calibrations was computed as the resultant of the normal and axial forces. The stated thrust and thrust coefficients for this investigation were determined from summation of the static thrust for the individual engines which was based on engine reference pressures recorded at each data point. The assumption was made that the static-thrust calibrations were applicable to the wind-on test conditions for computing the thrust coefficients. Relationships between jet exit velocity, thrust, and thrust coefficient at $q = 766$ Pa are shown in figure 5.

Test Procedure

The model was positioned in the wind tunnel at the desired angle of attack with the survey rake in position. Data were obtained at a constant angle of attack at various values of thrust, first with the wind off for static data and then with the wind on at

$q = 766$ Pa $(16\ lb/ft^2)$ for the forward-speed data. This procedure was repeated for each rake position and angle of attack and was repeated with the rake removed for the flap pressure distributions.

Corrections

Jet-boundary corrections for the influence of the closed tunnel boundaries were determined from reference 8 and applied to the measured force data presented herein. The customary corrections to the free-stream dynamic pressure were applied for the present tests.

PRESENTATION OF DATA

The results obtained in this investigation are given in the figures as follows:

DISCUSSION

Static Turning Characteristics

Static turning angles and static thrust-recovery efficiencies obtained in the test of reference 4 are given in figure 6 for different radius-flap deflections, including the 90° deflection used in the present investigation. The static turning angles show very little

variation with increasing thrust above about 450 N for all flap deflections. This characteristic and the relatively high and invariant level of thrust-recovery efficiency suggest that the jet flow from the rectangular nozzles was fairly well stabilized over the radius flap, even though the full turning that was expected for the indicated deflections was not achieved. The jet turning angles for the radius flap were about two-thirds of the flap deflection angle for all flap deflections; for example, about 60° turning was obtained with the 90° flap deflection. This level of turning suggests that the jet flow always detached from the radius flap ahead of the flap trailing edge. These separation characteristics are discussed later in the section "Flap Surface Pressure Distributions."

Lift and Drag Coefficients Over Angle-of-Attack Range

Aerodynamic force data obtained over the angle-of-attack range for the model with rectangular nozzles and the 90° radius flap, as determined from the tests of reference 4, are presented in figure 7. The lift and drag coefficients of figure 7 are presented to define the aerodynamic conditions covered in the present investigation. The survey-rake data obtained at angles of attack of 0° and 8° were on the linear part of the lift curves for power-on conditions, whereas data obtained at $\alpha = 16^{\circ}$ were in regions of decreased lift-curve slope, indicative of some flow separation on the wing. Although these separation effects were most pronounced for the power-off and low-thrust conditions, the power-on test results show that even for the high-thrust conditions a progressive reduction in lift-curve slope occurred at high angles of attack. The implications that these different angle-of-attack regimes have on the survey-rake data are discussed in the next section.

Jet Total-Pressure and Velocity Profiles

The basic survey-rake data obtained in this investigation are presented in figures 8 to 11 as the variation of the difference between jet total pressure and atmospheric total pressure $(p_t - p_{t,a})$ and of the corresponding jet velocities U with the perpendicular distance above the wing or flap surface. The velocity profiles presented in figures 8 to 11 were calculated from the measured total-pressure profiles according to the procedures given in the appendix. These basic data were obtained at each chordwise survey station for a range of engine thrust settings. Values of U_{exit} given in the key of each data figure were arithmetic averages of the velocity profiles at the nozzle exit because the nozzle exit velocity profiles showed sizable nonuniformities across the jet height, especially at the high-thrust settings. These nonuniformities are associated with the engine simulator characteristics; the smaller irregularities in pressure that occurred in the jet, at heights below about 0.25 cm for high-thrust conditions (figs. 8(c) and 9(a)), can be attributed to scatter in the fluctuating pressures.

Static jet characteristics.- Total-pressure and velocity profiles for the static jet are presented in figure 8 for each of the various survey-rake stations, from the nozzle exit (fig. 8(a)) to the rearmost position on the flap (fig. 8(j)). The pressure and velocity profiles obtained over the wing (figs. 8(a) to 8(e)) were of similar shape as the survey position progressed downstream, with the maximum velocity in the jet remaining at about 240 m/sec for the highest exit velocity. Total pressures for the first five stations over the wing (figs. 8(a) to 8(e)) and outside the jet were equal to the free-stream value $(p_t - p_{t,a} = 0)$; however, the velocity outside the jet reflects the induced flow around the nacelle. The jet flow continued to spread vertically as the downstream distance increased over the flap and the peak velocities decreased slightly.

Jet characteristics with free-stream flow.- Total-pressure and velocity profiles for the jet, with the tunnel flow on, are presented in the same manner as the static jet characteristics. Profiles obtained with the model at angles of attack of 0°, 8°, and 16° are presented in figures 9, 10, and 11, respectively. The jet-flow characteristics obtained in the presence of the free-stream flow were so similar to those of the static jet that only the most obvious differences associated with addition of free-stream flow and variations in angle of attack are mentioned at this point.

The presence of the free-stream flow was fairly pronounced inside the jet region at low thrust and, of course, with power off as evidenced by the higher velocities with free-stream flow. (For example, compare figs. 8(a) and 9(a) at $\alpha = 0^\circ$.) Increasing the angle of attack had very little effect on the velocity profiles within the jet region with the wind on (figs. 9 to 11). Outside the jet, an expected increase in velocity was evident with the tunnel flow on and the model at 0° angle of attack (figs. 8 and 9). Increasing the angle of attack with the tunnel flow on, however, caused irregularities in the profiles outside the jet and decreased the velocities as the angle of attack increased to 16° (figs. 9 to 11) for stations just downstream of the nacelle. Negative total-pressure differences were also indicated for these survey stations and reflect the presence of the wake behind the inboard nacelle at the higher angles of attack. For survey stations farther downstream, beginning at the flap knee (fig. 11(f)), the negative total-pressure differences and the reduced velocities outside the jet tended to approach the values obtained at lower angles of attack, which indicates a favorable entrainment effect of the jet on the high-angle-of-attack flow field outside the jet.

Nondimensional Velocity Profiles

A two-dimensional wall jet can be considered to consist of two different basic flow regions, the initial region and the main region. In the initial region, the wall jet develops from a flat type of profile with no decay of the maximum jet velocity experienced, as was

shown for static conditions at the five survey stations just downstream of the nozzle (figs. 8(a) to 8(e)). Velocity profiles for the next downstream station at the flap knee (x = 14.83 cm, fig. 8(f)) and for stations farther downstream (figs. 8(g) to 8(j)) showed a distinctly different shape, which resembles the profile for fully developed wall jet flow. This flow profile is similar to the Glauert profile (ref. 9) and is usually referred to as the main region. In the main region of the jet flow, the velocity profiles become similar with respect to an appropriate length and reference velocity in the jet. Parameters selected for nondimensionalizing the present jet surveys are the maximum jet velocity and the jet half-height $y_{1/2}$. The jet half-height is defined as the distance from the wing or flap surface to the height at which the jet velocity decreases to 50 percent of the maximum velocity. These normalizing parameters generally vary with downstream distance from the nozzle.

Effect of jet exit velocity.- Selected portions of the basic data of figures 8, 9, and 11 have been normalized with respect to the maximum jet velocity and jet half-height for both the static jet and the jet with free-stream flow at angles of attack of 0° and 16° for chordwise locations in both the initial and main regions of the jet flow. These normalized results are presented in figures 12 to 15 for three values of jet exit velocity. The profiles for the static jet were generally reduced to essentially one normalized curve both inside and outside the jet, with some irregularities shown just outside the jet; these irregularities can be attributed to turbulent mixing (figs. 12 and 13). Velocity profiles of the jet with free-stream flow were essentially collapsed to one normalized curve inside the jet for all angles of attack and survey stations included in figures 12 to 15; however, effects of the free-stream flow and angle of attack were evident outside the jet, particularly for survey stations in the initial flow region (figs. 12 and 13). The profiles that were normalized at 0° angle of attack with free-stream flow did not show the irregularities associated with turbulent mixing that were generally evident in the static profiles. The normalized results at 16° angle of attack, however, showed appreciable irregularities and changes in the overall level of normalized velocity outside the jet for the survey stations downstream of the nozzle (fig. 13) and at the flap knee (fig. 14). The irregularities and change in velocity are believed to be associated with effects of the wake from the nacelle at the fairly high angle of attack of 16°. Profiles at the rearmost survey station (fig. 15) indicated that the velocities outside the jet increased appreciably over the values obtained at the flap knee (fig. 14) at 16° angle of attack. This increase occurred because the attached jet flow accelerated the flow outside the jet as it passed over the curved surface of the radius flap. It is interesting to observe that the normalizing parameters used to obtain the nondimensional profiles provided a good description of the velocity profiles that were essentially independent of the exit velocity, even at the rearmost survey station.

Effect of survey-rake location.- The nondimensional velocity profiles presented in figures 12 to 15 have been regrouped to illustrate the effects of survey-rake location at three values of jet exit velocity and are presented in figures 16 to 18. The data of figures 16 to 18 show that the wall jet was not fully developed until the two rearmost survey stations were reached. Outside the jet, the velocity profiles for the different survey stations were influenced predominantly by the free-stream flow and angle-of-attack effects (figs. 17 and 18) with the wind on, and by variations in turbulent mixing at the various downstream survey positions for the static jet (fig. 16). Within the initial jet flow region (x = 0 and 6.63 cm), effects of jet thickening are evident as the survey rake is moved from the jet exit (x = 0 cm) to the first downstream position (x = 6.63 cm). Inside the jet, the profiles obtained in the initial region (x = 6.63 cm) showed a transition to the Glauert profile, with the maximum velocity occurring at a lower height in the jet as the survey station moved downstream from the exit (figs. 16 to 18).

An overall assessment of the nondimensional velocity profiles indicates that inside the jet, the normalizing parameters that were used provided a very good description of the flow in the main flow region and in the initial flow region, except at the jet edge, where thickening effects were appreciable. Outside the jet, the normalizing parameters did not account for free-stream or flow separation effects.

Jet Velocity Decay and Thickness Characteristics

The previous discussion of jet characteristics has been concerned with the velocity characteristics through the jet in a plane normal to the local wing or flap surface and along the jet center line. The jet thickness and velocity decay characteristics along the jet axis are also of interest in defining and understanding the jet flow field. Nondimensional velocities in the jet as a function of a nondimensional distance downstream of the jet exit were derived from the basic data of figures 8, 9, and 11 and are presented in figures 19 and 20. The normalizing parameter used for the jet velocity decay was the reference velocity at the jet exit U_{ref}. Distances along the jet axis were nondimensionalized by the jet exit height h, and jet thickness characteristics were nondimensionalized by the jet half-height at the exit. Results are presented for the static jet and the jet with the free-stream flow at angles of attack of 0° and 16° for representative low- and high-jet-exit-velocity conditions (figs. 19 and 20).

Jet velocity decay.- The jet-velocity-decay results presented in figures 19(a) and 20(a) show that the maximum jet velocity for static (wind-off) conditions remained almost constant from the jet exit (x/h = 0) to the flap knee (x/h = 5.41) and then showed about 12-percent decay between the flap knee and the rearmost survey location (x/h = 8.0). Addition of the free-stream flow at 0° angle of attack resulted in little change in

maximum velocity from the jet exit to the flap knee, followed by a slight increase in velocity as the flow passed over the flap knee. This higher level of U_{max} over the flap with the wind on (figs. 19(a) and 20(a)) is attributed to the lower static pressure imposed by the free stream and the flow turning over the curved surface of the flap. In contrast, the characteristics with the wind on at 16° angle of attack showed a velocity decay of about 25 percent as the flow progressed from the flap knee (x = 5.41 cm) to the rear survey station (x = 8.0 cm) at the lower jet exit velocity presented (fig. 19(a)). At the higher jet exit velocity (fig. 20(a)), the decay was somewhat less at the rear survey station. The appreciable velocity decay at 16° angle of attack can probably be attributed to the increased static pressures associated with separated flow at the high angle of attack. However, the nondimensional velocity profiles of figure 15 suggest some static-pressure recovery at the rear survey station by the increase in velocity outside the jet in comparison with corresponding velocities at the flap knee.

Jet thickness.- Jet thickness characteristics are given in figures 19(b) and 20(b) for the same test conditions as for the jet-velocity-decay results. The effective jet thickness $y_{1/2}/y_{1/2,exit}$ for the static jet showed a general decrease from a value of unity at the nozzle exit to a value of about 0.92 at the flap knee (x/h = 5.41). Downstream of the flap knee the jet began to thicken as it passed over the flap and reached a maximum of about 20-percent thickening at the rear survey station. The relatively high internal roof angle of the nozzle provided good jet flow impingement on the wing surface and caused the jet to thin in the region of the flap knee. The thinning of the jet ahead of the flap knee had a beneficial effect on flow turning over the flap, and as the flow was turned by the flap, the jet began to thicken.

With the wind on at 0° angle of attack, the jet thinned appreciably as it progressed from the nozzle exit to the knee of the flap, where the thickness was about 10 percent less than the exit height. Downstream of the flap knee the jet thickened considerably (figs. 19(b) and 20(b)), although the stream velocity prevented the full thickening obtained with the static jet. Increasing the angle of attack to 16° thickened the jet just downstream of the exit for the low exit velocity (fig. 19(b)) in comparison with the thickness at 0° angle of attack; however, the jet thickness at the flap knee was about 20 percent less than at the exit. Downstream of the flap knee the jet thickened considerably and reached the approximate thickness shown for the static jet at the rear survey station. Results obtained for the high exit velocity (fig. 20(b)) showed about the same jet thickness ahead of the flap knee for an angle of attack of 16° as for 0°. Downstream of the flap knee the thickness with the wind on approached the thickness for the static jet.

Flap Surface Pressure Distributions

Static-pressure distributions were obtained over the upper surface of the radius flap in order to gain additional insight into the jet flow behavior relatively far downstream

of the jet exit. The pressure-distribution results for a range of thrust coefficients are presented in the form of pressure coefficients along the flap chord at the nacelle center line with the model at 0° angle of attack. Pressure coefficients for both the static data and the wind-on data were based on the dynamic pressure of the jet exit flow $\frac{1}{2}\rho U_{exit}^2$.

Static jet.- Pressure distributions over the radius flap for the static jet are presented in figure 21 for several values of jet exit velocity. Although the pressure distributions had similar shapes for all thrust levels, the pressure coefficients tended to increase somewhat with increasing exit velocity. Some of the spread in the points can be attributed to data scatter and some may be associated with small differences in uniformity of the jet flow at different exit velocities. A rough check of possible compressibility effects indicated that some of the data spread may be associated with Mach number effects on the pressure coefficients. A mean-line fairing of the data points is shown in figure 21 and is used in the comparison with the wind-on data in figure 22.

Wind-on jet at 0° angle of attack.- Static-pressure distributions obtained over the radius flap with the free-stream velocity are presented in figure 22 for the same range of jet exit velocities as for the static jet. The dashed curve of figure 22 shows the distribution obtained for the static jet. The data of figure 22 show that the flap pressure distributions over most of the flap chord were more negative with the wind on than with the static jet. This difference in pressures may be attributed to the pumping effect of the free-stream flow on the jet flow which was noted earlier in the section "Jet Total-Pressure and Velocity Profiles." Test data for the two highest exit velocities appear to define a lower limit for the wind-on pressure distributions, inasmuch as the distributions were essentially the same for both exit velocities.

An additional effect of the free-stream flow on flap pressures is shown by the adverse pressure gradient over the rear portions of the flap, which became more adverse at the low exit velocities. The two-dimensional flow separation point was estimated by the Stratford method (ref. 10) for each pressure distribution, including the static jet results, in order to assess effects of the pressure distribution on flow separation and the resulting jet deflection. The chordwise location at which separation was predicted is indicated in figure 22 by the vertical dashed lines on each pressure distribution. The locations of separation points were converted to separation angles measured from the knee of the flap to the predicted separation point on the radius flap. Separation angles Δ_j are presented in figure 23 for the range of exit velocities of the investigation. The estimated separation point with the power off is also shown in figure 23, although the pressure distribution which was based on free-stream dynamic pressure is not presented.

The results of figure 23 show that the static separation angle agreed very well with wind-on separation angles and static turning angles obtained from model force data (fig. 6), for a range of exit velocities above 140 m/sec. At low jet velocities, addition of

the free-stream flow to the jet increased the magnitude of the adverse pressure gradient over the flap, which caused the estimated flow separation points to move forward on the flap. This forward movement caused reductions in effective jet turning angles that were considerably lower than the static separation angle and the static turning from force data. The overall implication of the comparison of results in figure 23 is that, for the 90^{o} radius-flap configuration, the static turning angles obtained from force tests were applicable to the wind-on turning of the jet flow over a substantial part of the thrust range.

SUMMARY OF RESULTS

A low-speed investigation was conducted in the Langley V/STOL tunnel of the wing-surface—jet interaction characteristics of an upper-surface blown model with rectangular exhaust nozzles and a radius flap. The results of this investigation may be summarized as follows:

1. The maximum jet velocity experienced almost no decay between the nozzle exit and the knee of the radius flap. Some velocity decay was experienced in passing over the radius flap, and the details of this decay were found to vary with the aerodynamic conditions of the model.

2. The effective jet thickness showed a slight decrease between the nozzle exit and the knee of the radius flap. Over the radius flap, the effective jet thickness increased to values somewhat greater than the thickness at the nozzle exit. Variations in the effective wind-on jet thickness along the chord were found to be only slightly dependent on the angle of attack of the model.

3. Velocity profiles inside the jet were insensitive to variations in model angle of attack; however, the profiles outside the jet showed expected variations with model angle of attack.

4. The two-dimensional static separation angle, estimated from pressure distributions over the upper surface of the radius flap for the static jet, agreed well with the three-dimensional static turning angle obtained from model force tests at moderate to high thrust levels.

5. Addition of the free-stream flow to the jet increased the magnitude of the adverse pressure gradient over the radius flap, and the estimated flow separation points at low exit velocities moved forward on the flap. The forward movement caused significant reductions in effective jet-turning angles that were considerably lower than the three-dimensional static turning.

6. At the highest jet velocities, the estimated separation points moved rearward and the accompanying effective wind-on turning angles were in excellent agreement with the static turning angles obtained from model force data.

Langley Research Center
National Aeronautics and Space Administration
Hampton, VA 23665
October 7, 1976

APPENDIX

COMPUTATION OF VELOCITY FROM TOTAL-PRESSURE MEASUREMENTS

The velocity profiles shown in the basic data (figs. 8 to 11) were computed by the method discussed in reference 11. Velocities were computed from the following relationship:

$$U = K\sqrt{1 - \left(\frac{p}{p_t}\right)^{0.2857}}$$

where K is a constant used to relate the pressure measurements to jet velocity. Values of K for the present computation were 761 for U in m/sec, and 2496 for U in ft/sec.

REFERENCES

1. Smith, Charles C., Jr.; Phelps, Arthur E., III; and Copeland, W. Latham: Wind-Tunnel Investigation of a Large-Scale Semispan Model With an Unswept Wing and an Upper-Surface Blown Jet Flap. NASA TN D-7526, 1974.

2. Phelps, Arthur E., III; and Smith, Charles C., Jr.: Wind-Tunnel Investigation of an Upper Surface Blown Jet-Flap Powered-Lift Configuration. NASA TN D-7399, 1973.

3. Phelps, Arthur E.; Letko, William; and Henderson, Robert L.: Low-Speed Wind-Tunnel Investigation of a Semispan STOL Jet Transport Wing-Body With an Upper-Surface Blown Jet Flap. NASA TN D-7183, 1973.

4. Sleeman, William C., Jr.; and Hohlweg, William C.: Low-Speed Wind-Tunnel Investigation of a Four-Engine Upper Surface Blown Model Having a Swept Wing and Rectangular and D-Shaped Exhaust Nozzles. NASA TN D-8061, 1975.

5. Clark, Lorenzo R.: An Experimental Study of the Noise Field Generated by Jet Flow Blowing Over the Upper Surface of a Simulated Wing and Flap. M.S. Thesis, George Washington Univ., 1974.

6. Johnson, William G., Jr.: Aerodynamic Characteristics of a Powered Externally Blown Flap STOL Transport Model With Two Engine Simulator Sizes. NASA TN D-8057, 1975.

7. Hoad, Danny R.: Longitudinal Aerodynamic Characteristics of a Deflected-Thrust Propulsive-Lift Transport Model. NASA TM X-3234, 1975.

8. Heyson, Harry H.: Linearized Theory of Wind-Tunnel Jet-Boundary Corrections and Ground Effect for VTOL-STOL Aircraft. NASA TR R-124, 1962.

9. Glauert, M. B.: The Wall Jet. J. Fluid Mech., vol. 1, pt. 6, Dec. 1956, pp. 625-643.

10. Stratford, B. S.: The Prediction of Separation of the Turbulent Boundary Layer. J. Fluid Mech., vol. 5, pt. 1, Jan. 1959, pp. 1-16.

11. Bailey, Frederick J., Jr.; Zolovcik, John A.; Phillips, William H.; and Huston, Wilber B.: Piloted Aircraft Testing. High Speed Problems of Aircraft and Experimental Methods, A. F. Donovan, H. R. Lawrence, F. E. Goddard, and R. R. Gilruth, eds., Princeton Univ. Press, 1961, pp. 833-904.

TABLE I.- TOTAL-PRESSURE PROFILES

Survey station	α, deg	q		x		Basic-data figure
		Pa	lb/ft^2	cm	in.	
1	0	0	0	0	0	8(a)
2	↓	↓	↓	2.95	1.16	8(b)
3				4.06	1.60	8(c)
4				5.44	2.14	8(d)
5				6.63	2.61	8(e)
6				14.83	5.84	8(f)
7				16.31	6.42	8(g)
8				17.83	7.02	8(h)
9				20.68	8.14	8(i)
10				21.89	8.62	8(j)
1	0	766	16	0	0	9(a)
2	↓	↓	↓	2.95	1.16	9(b)
3				4.06	1.60	9(c)
4				5.44	2.14	9(d)
5				6.63	2.61	9(e)
6				14.83	5.84	9(f)
7				16.31	6.42	9(g)
8				17.83	7.02	9(h)
9				20.68	8.14	9(i)
10				21.89	8.62	9(j)
1	8	766	16	0	0	10(a)
2	↓	↓	↓	2.95	1.16	10(b)
3				4.06	1.60	10(c)
4				5.44	2.14	10(d)
5				6.63	2.61	10(e)
6				14.83	5.84	10(f)
7				16.31	6.42	10(g)
8				17.83	7.02	10(h)
9				20.68	8.14	10(i)
10				21.89	8.62	10(j)
1	16	766	16	0	0	11(a)
2	↓	↓	↓	2.95	1.16	11(b)
3				4.06	1.60	11(c)
4				5.44	2.14	11(d)
5				6.63	2.61	11(e)
6				14.83	5.84	11(f)
7				16.31	6.42	11(g)
8				17.83	7.02	11(h)
9				20.68	8.14	11(i)
10				21.89	8.62	11(j)

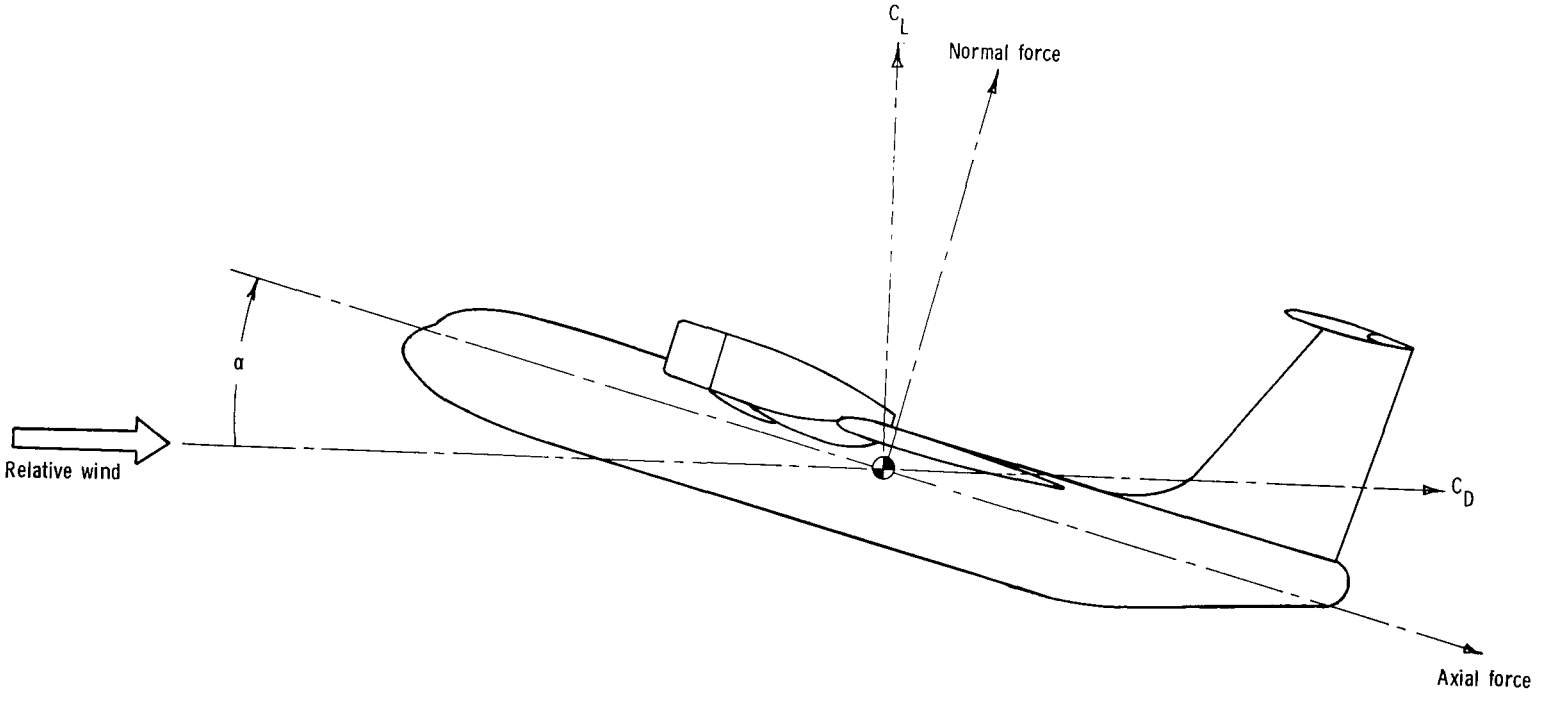

Figure 1.- System of axes used in presentation of model force data.

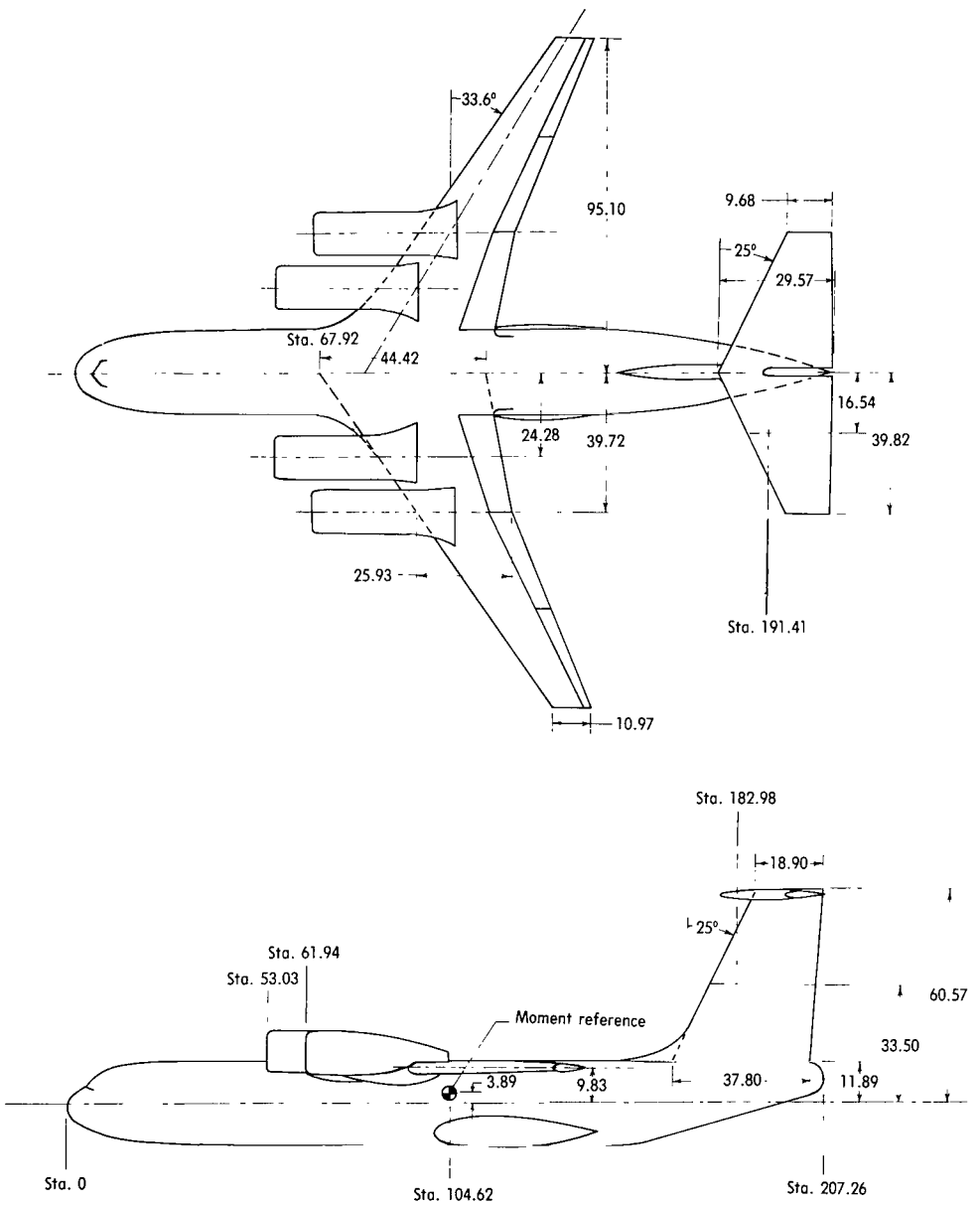

(a) General arrangement and principal dimensions of model with rectangular exhaust nozzles.

Figure 2.- Upper-surface blown model tested in Langley V/STOL tunnel. All dimensions are in centimeters.

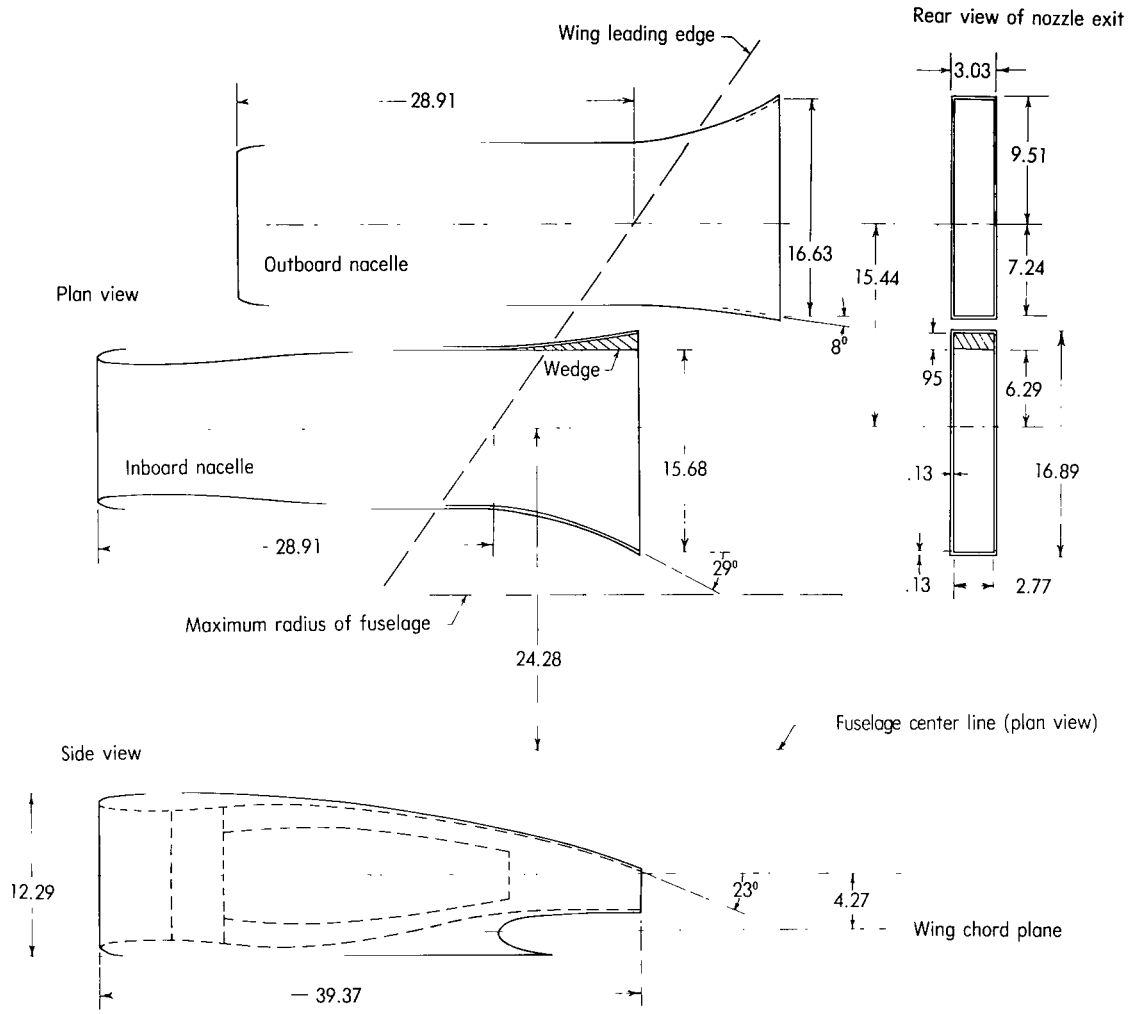

(b) Details of nacelles and rectangular exhaust nozzles.

Figure 2.- Continued.

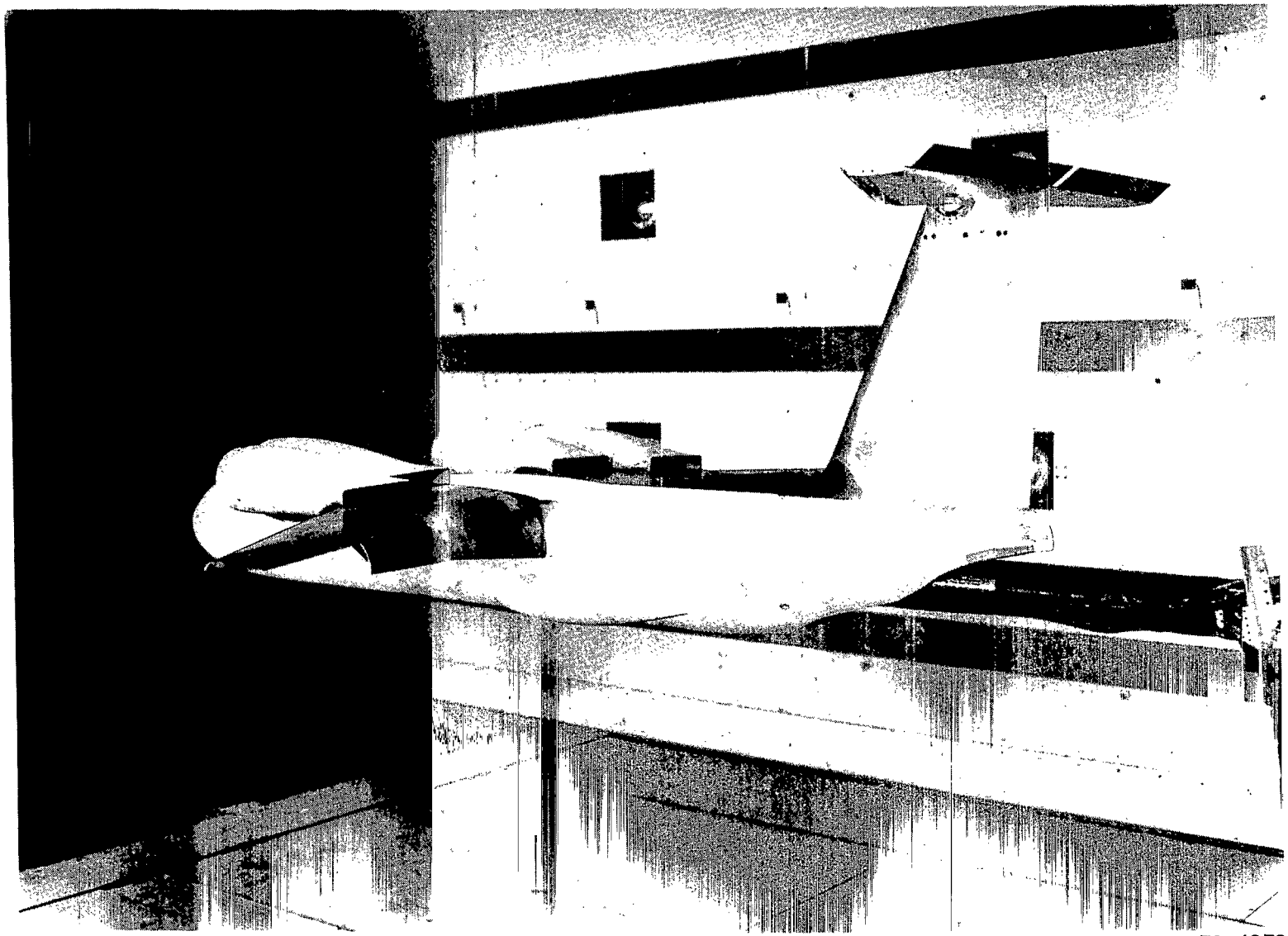

L-73-4273

(c) Photograph of model in Langley V/STOL tunnel.

Figure 2.- Concluded.

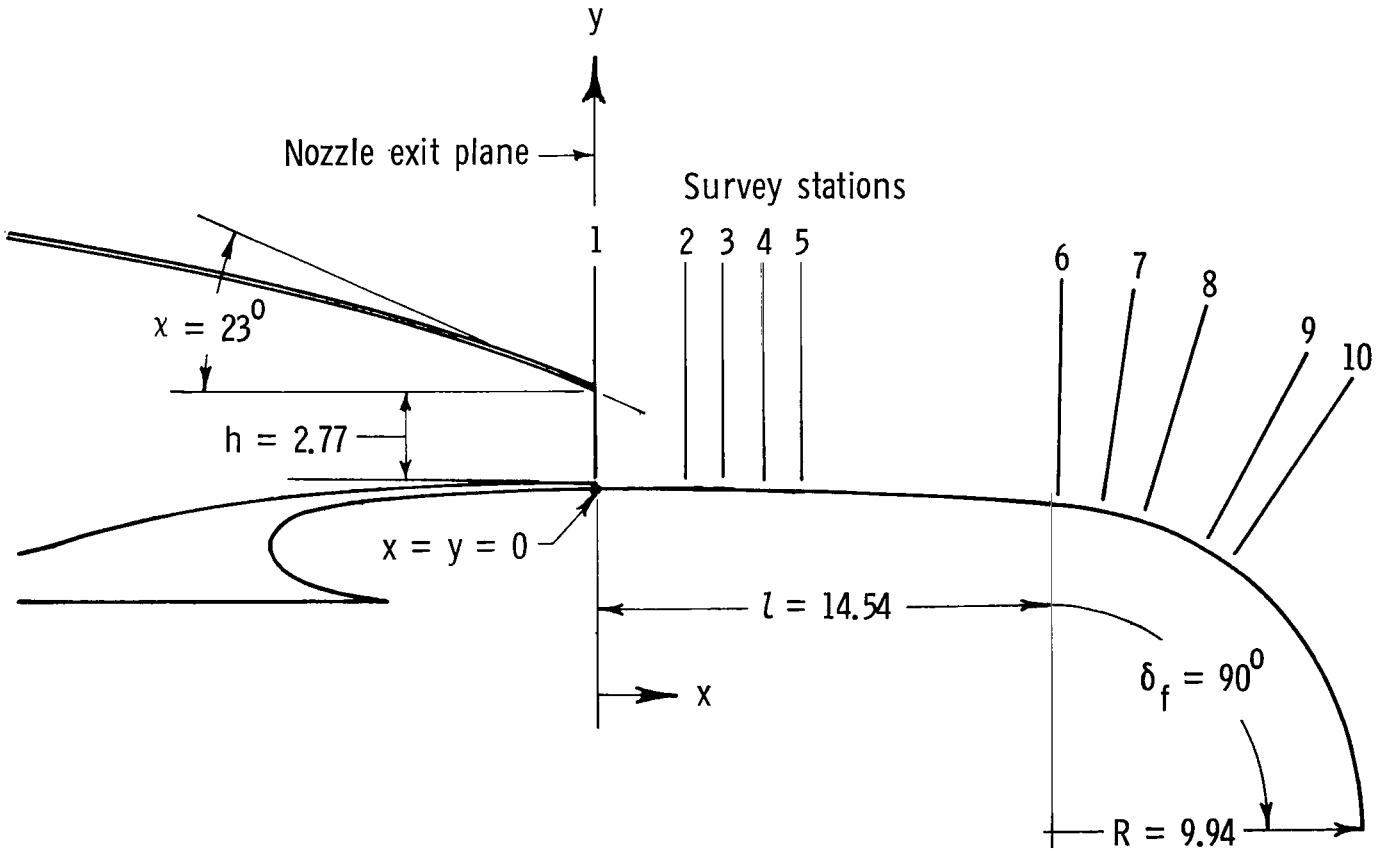

(a) Survey rake positions shown in relation to nozzle exit and radius flap.
All dimensions are in centimeters.

Figure 3.- Survey-rake stations along center line of inboard nacelle and radius-flap high-lift system.

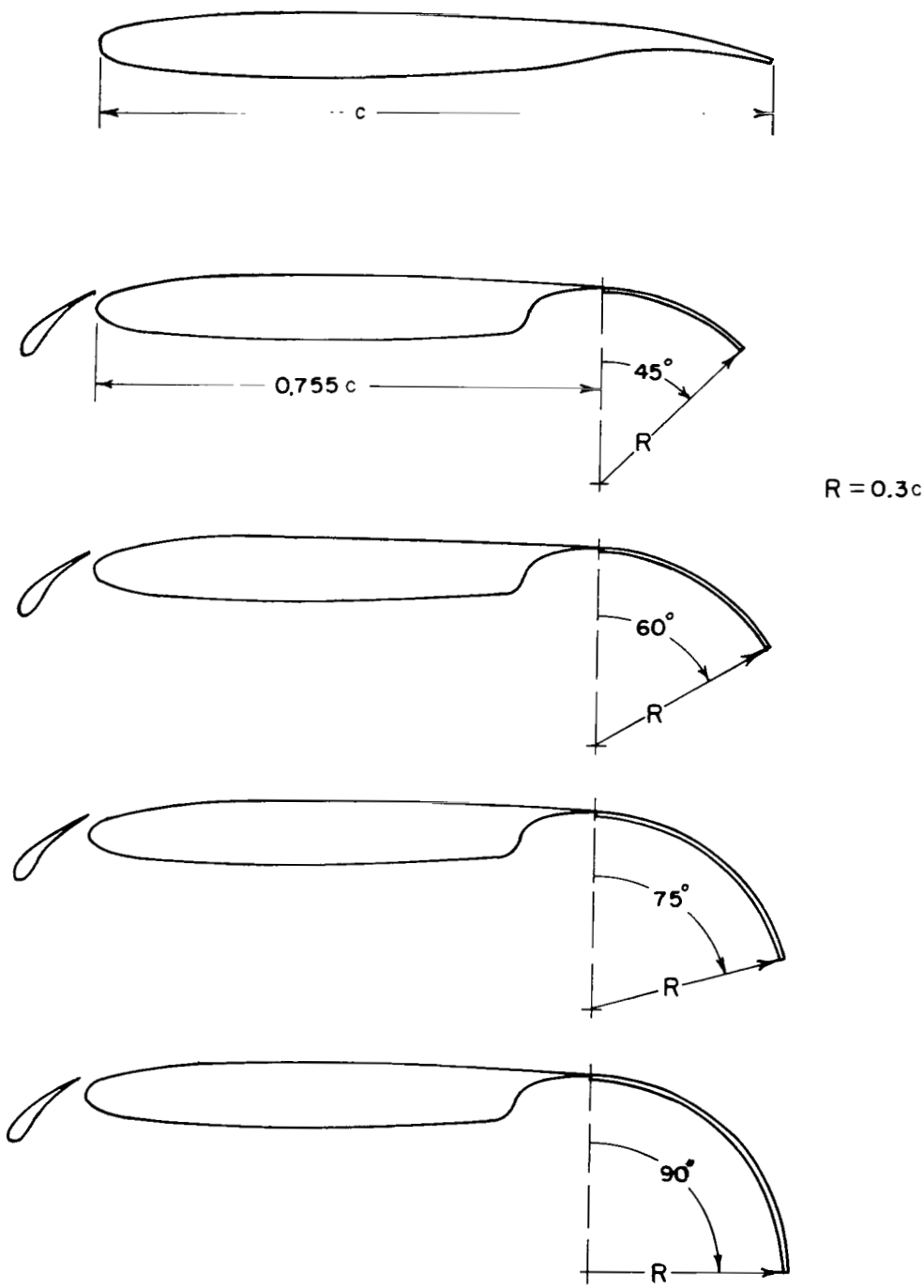

(b) Radius-flap high-lift system.

Figure 3.- Concluded.

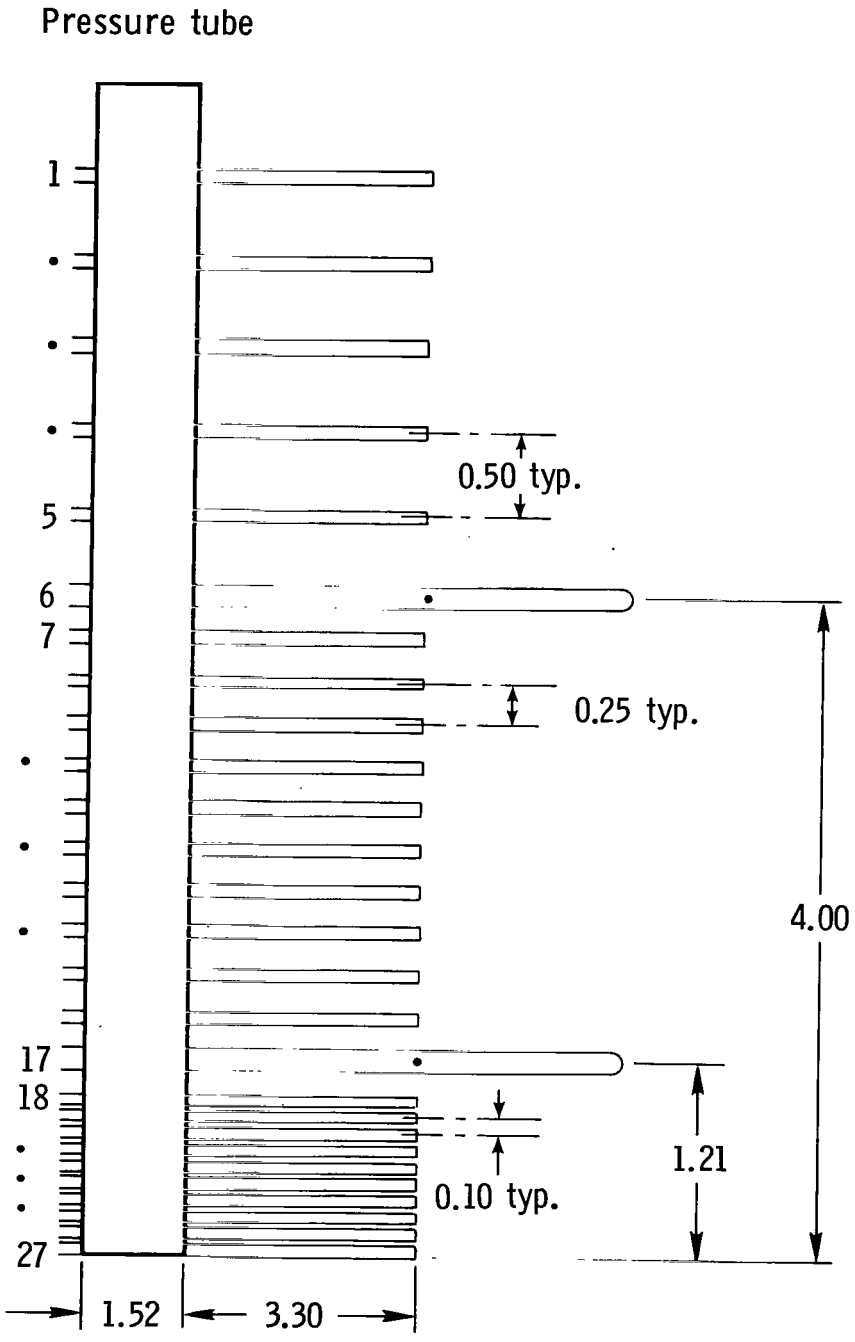

Figure 4.- Survey rake used in measurement of velocity profiles. All dimensions are in centimeters.

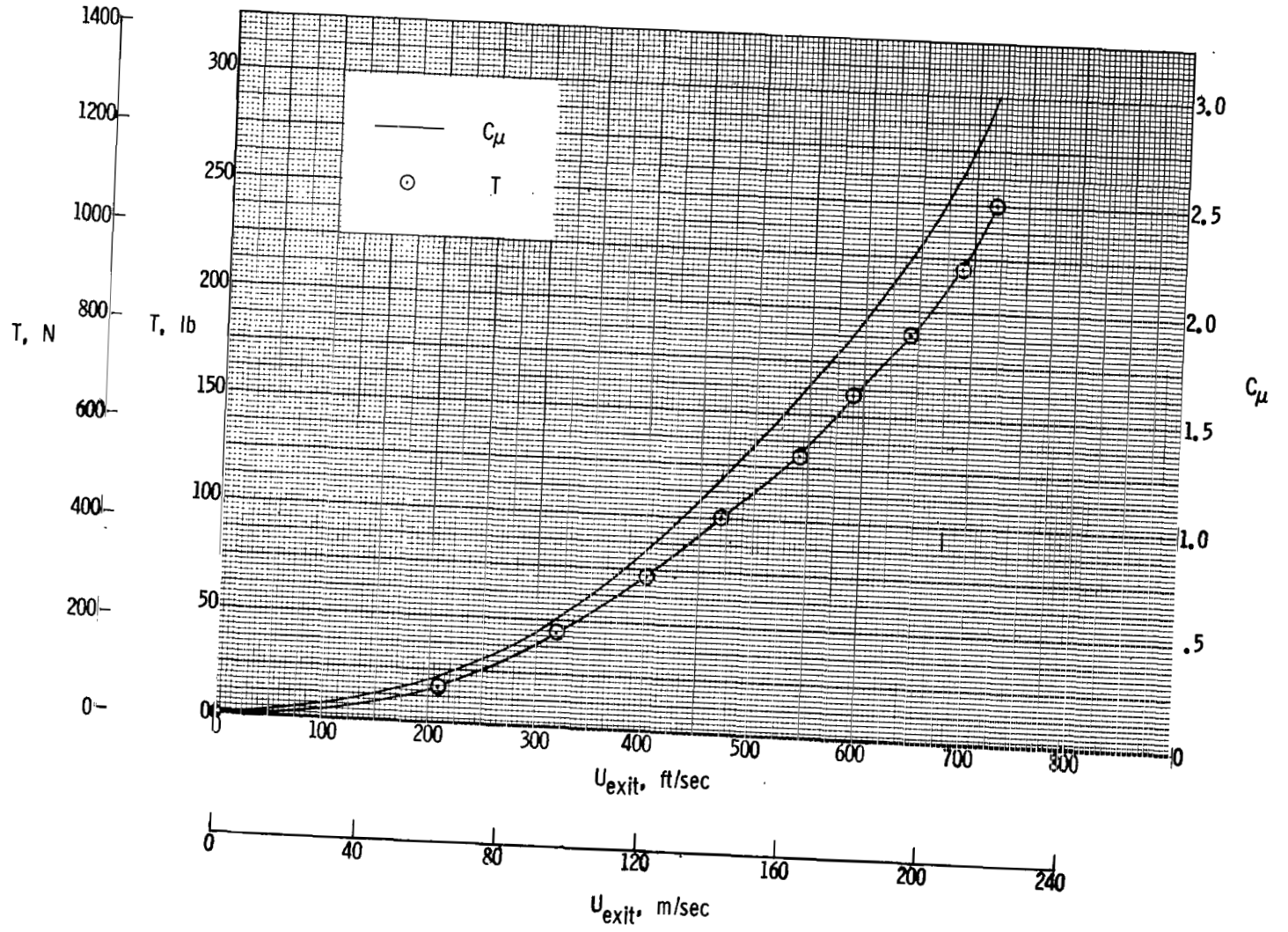

Figure 5.- Relationship between jet exit velocity, thrust, and thrust coefficient for q = 766 Pa (16 lb/ft^2).

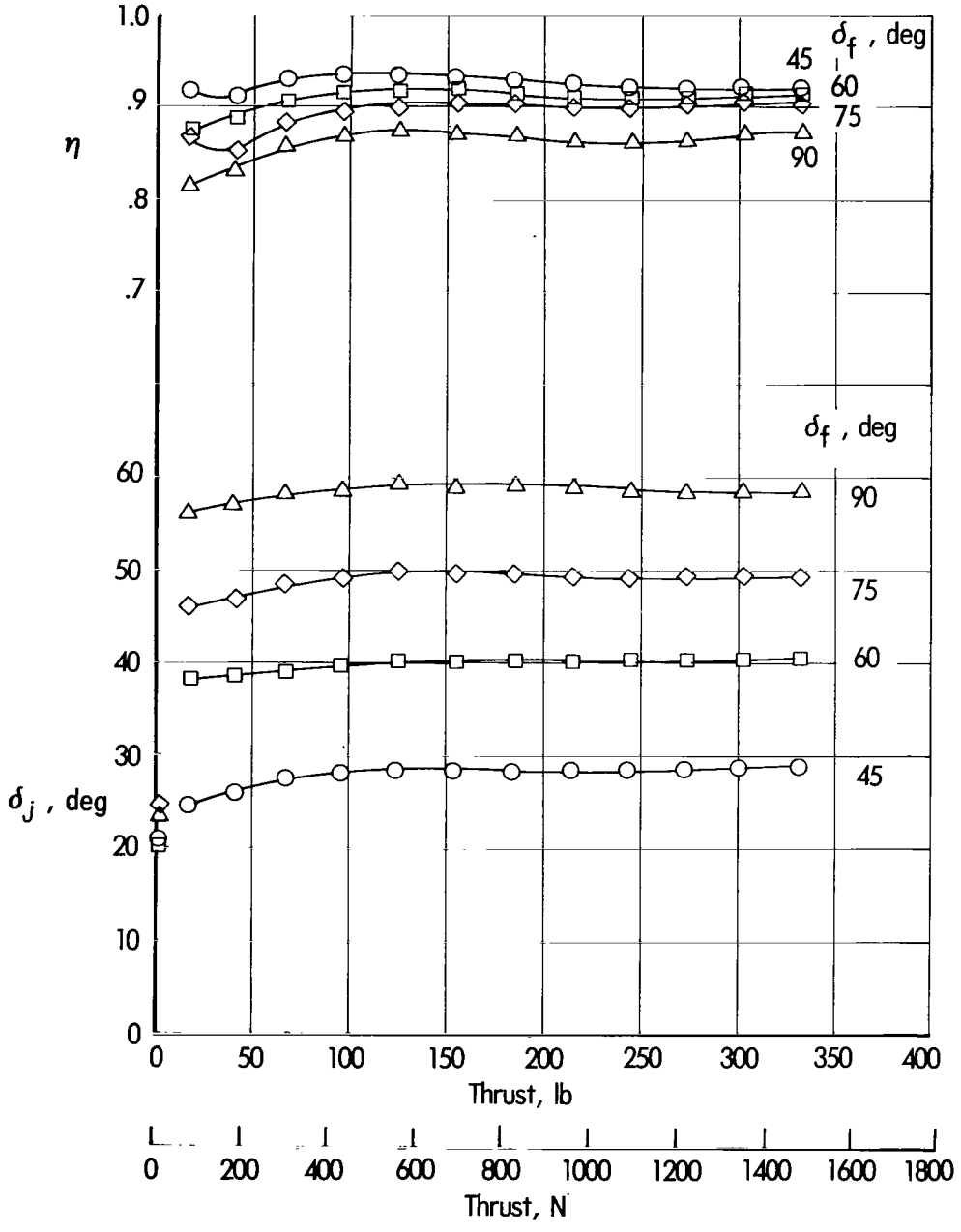

Figure 6.- Effect of radius-flap deflection on variation of static turning angle and static thrust-recovery efficiency with static thrust as determined from force tests of reference 4. $\alpha = 0^{o}$.

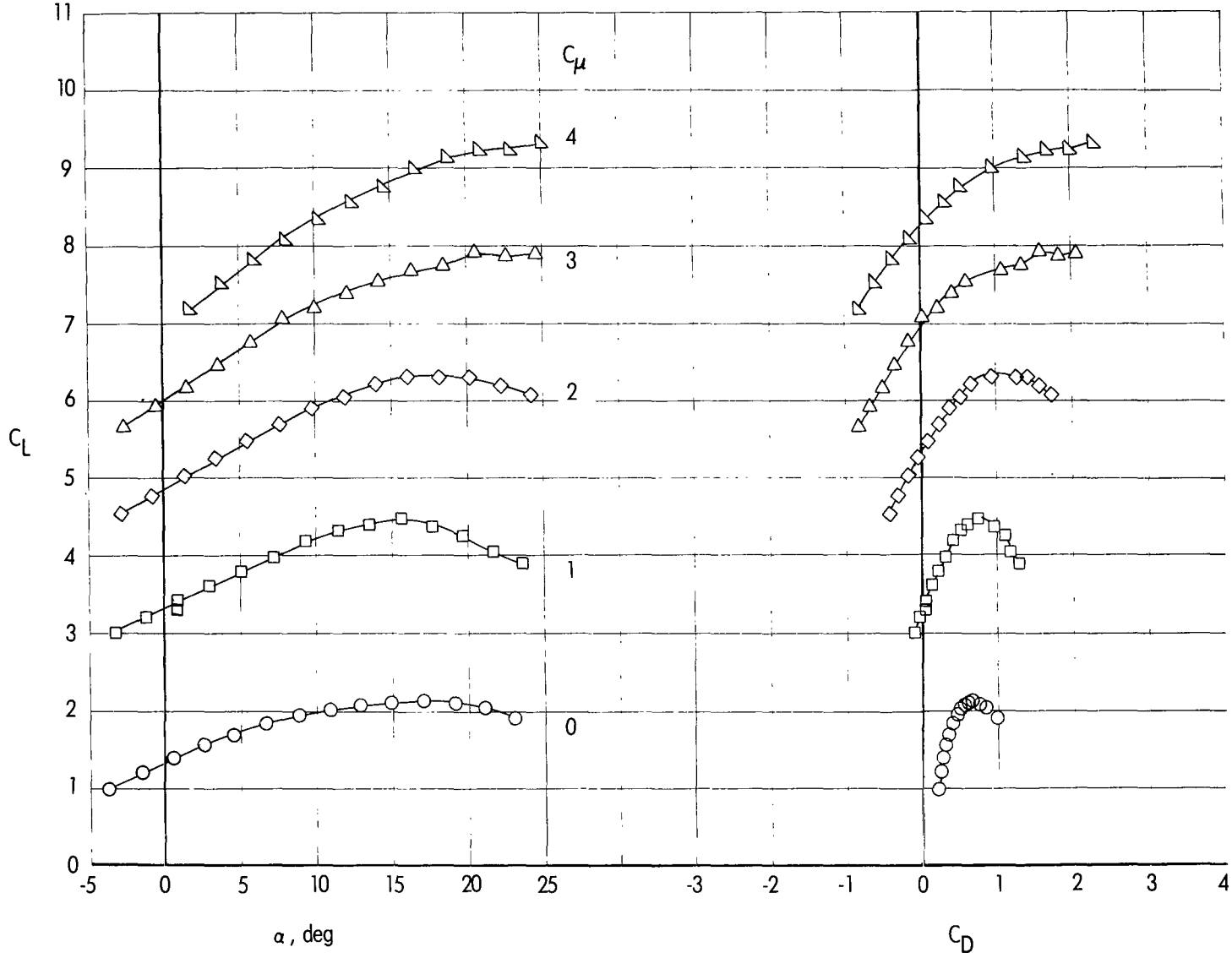

Figure 7.- Variation of lift and drag coefficients, as determined from aerodynamic tests of reference 4, with angle of attack for model with 90^o radius flap.

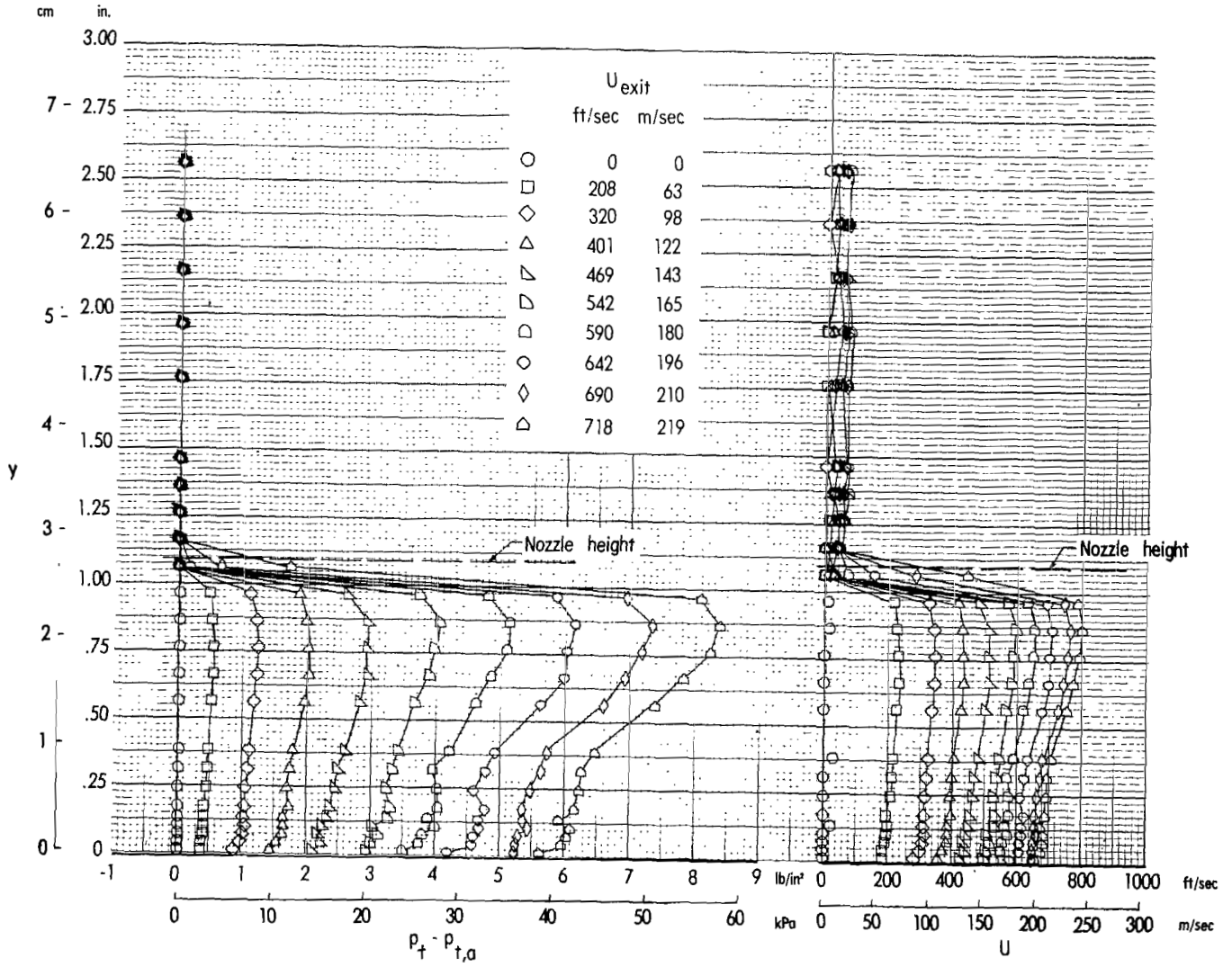

(a) x = 0 cm (nozzle exit).

Figure 8.- Static jet velocity and total-pressure profiles obtained at various chordwise stations along the nacelle center line behind the nozzle exit.

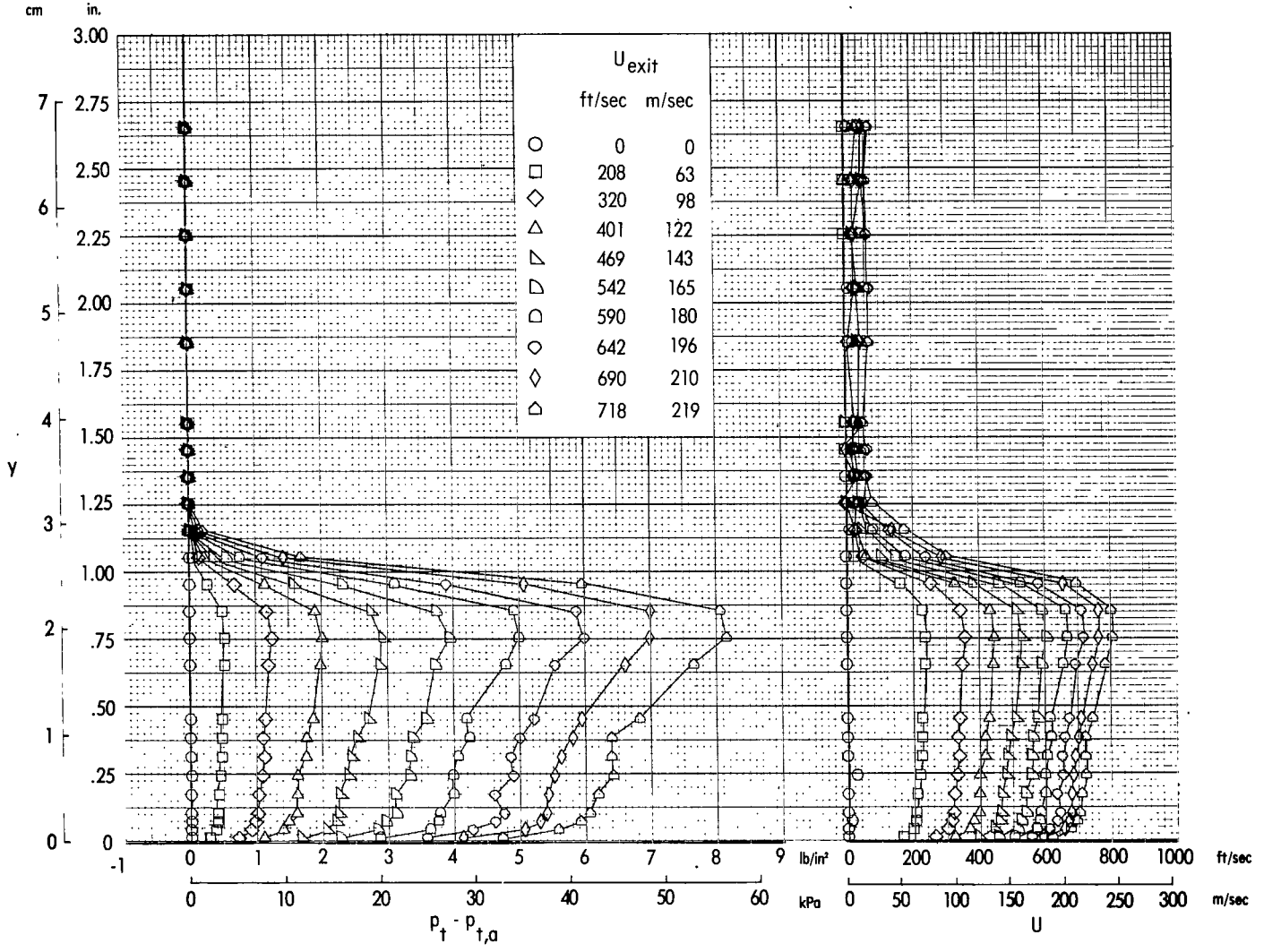

(b) x = 2.95 cm.

Figure 8. - Continued.

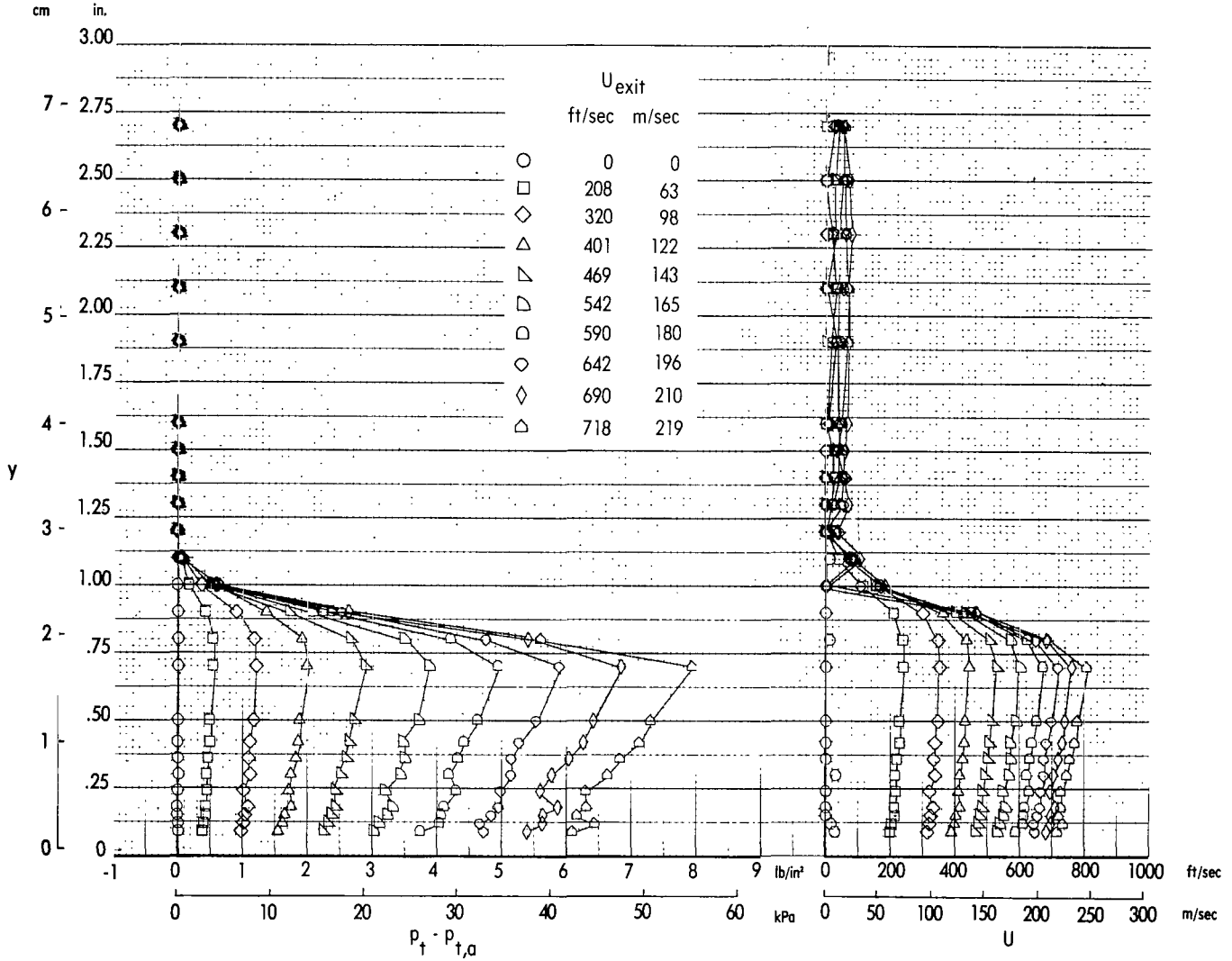

(c) x = 4.06 cm.

Figure 8.- Continued.

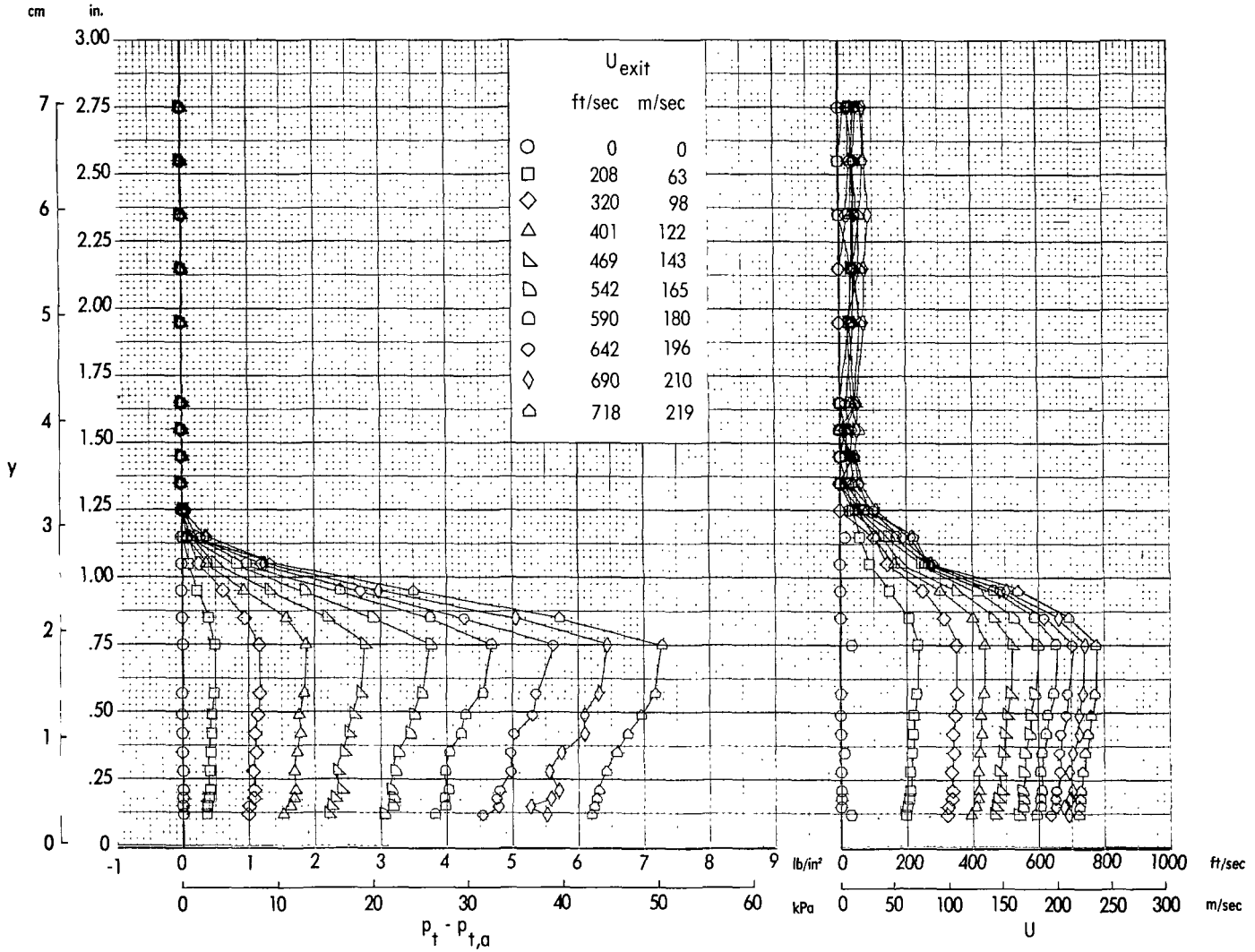

(d) x = 5.44 cm.

Figure 8.- Continued.

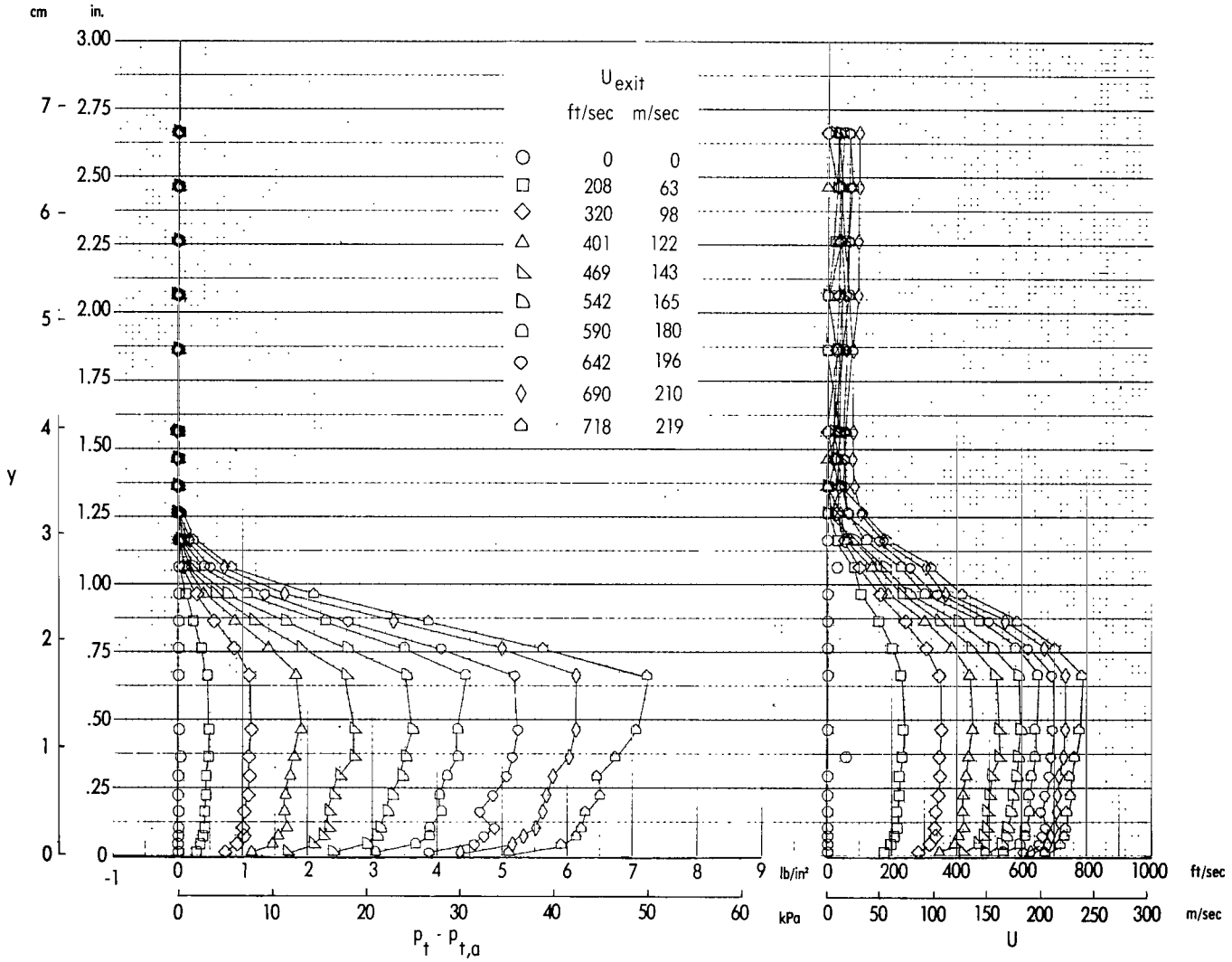

(e) x = 6.63 cm.

Figure 8.- Continued.

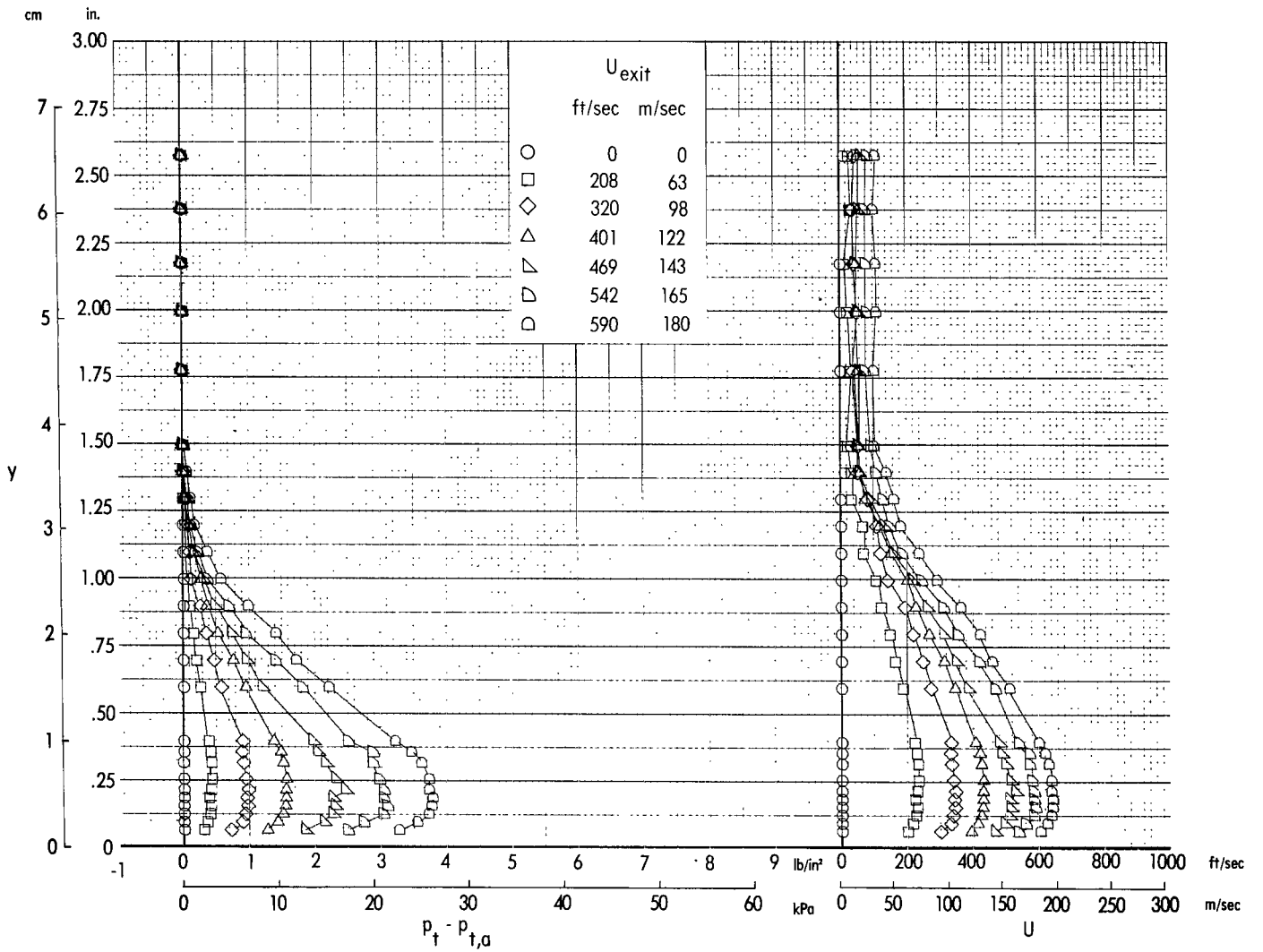

(f) x = 14.83 cm (flap knee).

Figure 8.- Continued.

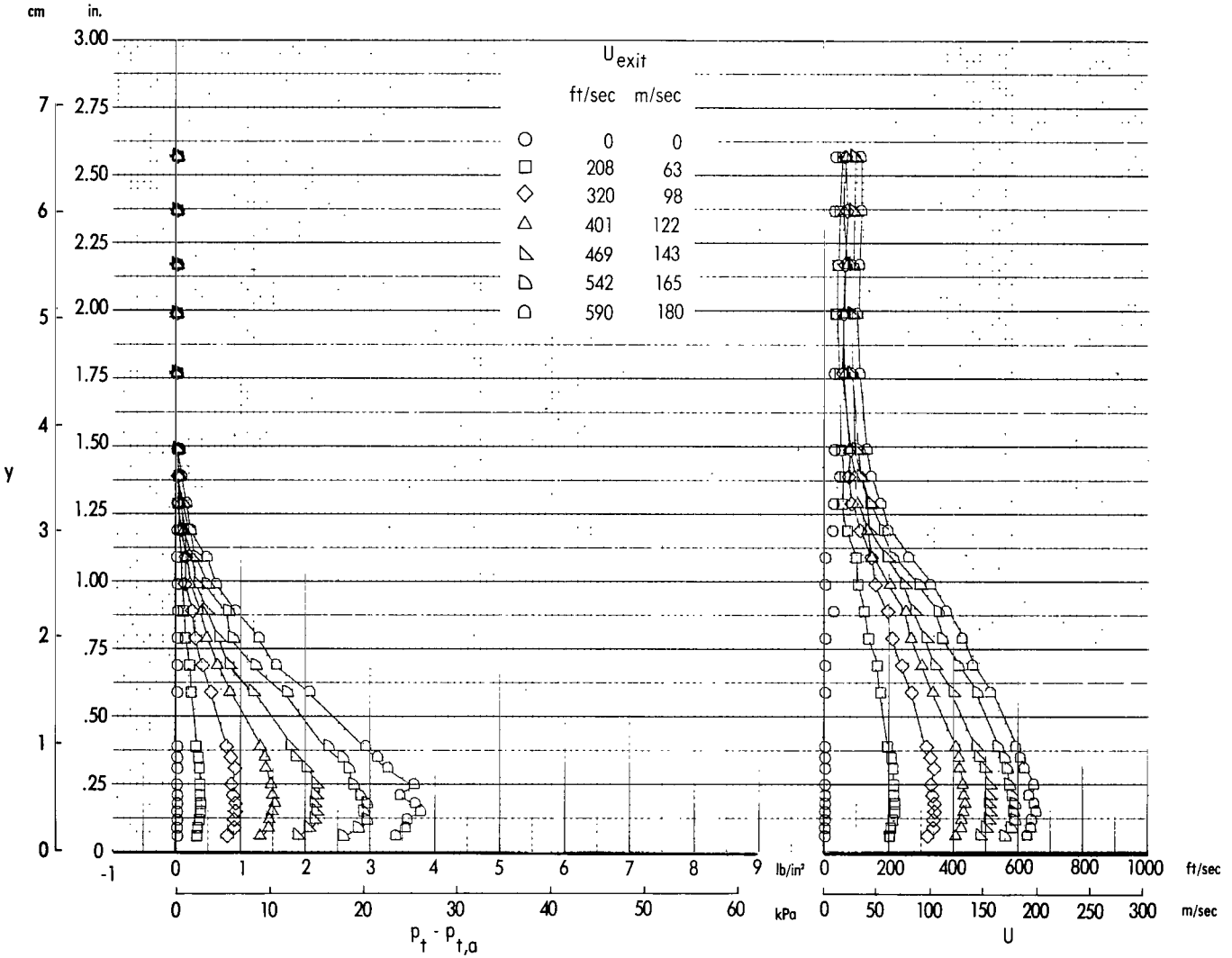

(g) x = 16.31 cm.

Figure 8.- Continued.

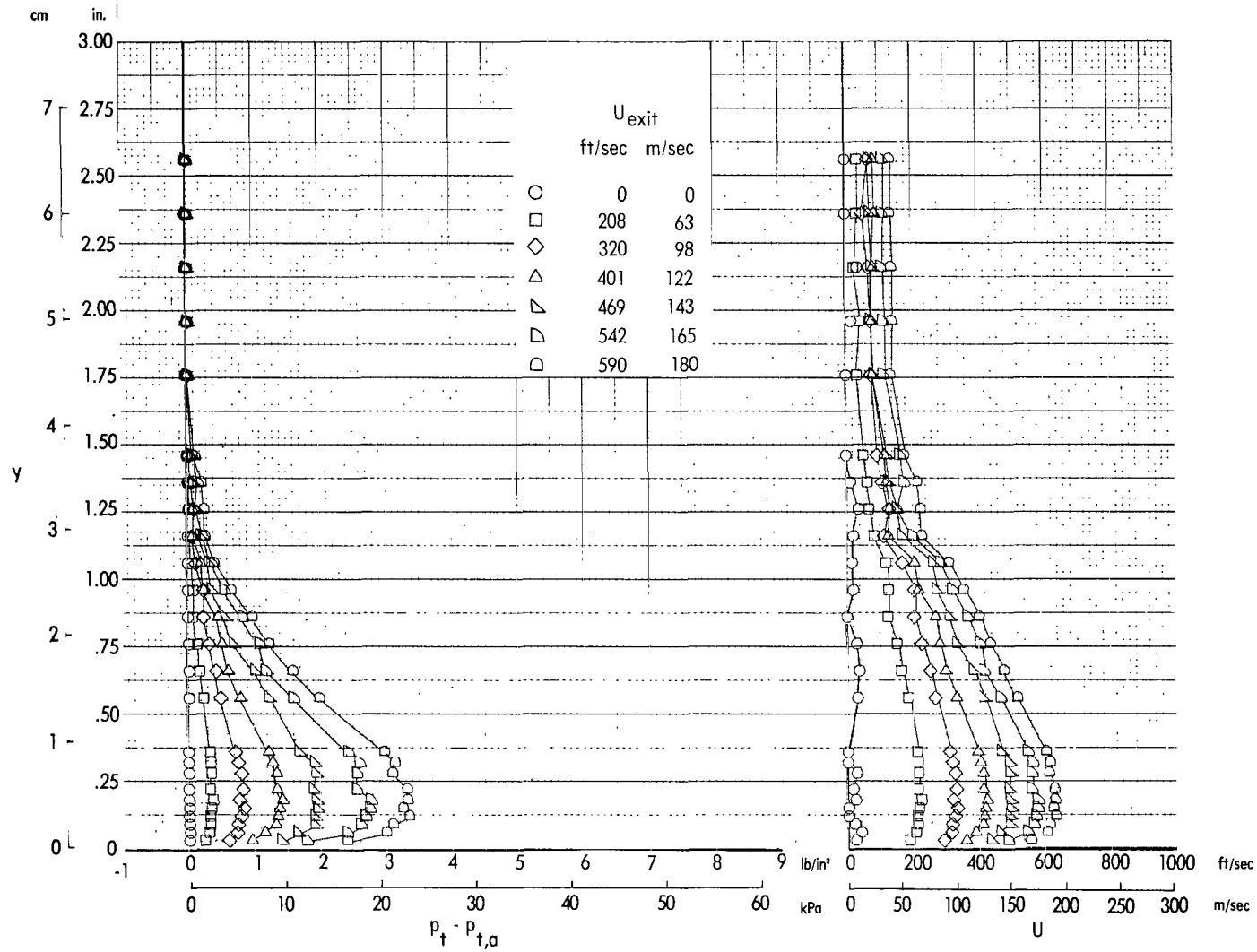

(h) x = 17.83 cm.

Figure 8.- Continued.

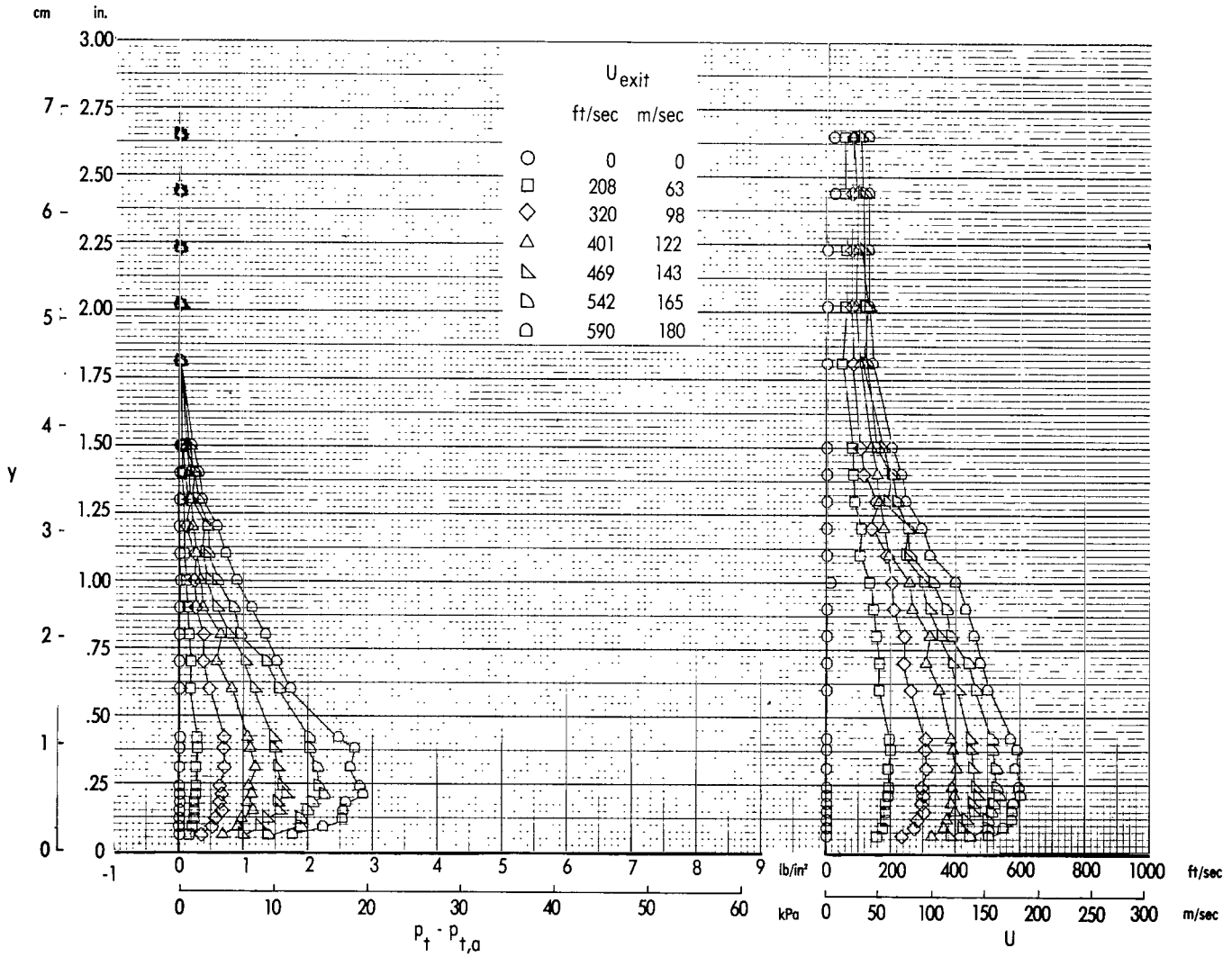

(i) x = 20.68 cm.

Figure 8.- Continued.

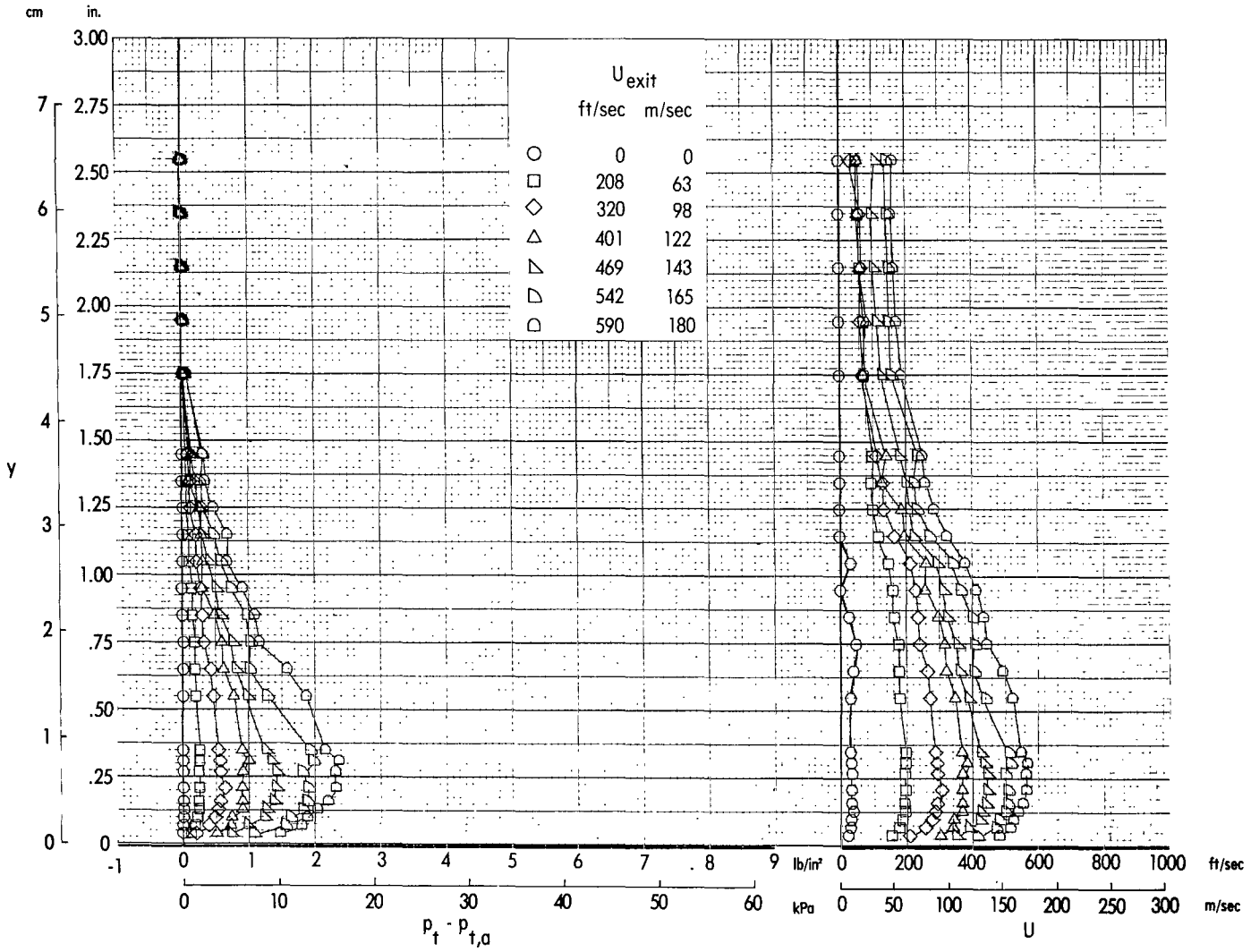

(j) x = 21.89 cm.

Figure 8.- Concluded.

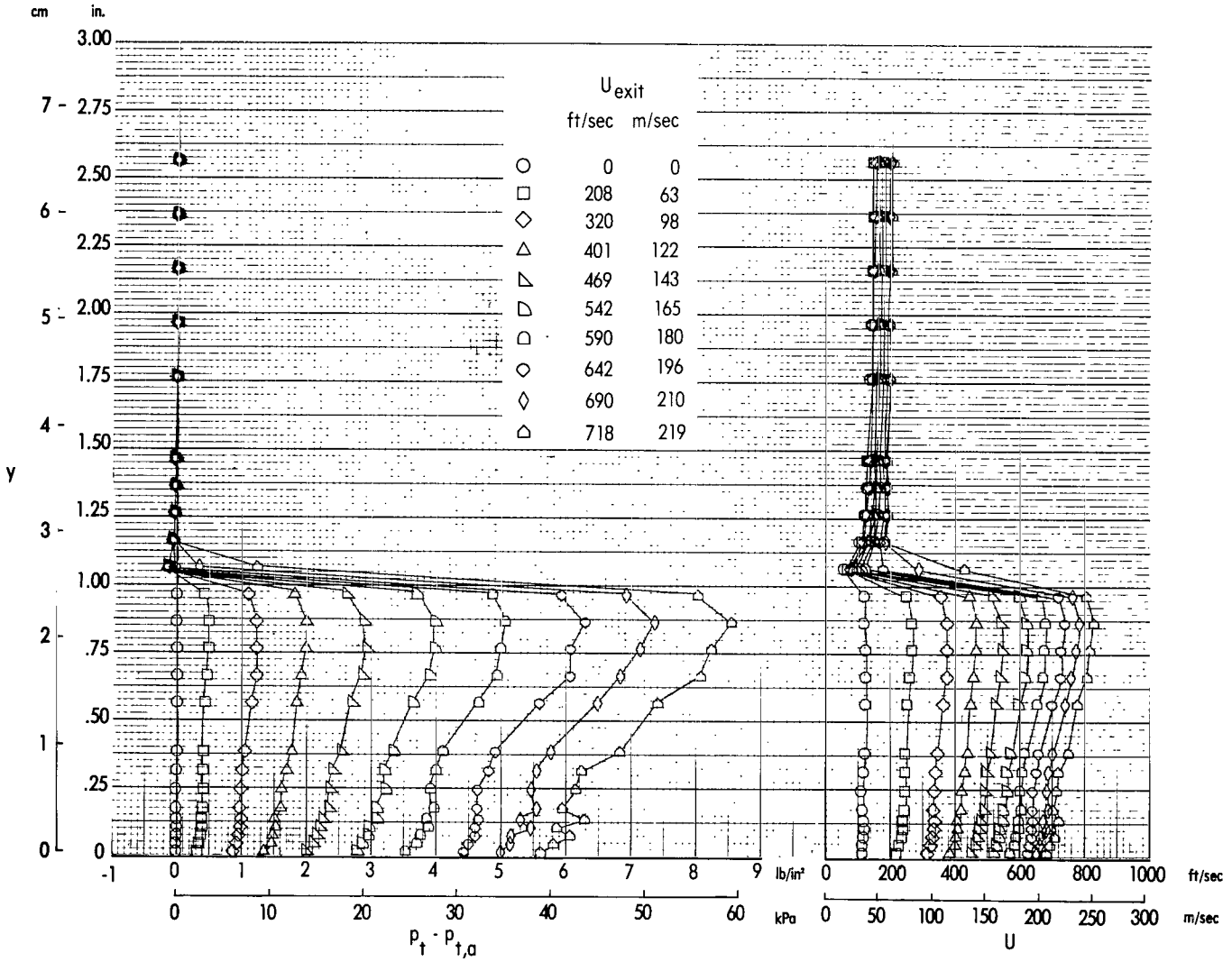

(a) x = 0 cm (nozzle exit).

Figure 9.- Jet velocity and total-pressure profiles with free-stream flow, obtained at various chordwise stations along the nacelle center line behind the nozzle exit. q = 766 Pa; $\alpha = 0^{o}$.

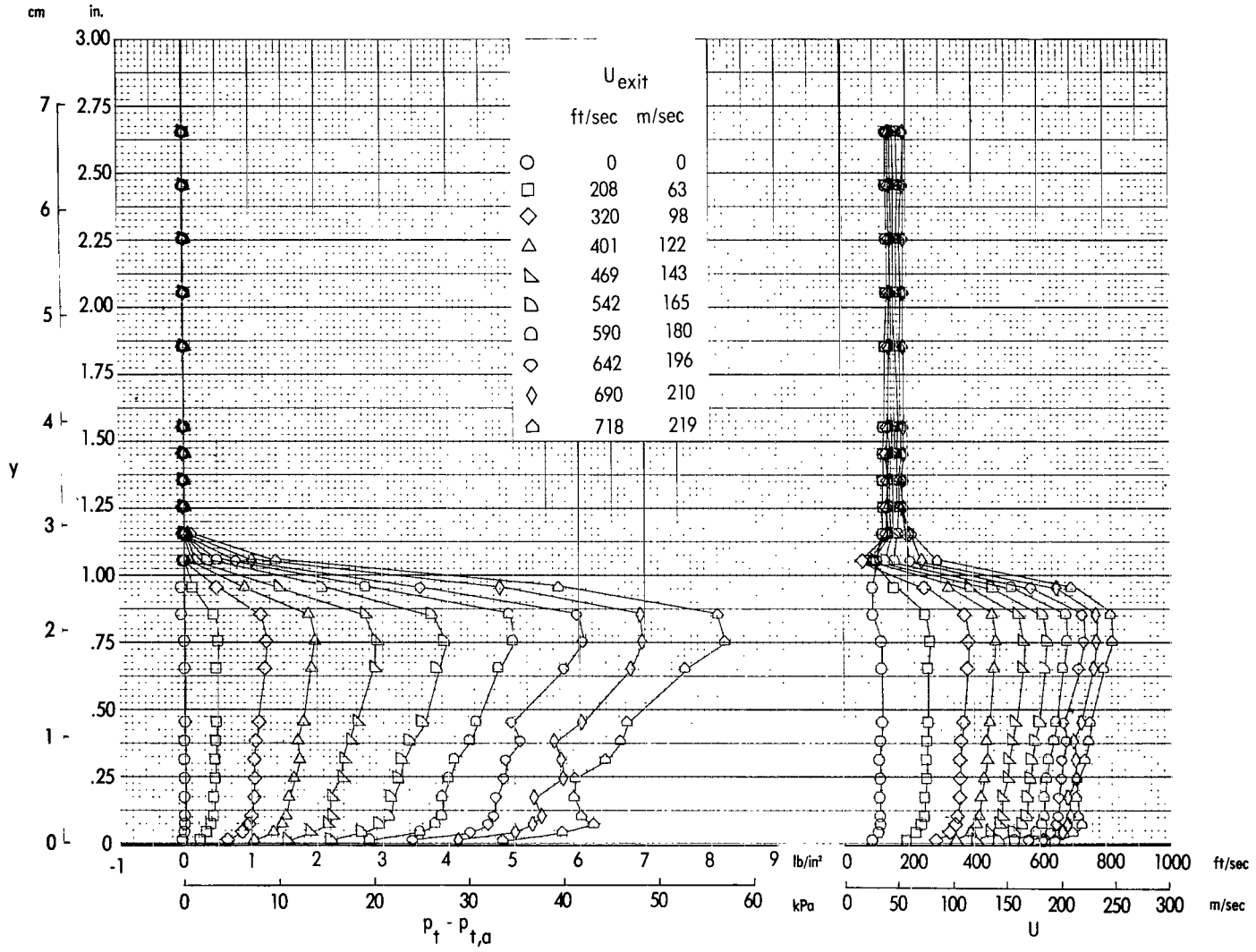

(b) x = 2.95 cm.

Figure 9.- Continued.

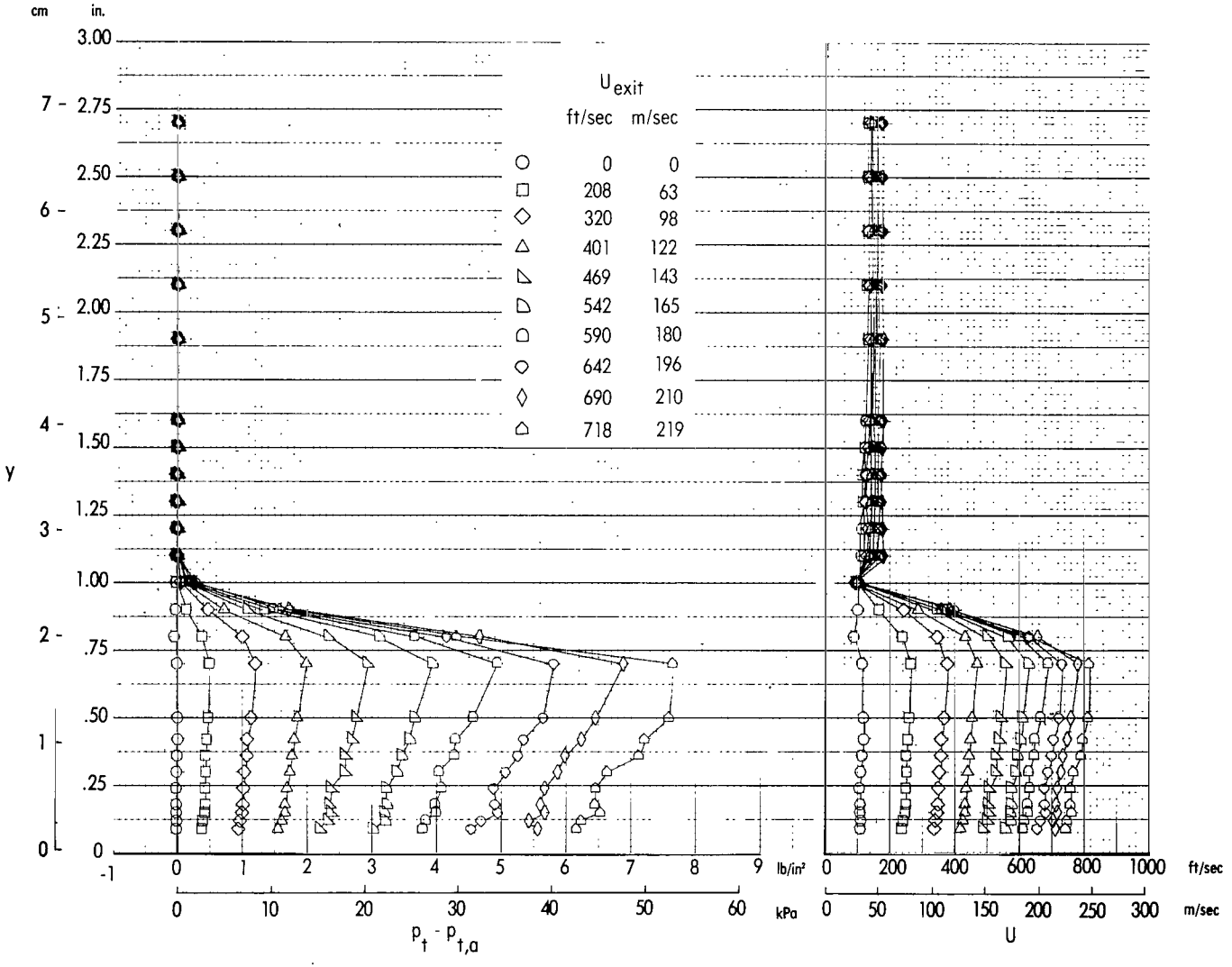

(c) x = 4.06 cm.

Figure 9.- Continued.

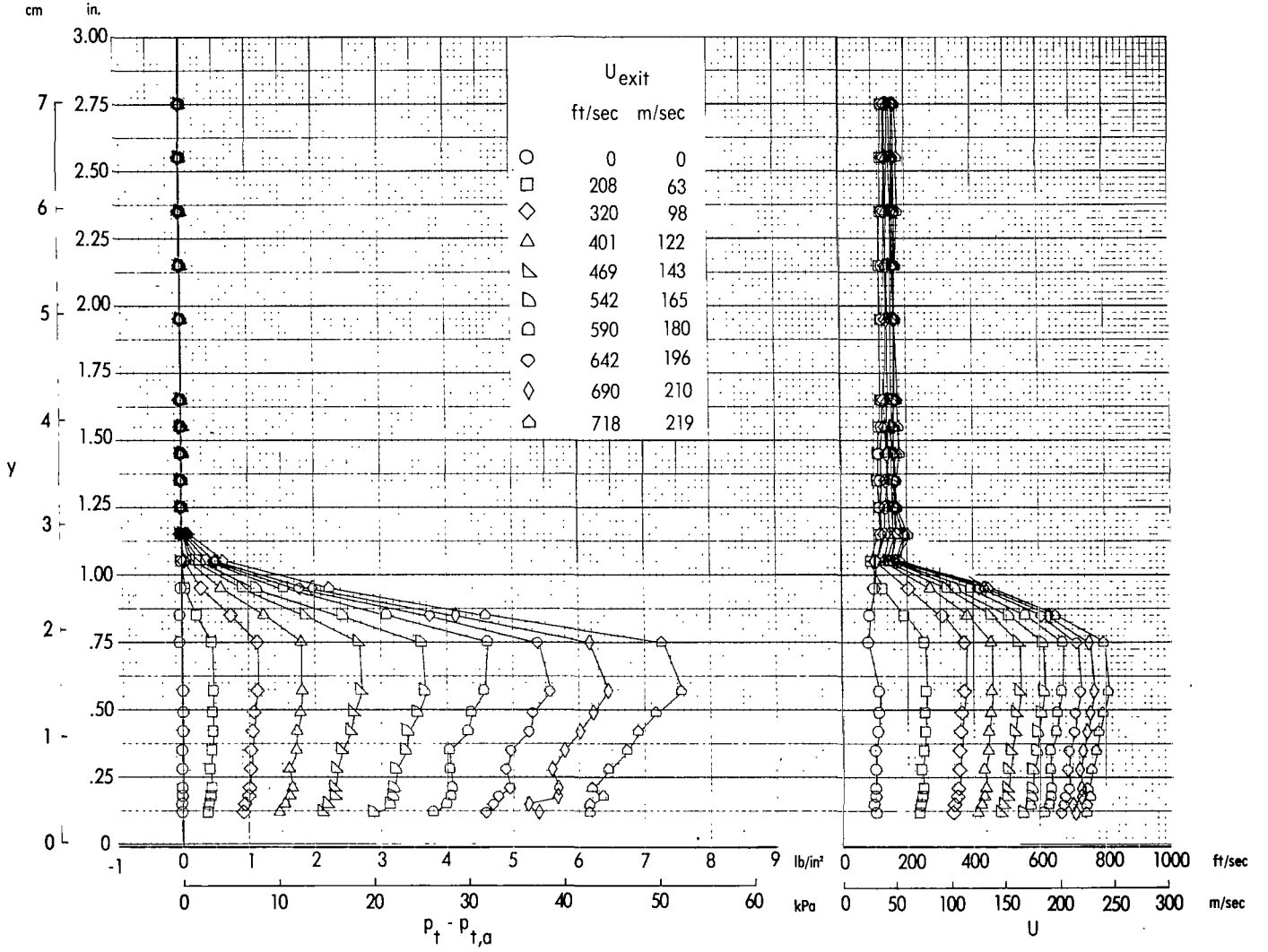

(d) x = 5.44 cm.

Figure 9.- Continued.

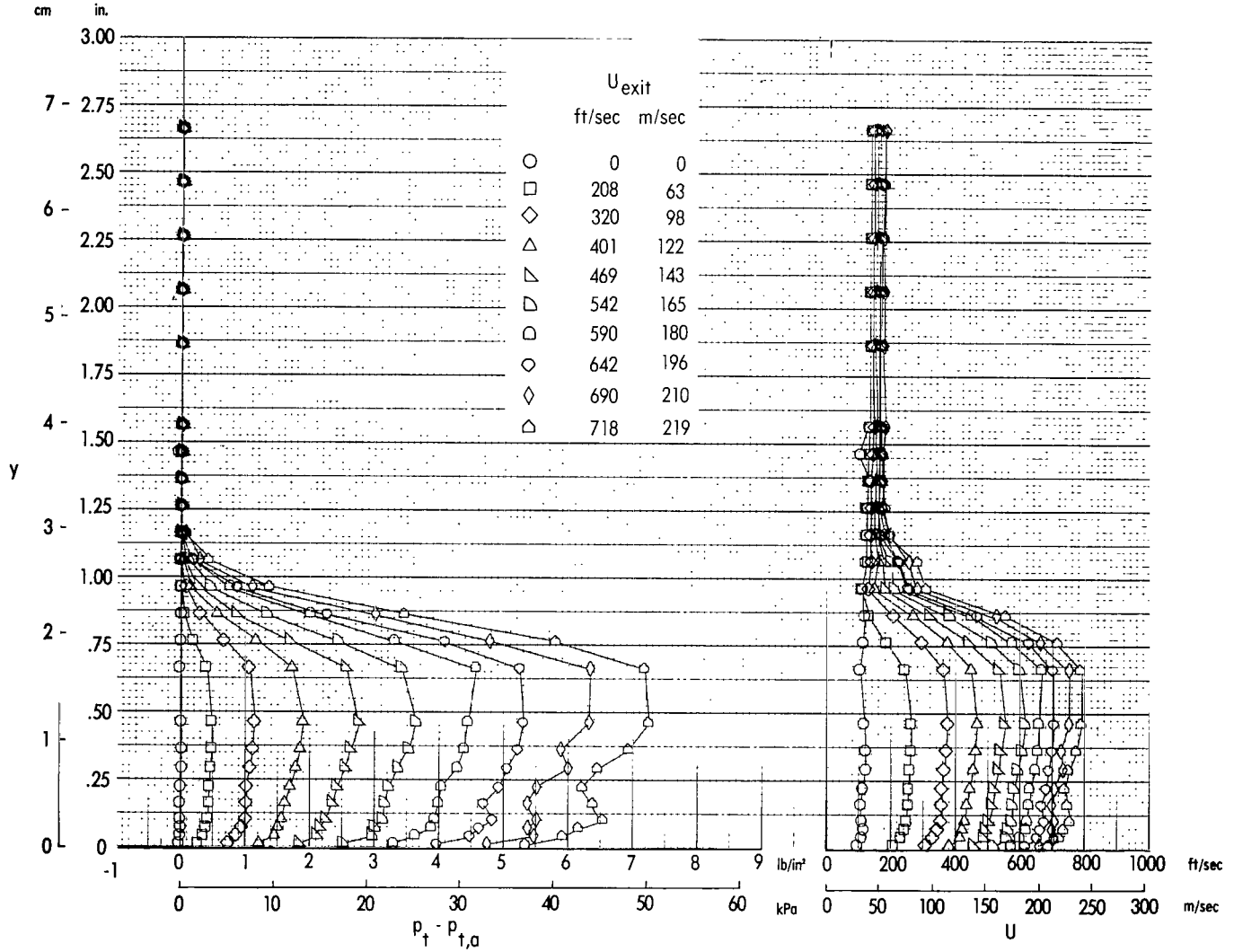

(e) x = 6.63 cm.

Figure 9.- Continued.

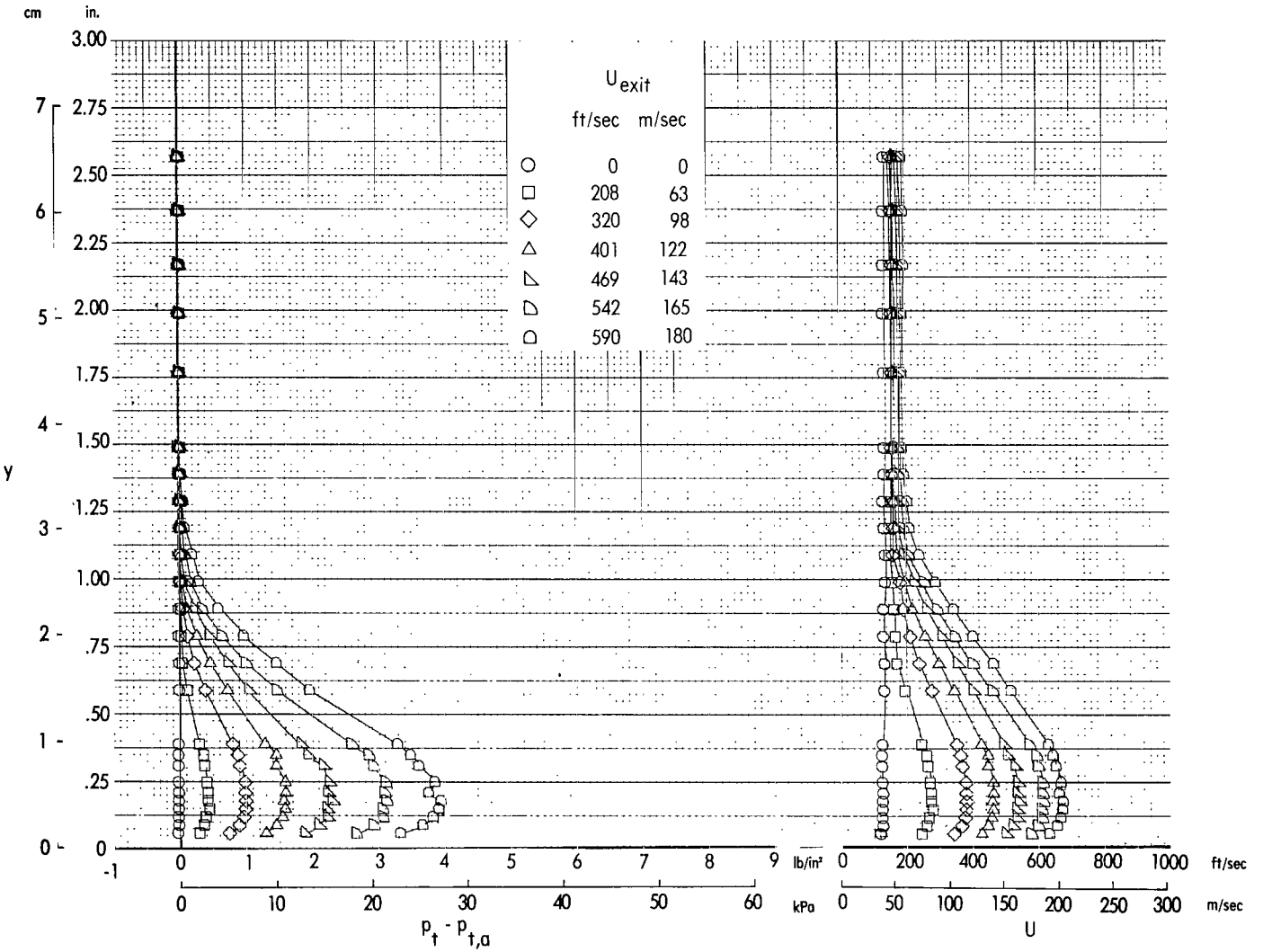

(f) x = 14.83 cm (flap knee).

Figure 9.- Continued.

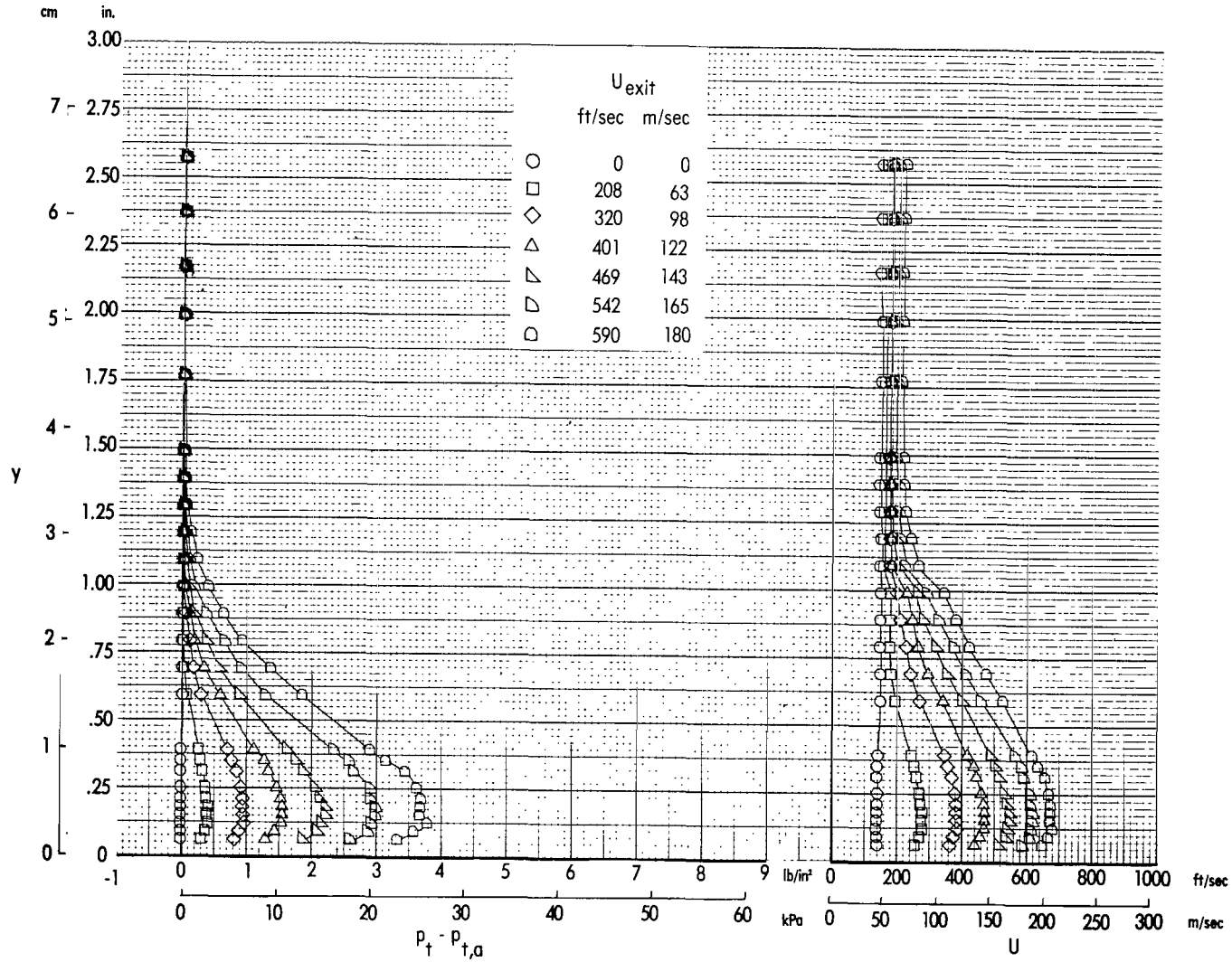

(g) x = 16.31 cm.

Figure 9.- Continued.

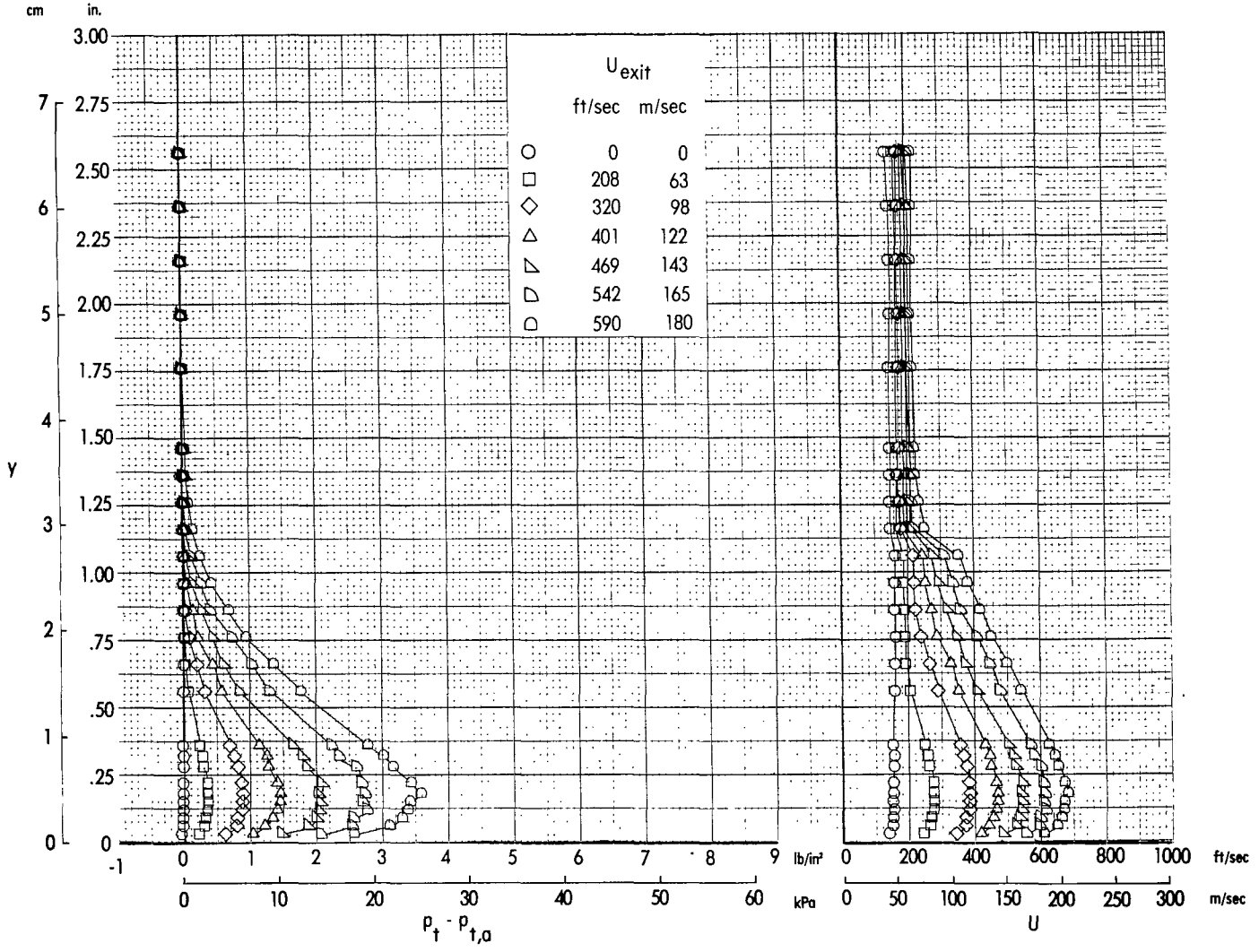

(h) x = 17.83 cm.

Figure 9.- Continued.

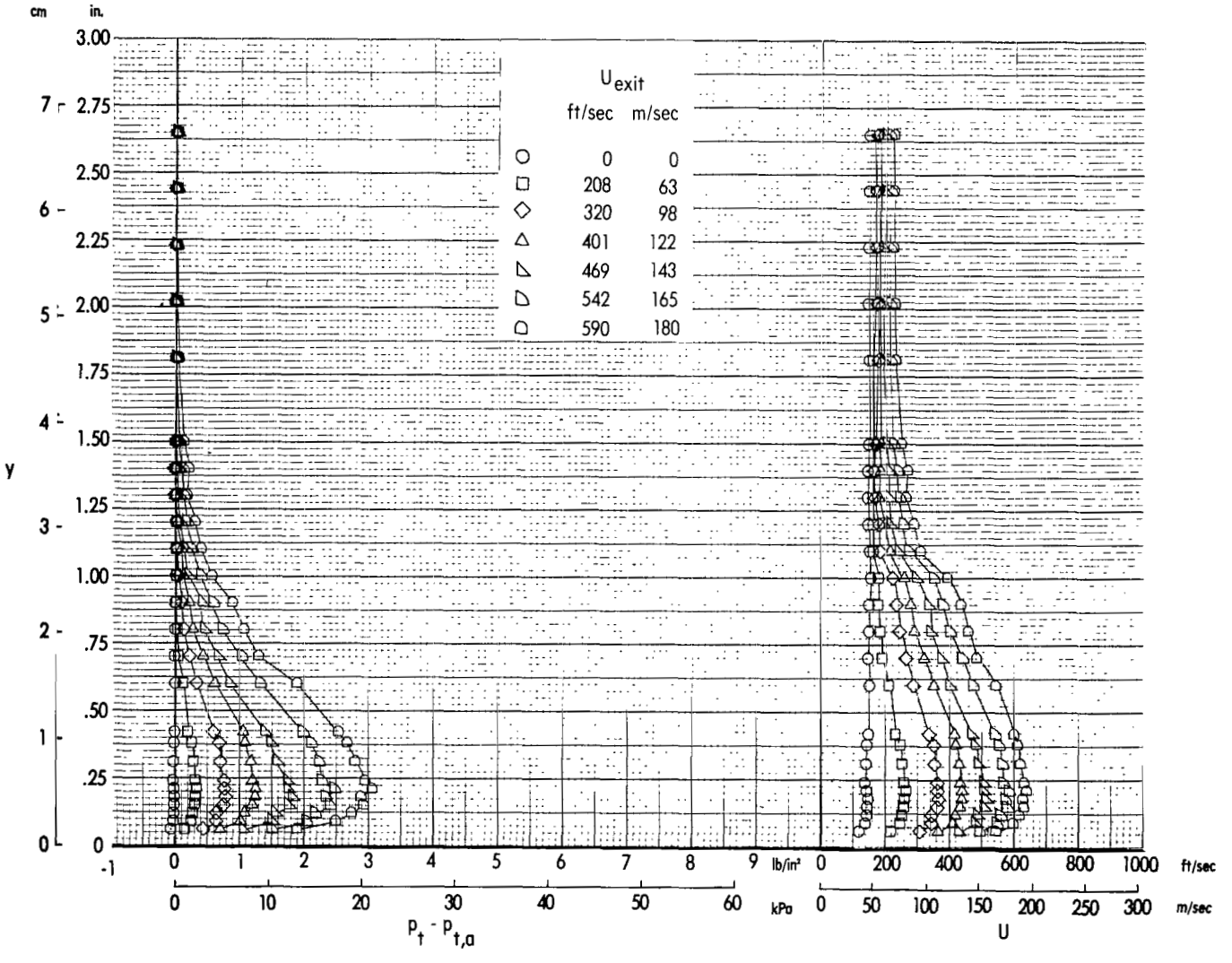

(i) x = 20.68 cm.

Figure 9.- Continued.

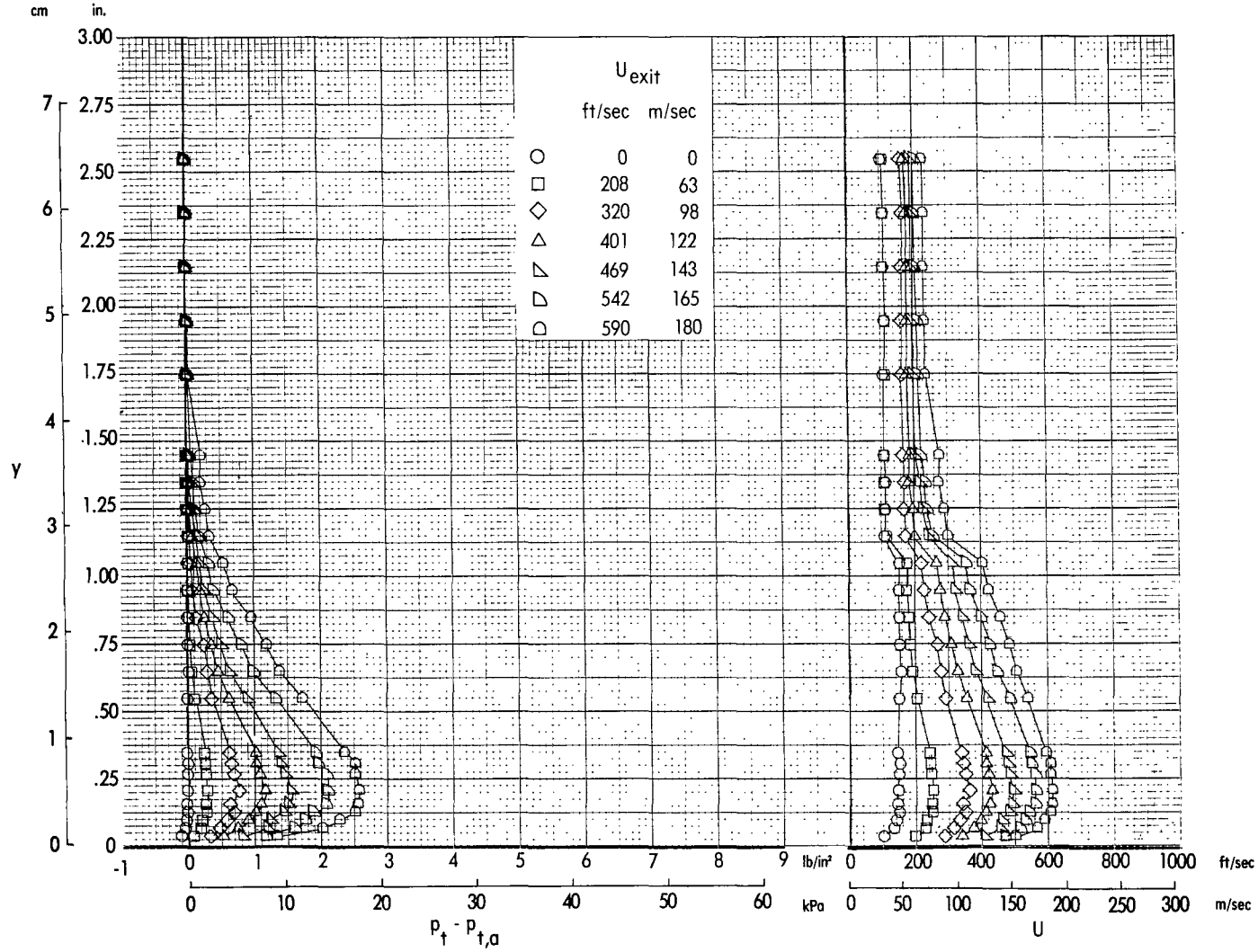

(j) x = 21.89 cm.

Figure 9.- Concluded.

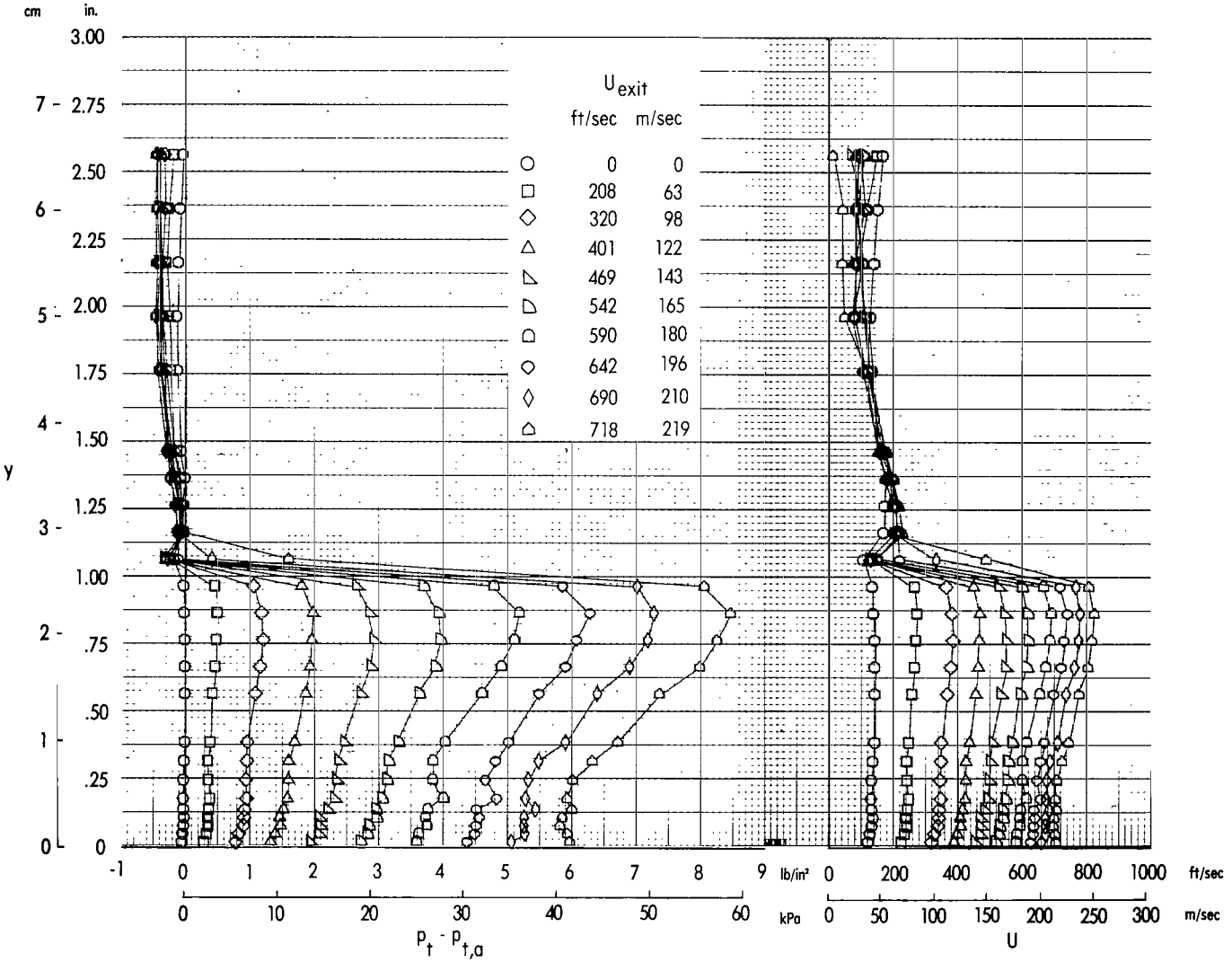

(a) x = 0 cm (nozzle exit).

Figure 10.- Jet velocity and total-pressure profiles with free-stream flow, obtained at various chordwise stations along the nacelle center line behind the nozzle exit. q = 766 Pa; $\alpha = 8^{o}$.

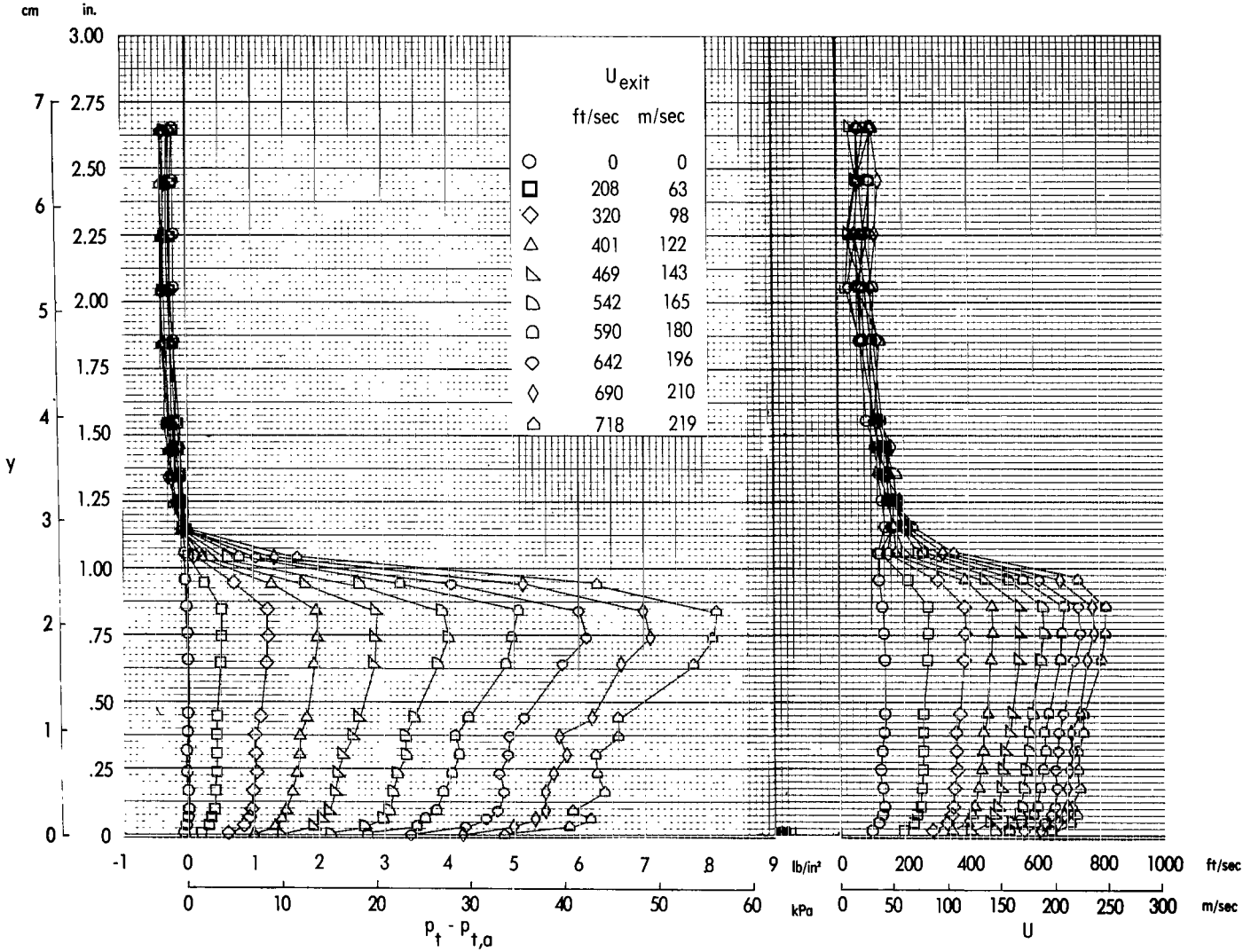

(b) x = 2.95 cm.

Figure 10.- Continued.

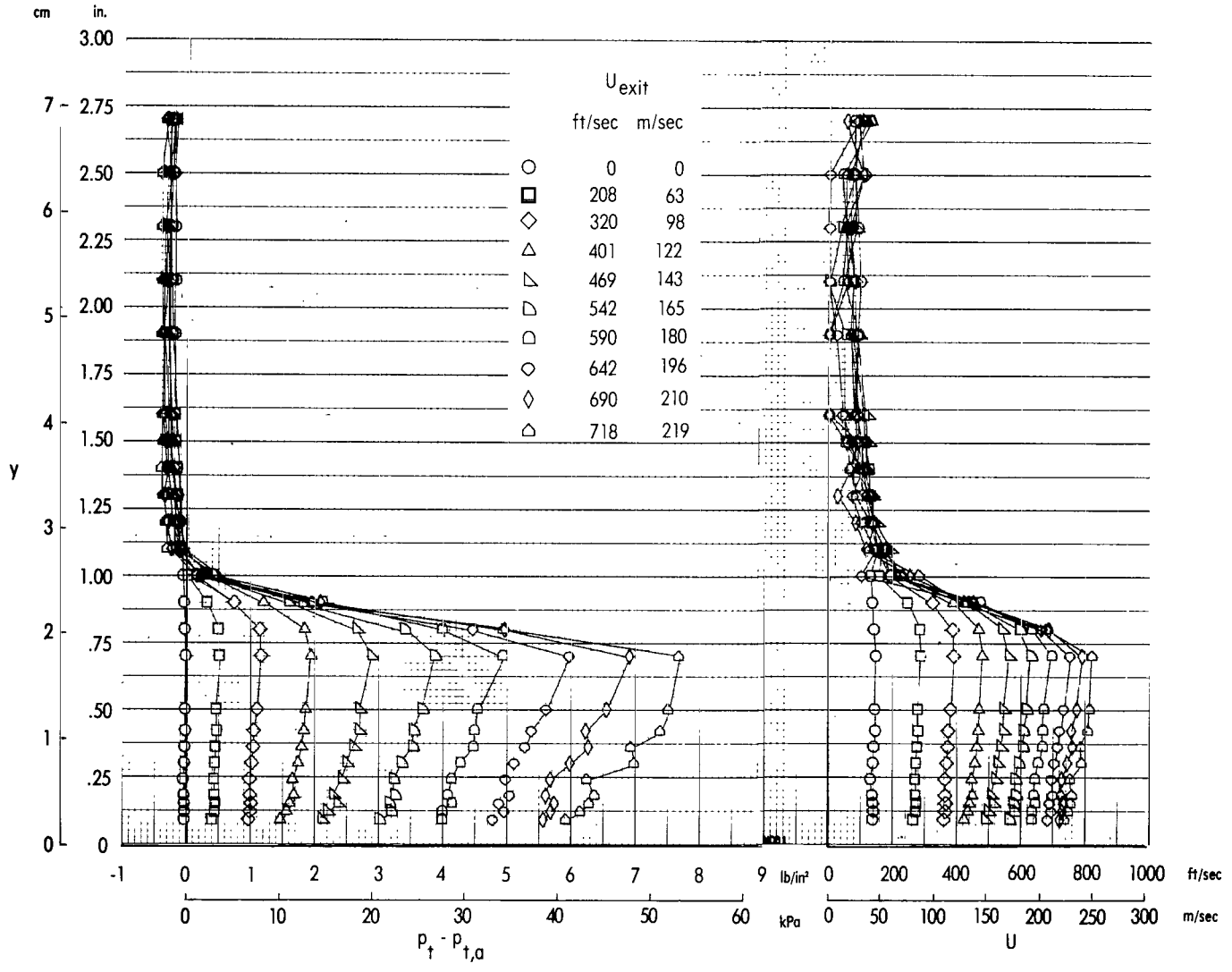

(c) x = 4.06 cm.

Figure 10.- Continued.

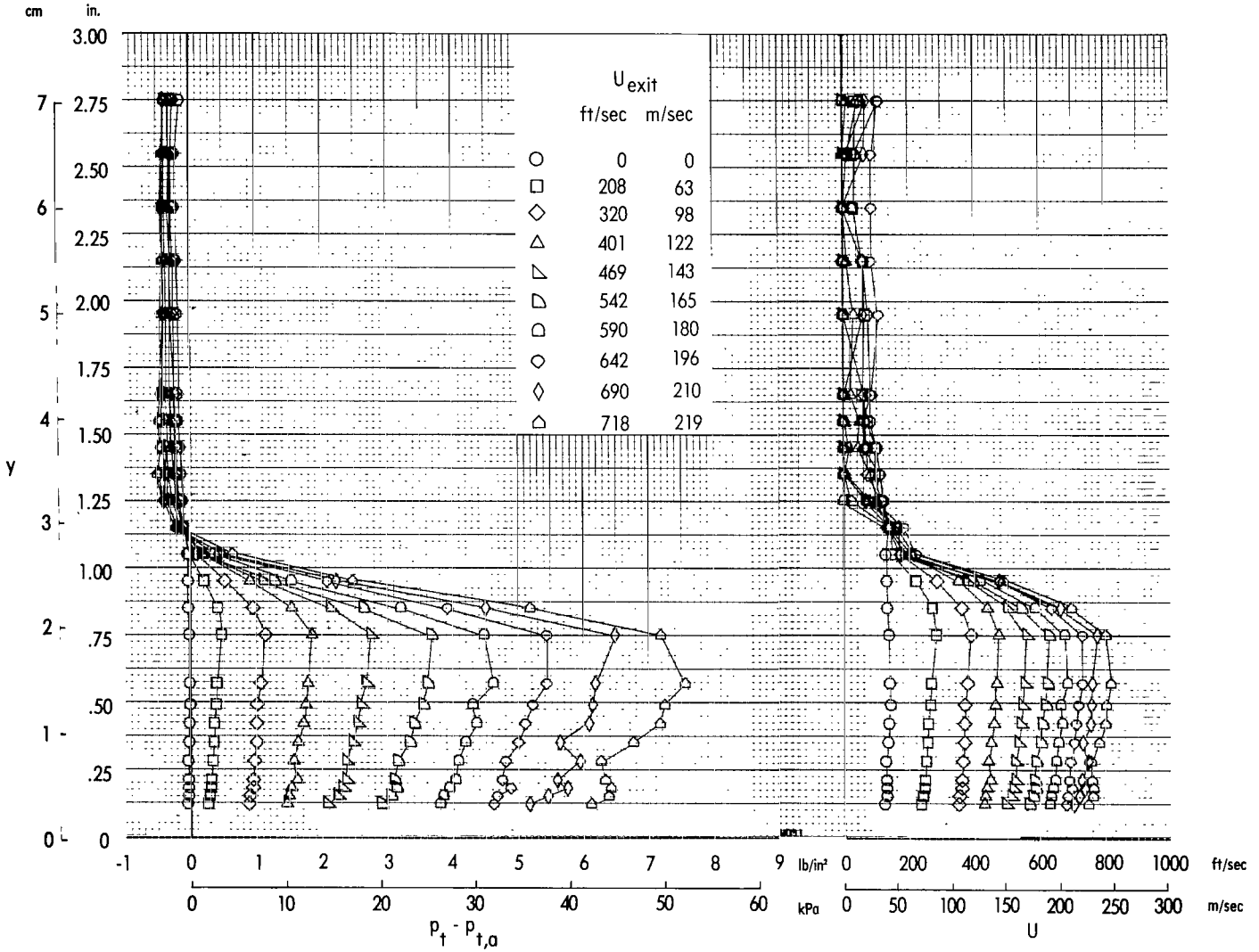

(d) x = 5.44 cm.

Figure 10.- Continued.

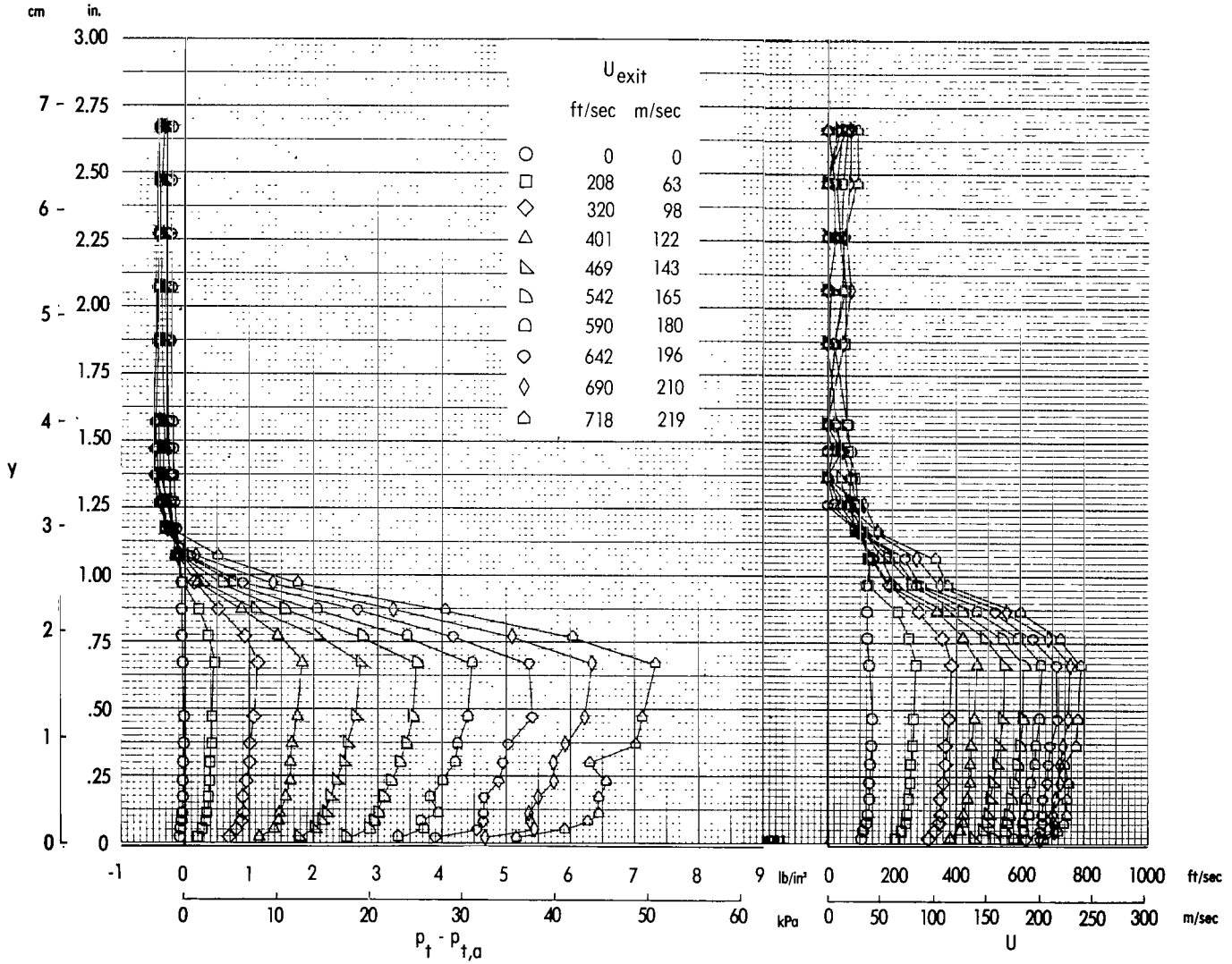

(e) x = 6.63 cm.

Figure 10.- Continued.

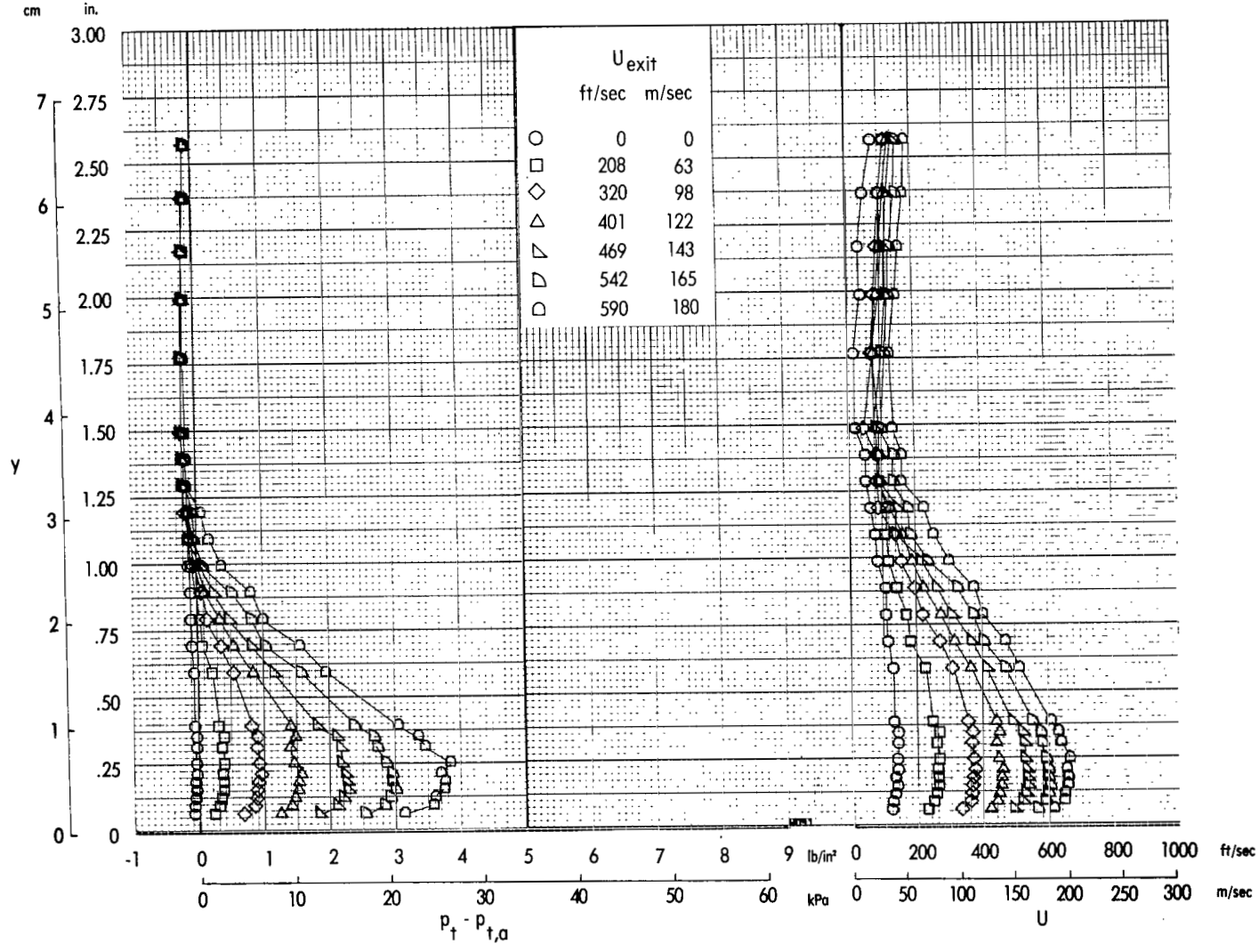

(f) x = 14.83 cm (flap knee).

Figure 10.- Continued.

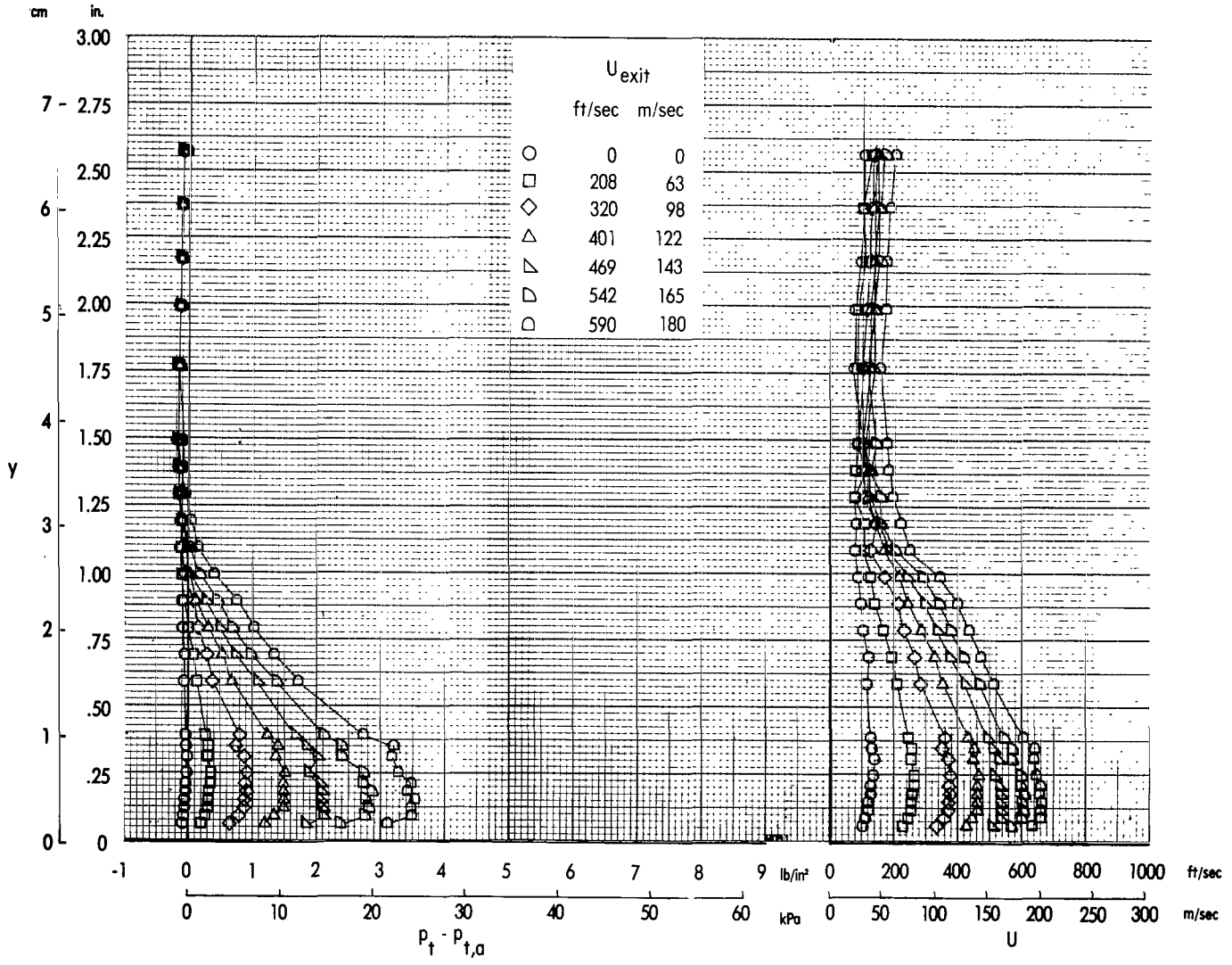

(g) x = 16.31 cm.

Figure 10.- Continued.

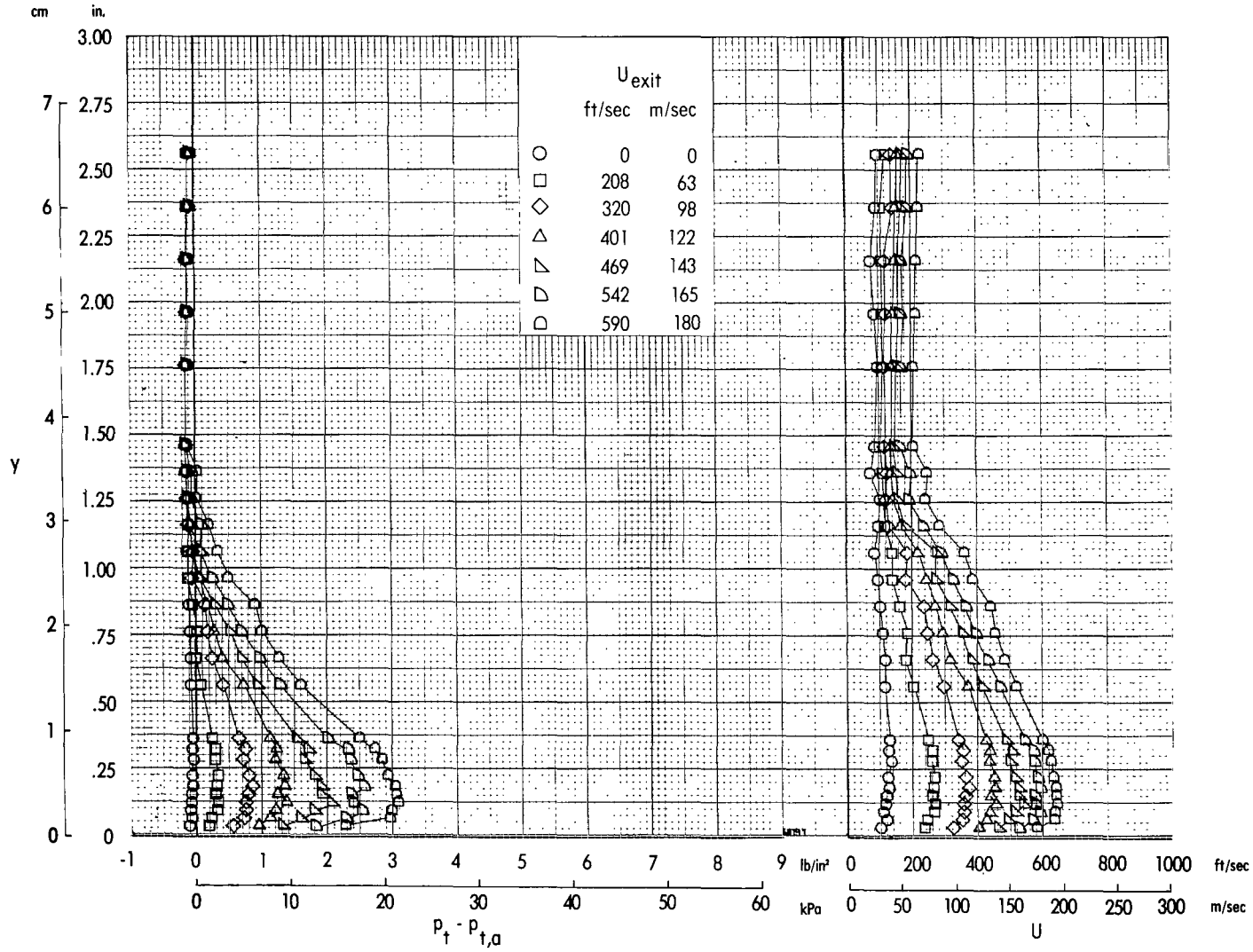

(h) x = 17.83 cm.

Figure 10.- Continued.

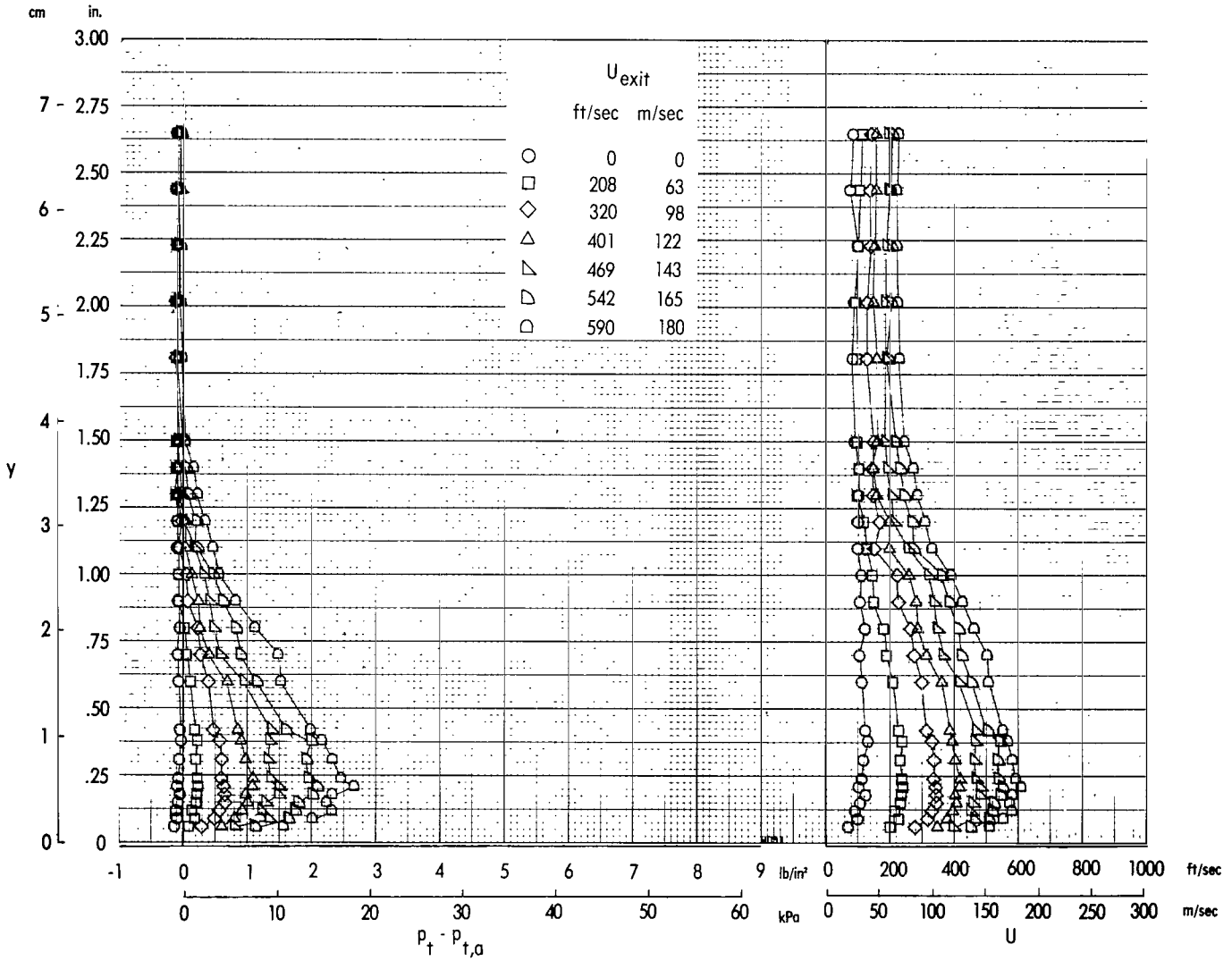

(i) x = 20.68 cm.

Figure 10.- Continued.

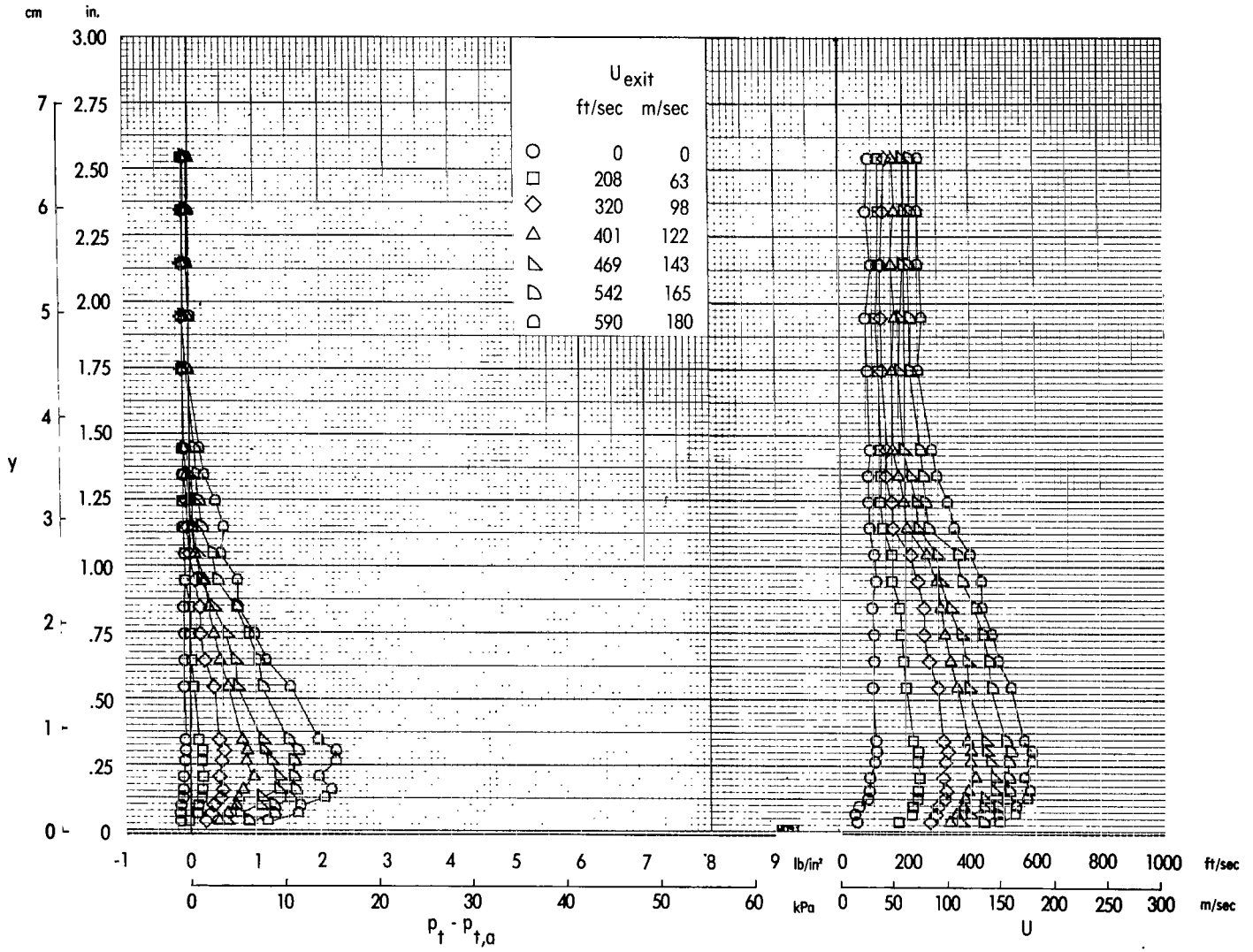

(j) x = 21.89 cm.

Figure 10.- Concluded.

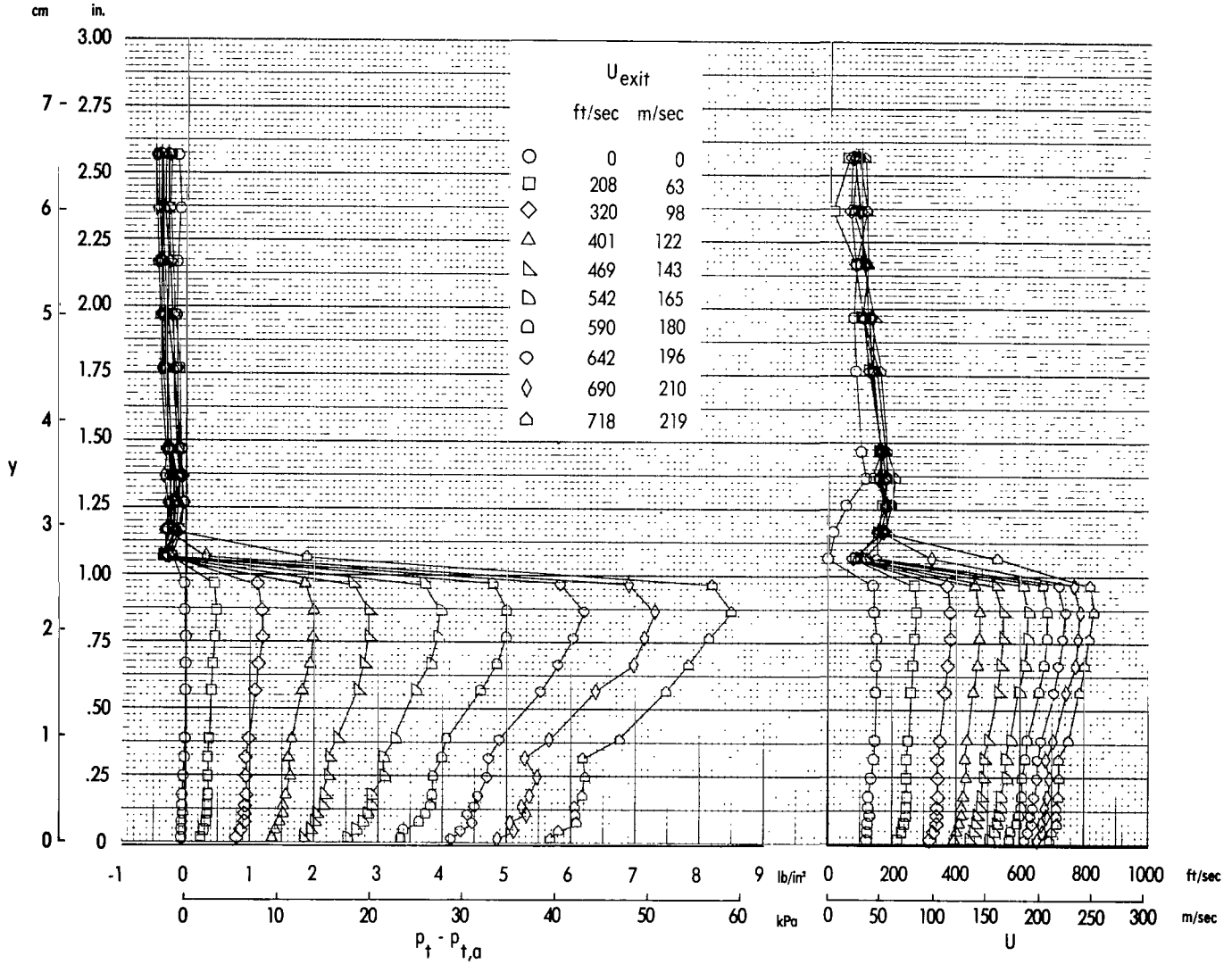

(a) x = 0 cm (nozzle exit).

Figure 11.- Jet velocity and total-pressure profiles with free-stream flow, obtained at various chordwise stations along the nacelle center line behind the nozzle exit. q = 766 Pa; $\alpha = 16^{o}$.

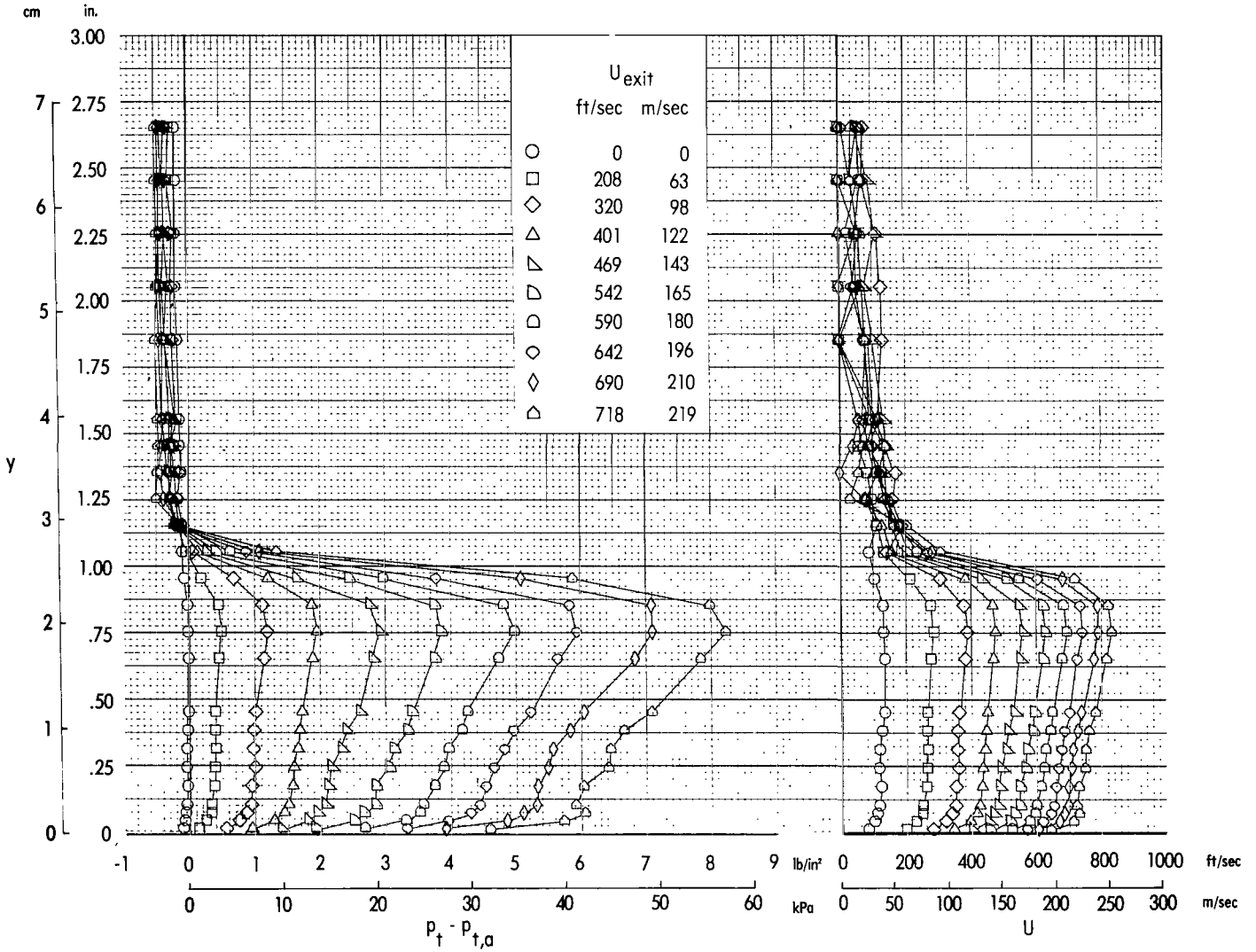

(b) x = 2.95 cm.

Figure 11.- Continued.

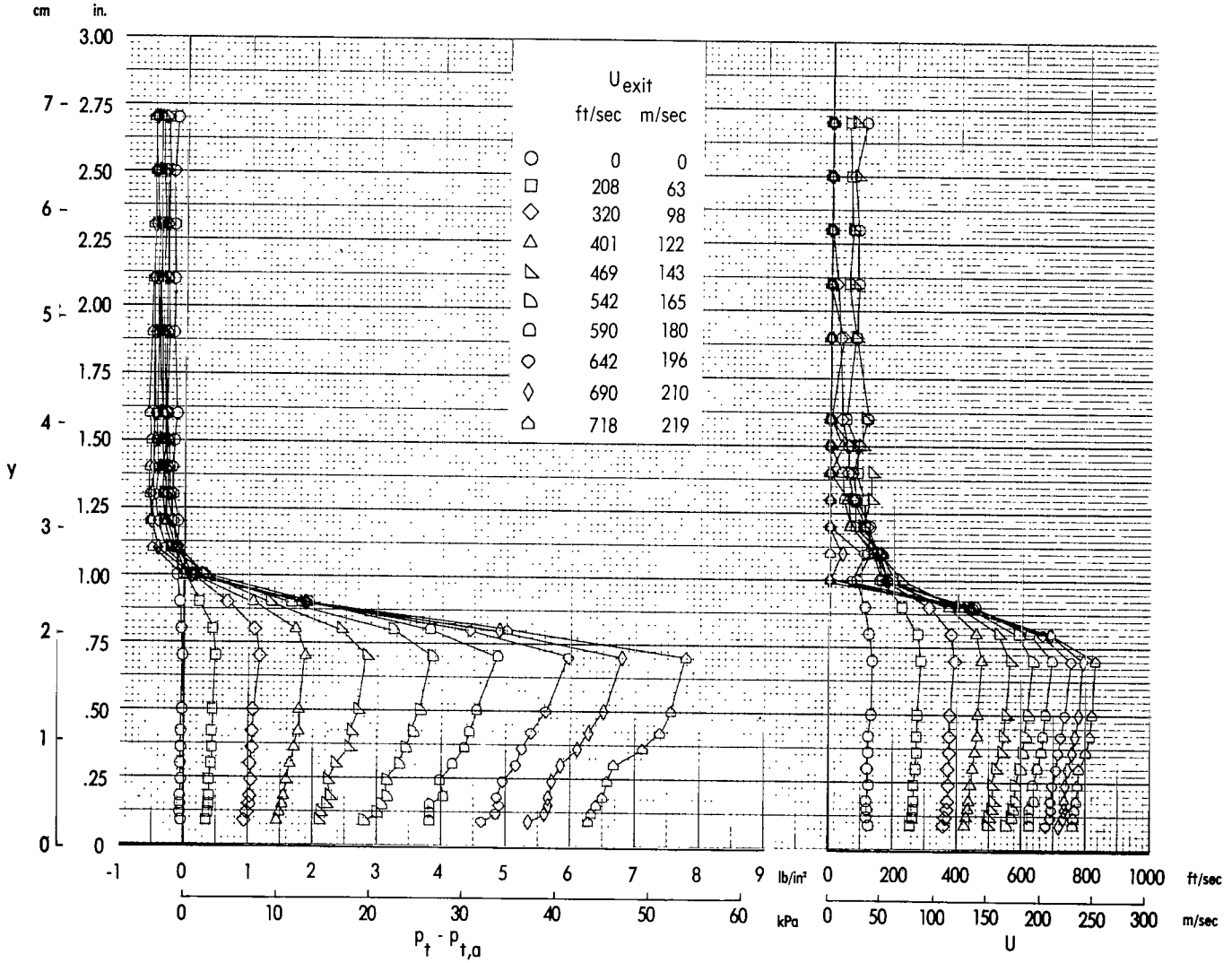

(c) x = 4.06 cm.

Figure 11.- Continued.

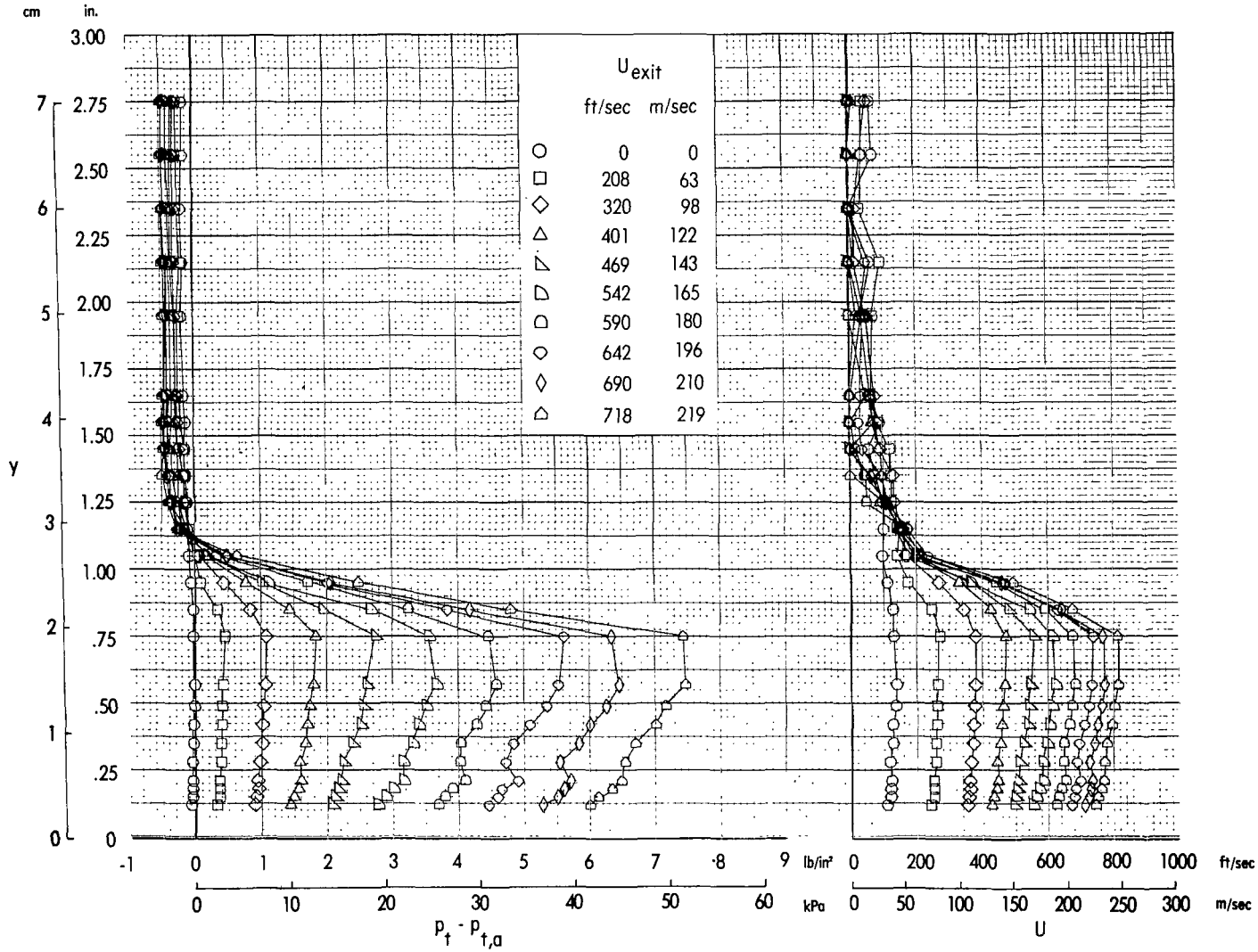

(d) x = 5.44 cm.

Figure 11.- Continued.

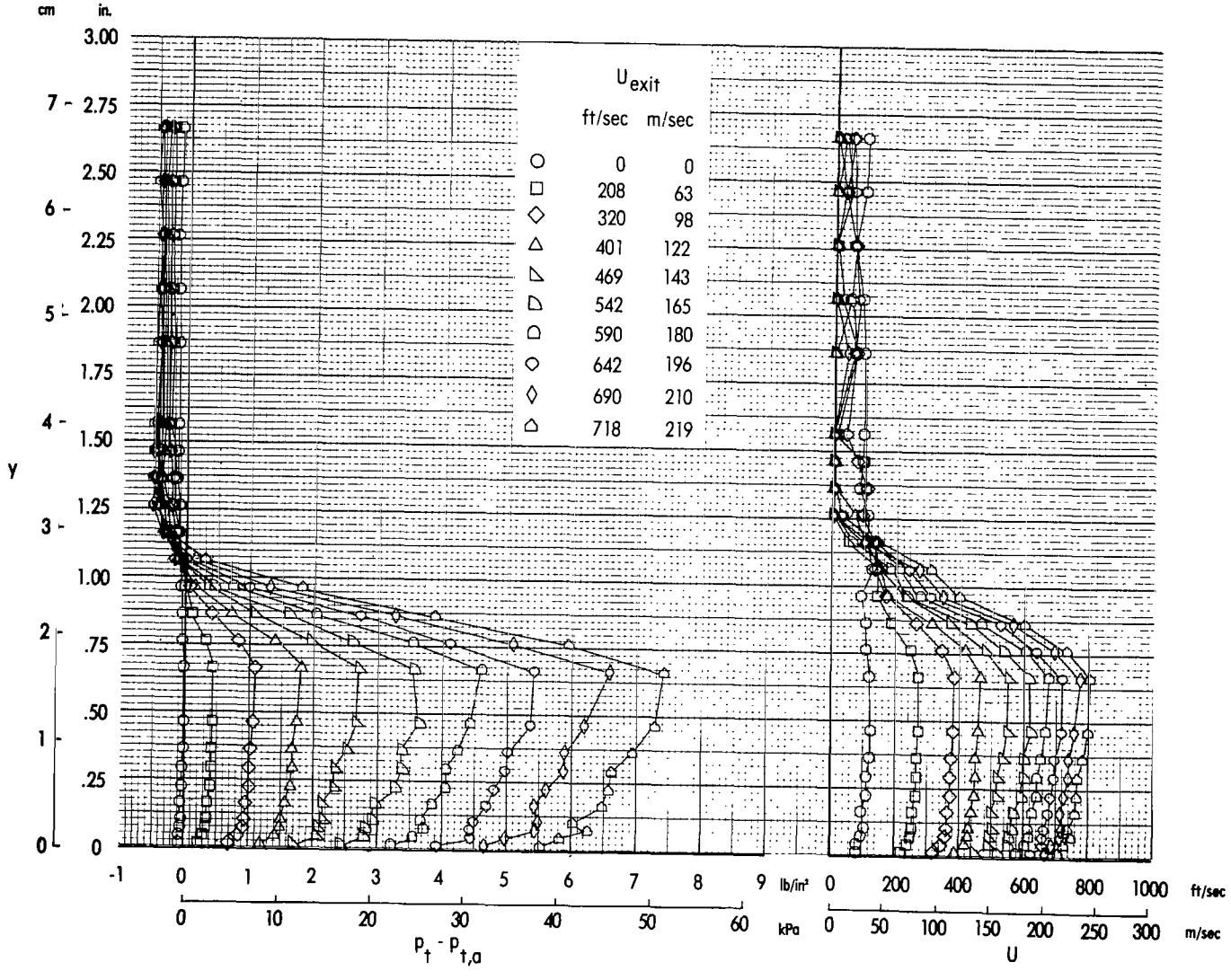

(e) x = 6.63 cm.

Figure 11.- Continued.

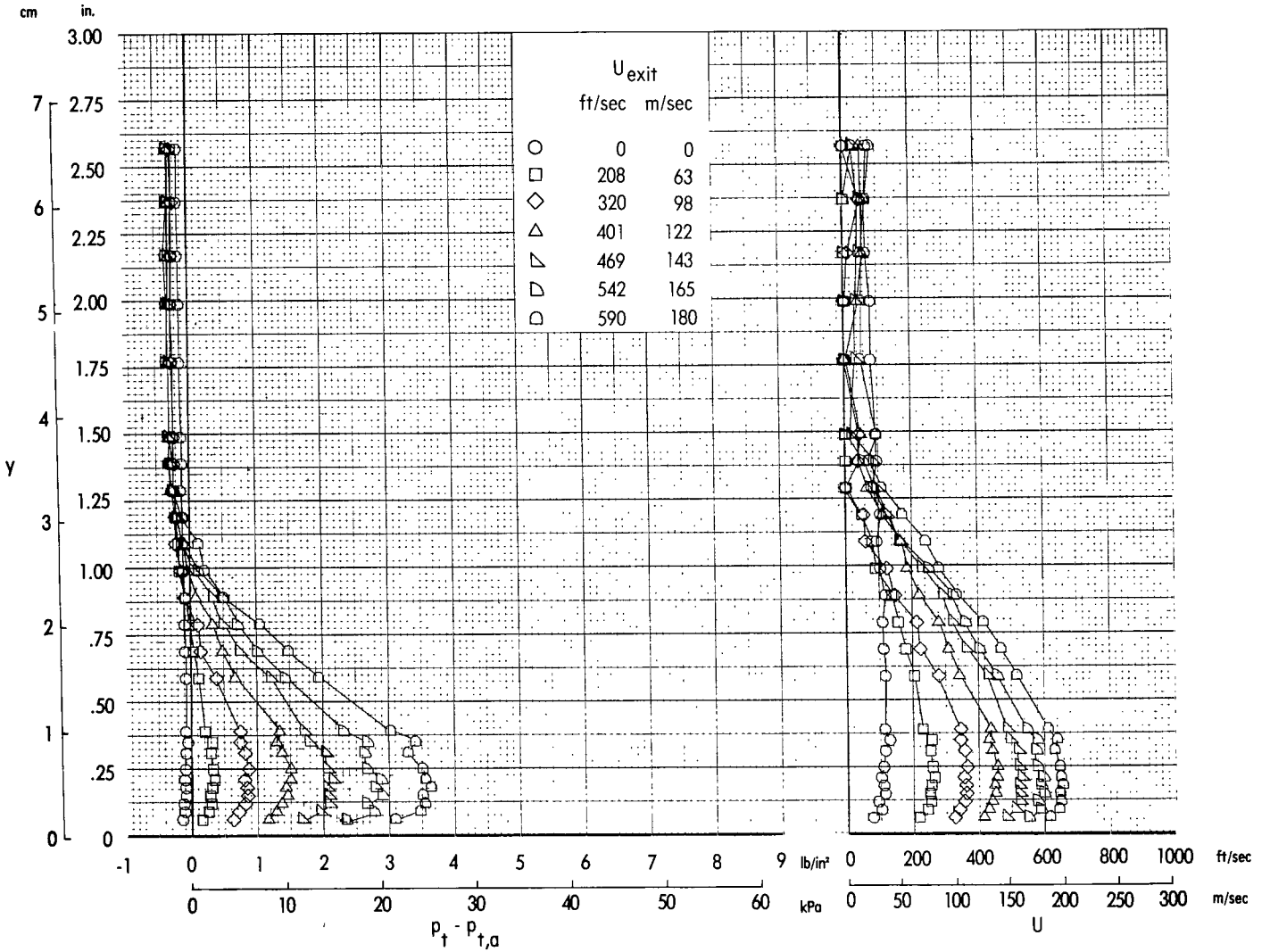

(f) x = 14.83 cm (flap knee).

Figure 11.- Continued.

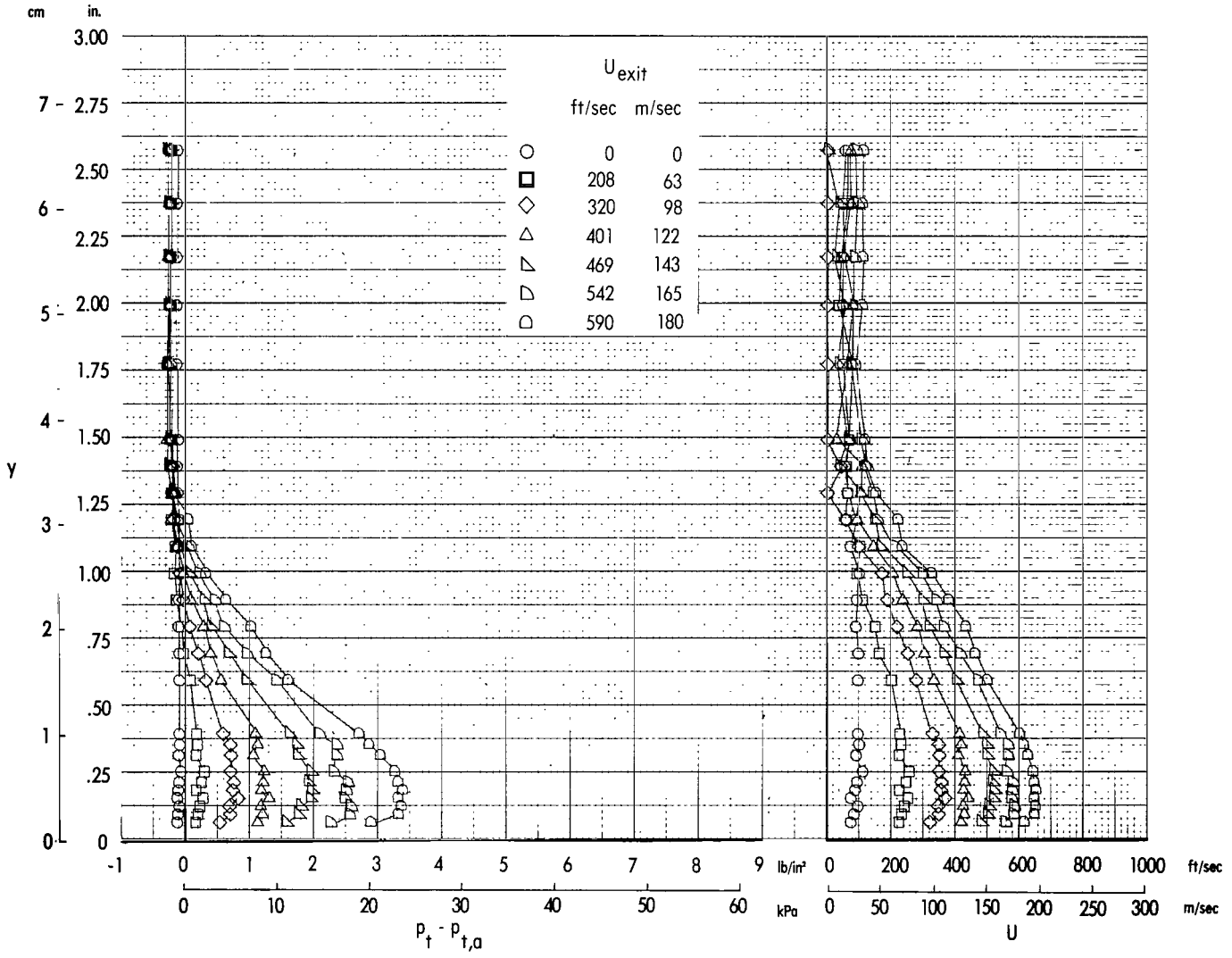

(g) x = 16.31 cm.

Figure 11.- Continued.

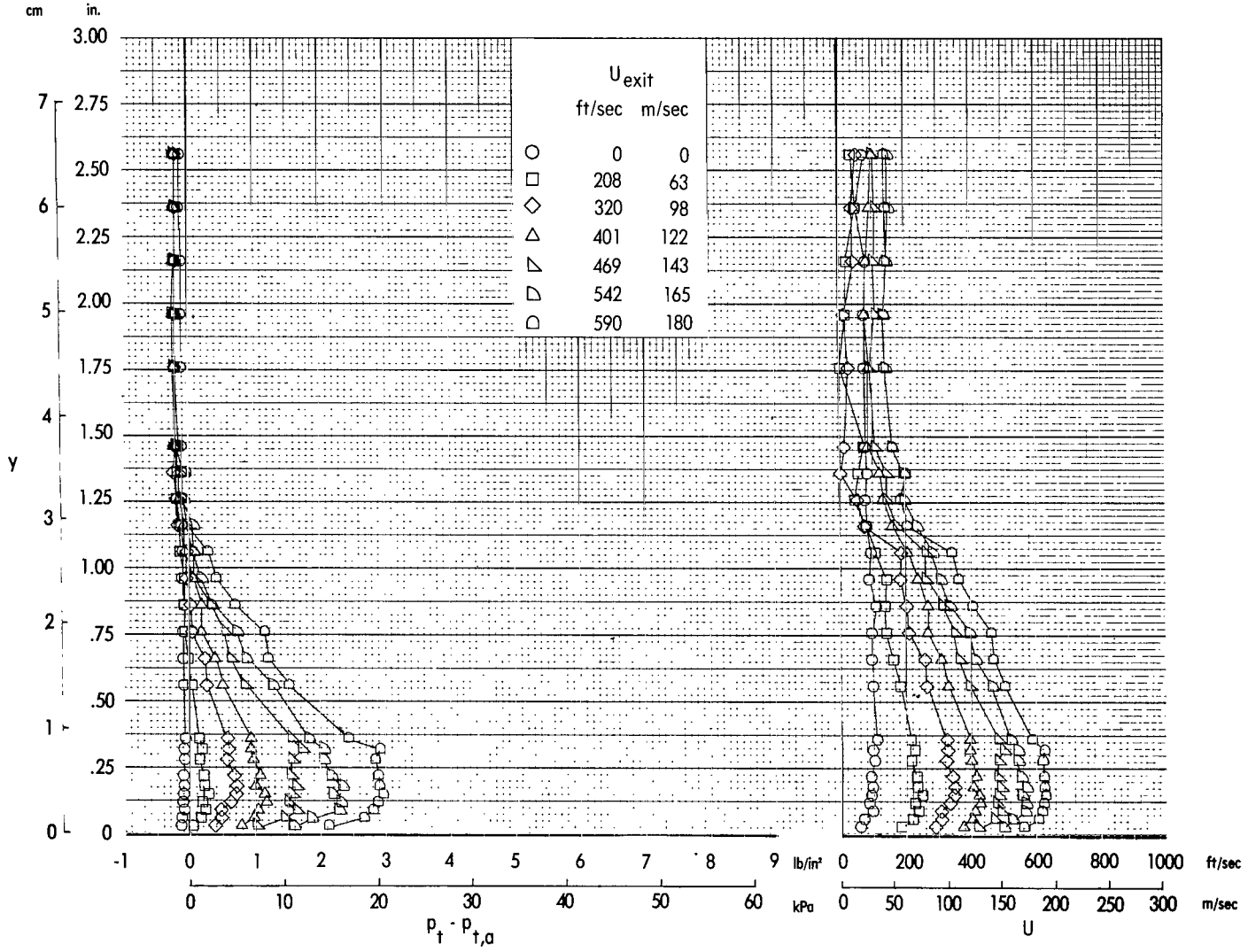

(h) x = 17.83 cm.

Figure 11.- Continued.

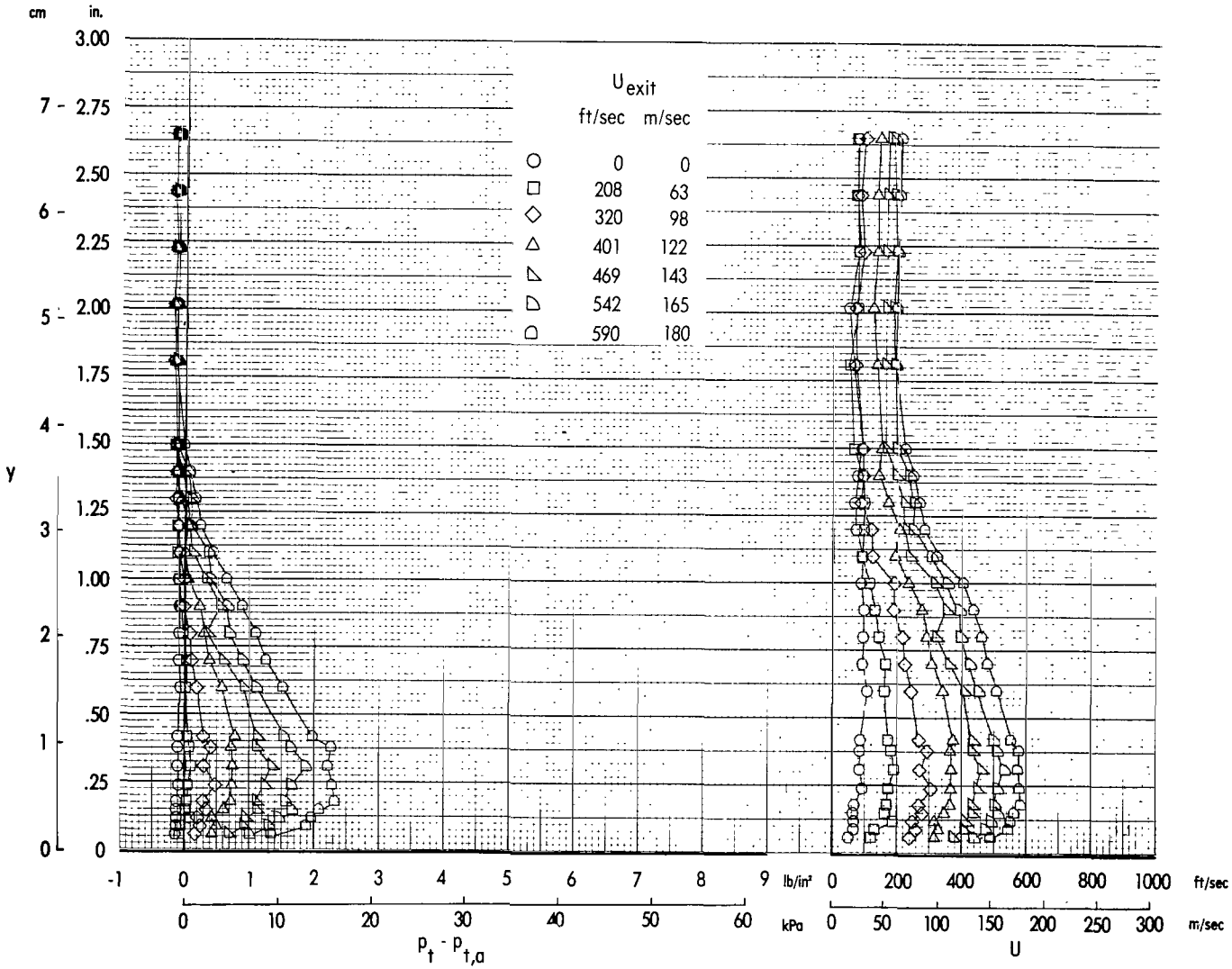

(i) x = 20.68 cm.

Figure 11.- Continued.

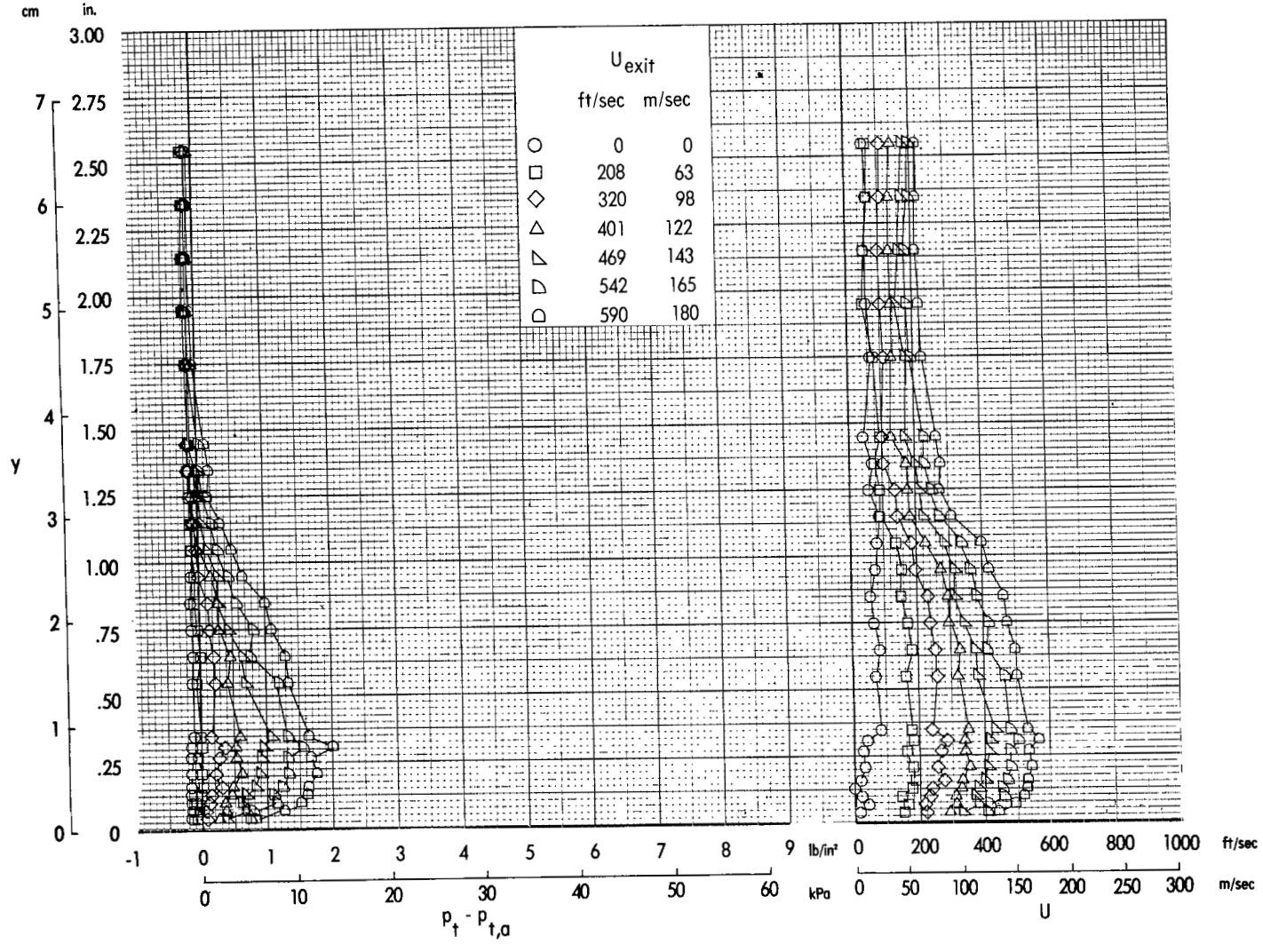

(j) x = 21.89 cm.

Figure 11.- Concluded.

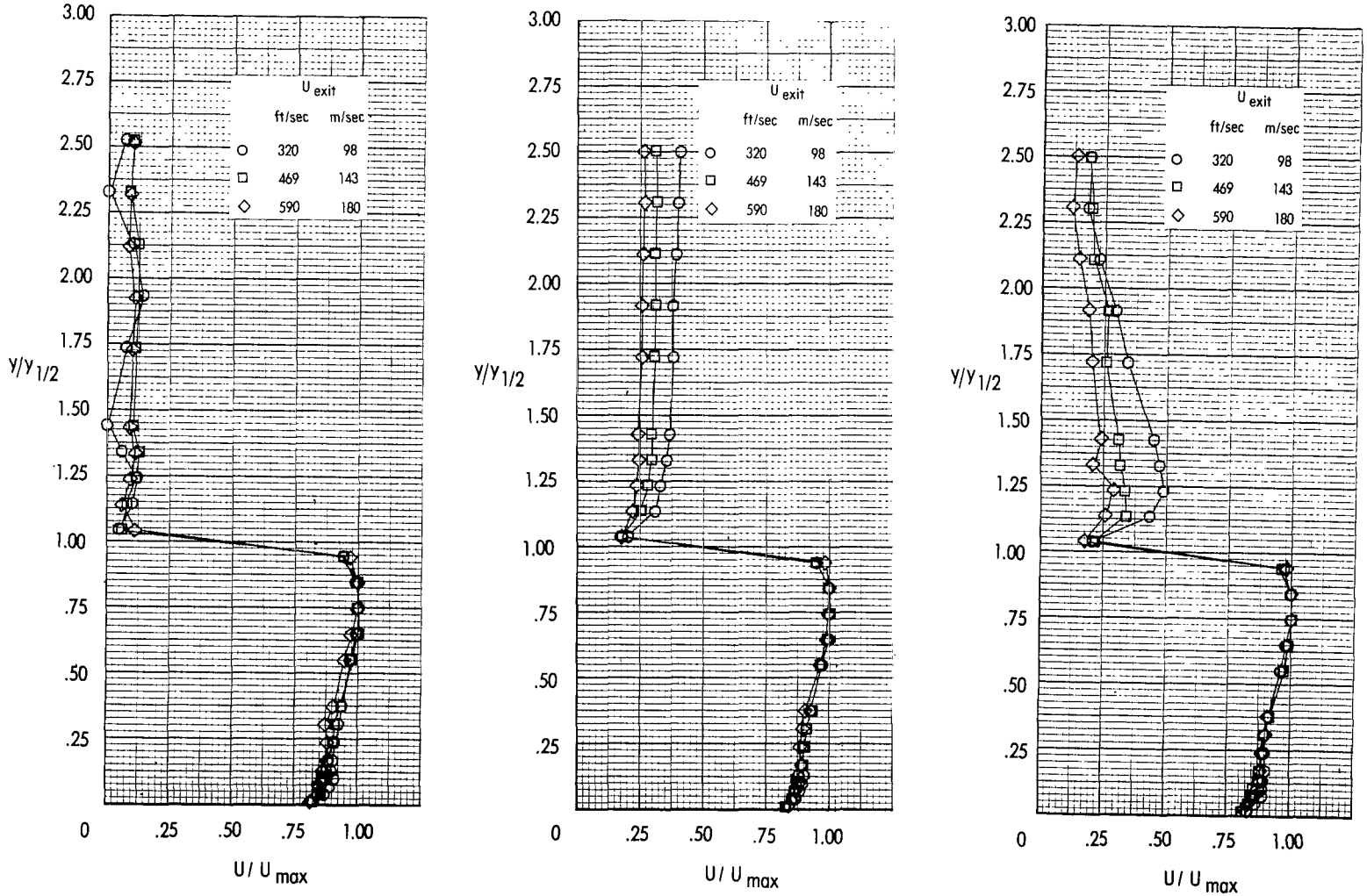

(a) $\alpha = 0^{o}$, static data. (b) $\alpha = 0^{o}$, q = 766 Pa. (c) $\alpha = 16^{o}$, q = 766 Pa.

Figure 12.- Effect of jet exit velocity on nondimensional velocity profiles obtained at nozzle exit, x = 0.

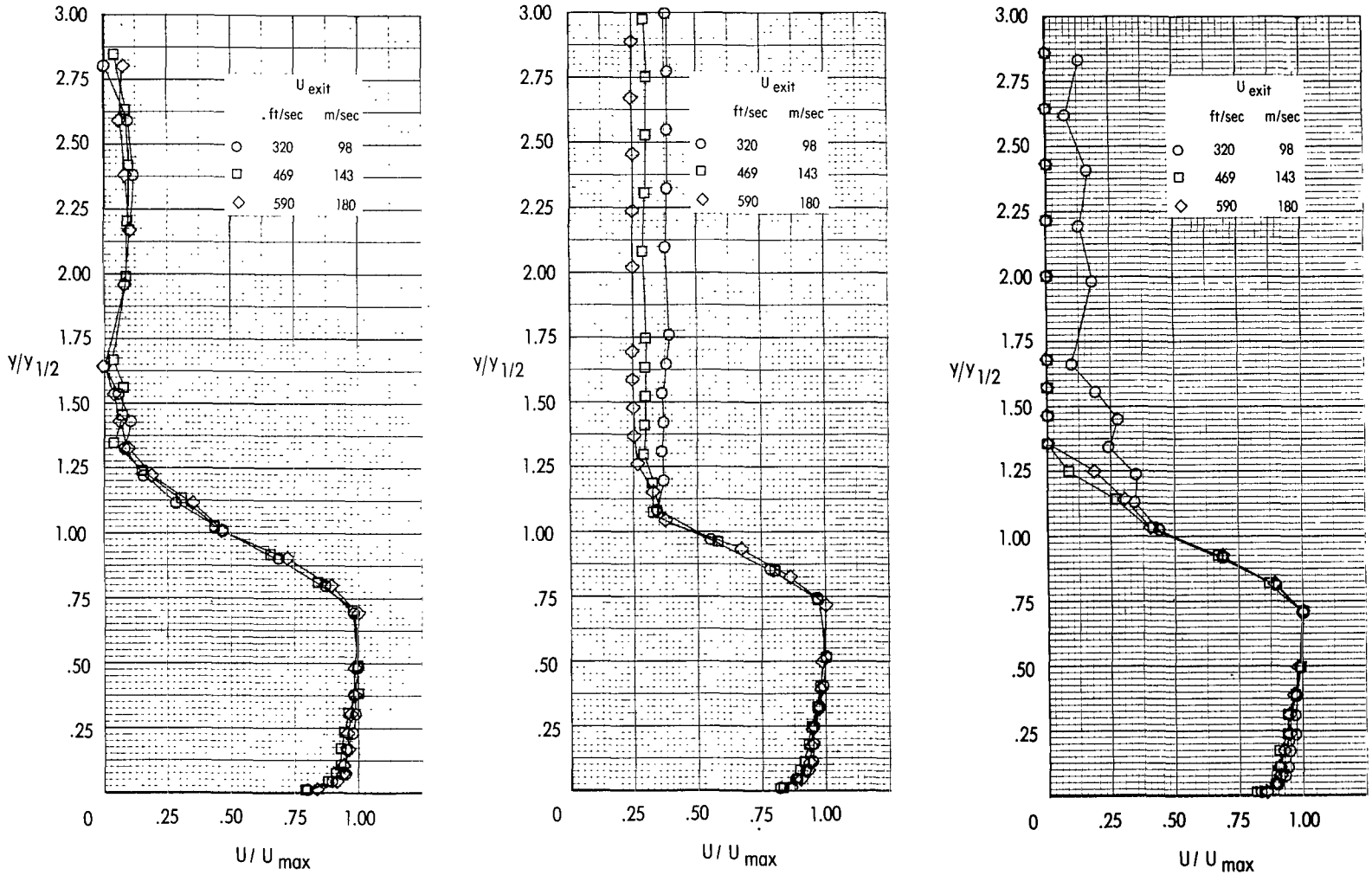

(a) $\alpha = 0^{o}$, static data. (b) $\alpha = 0^{o}$, q = 766 Pa. (c) $\alpha = 16^{o}$, q = 766 Pa.

Figure 13.- Effect of jet exit velocity on nondimensional velocity profiles obtained over wing, x = 6.63 cm.

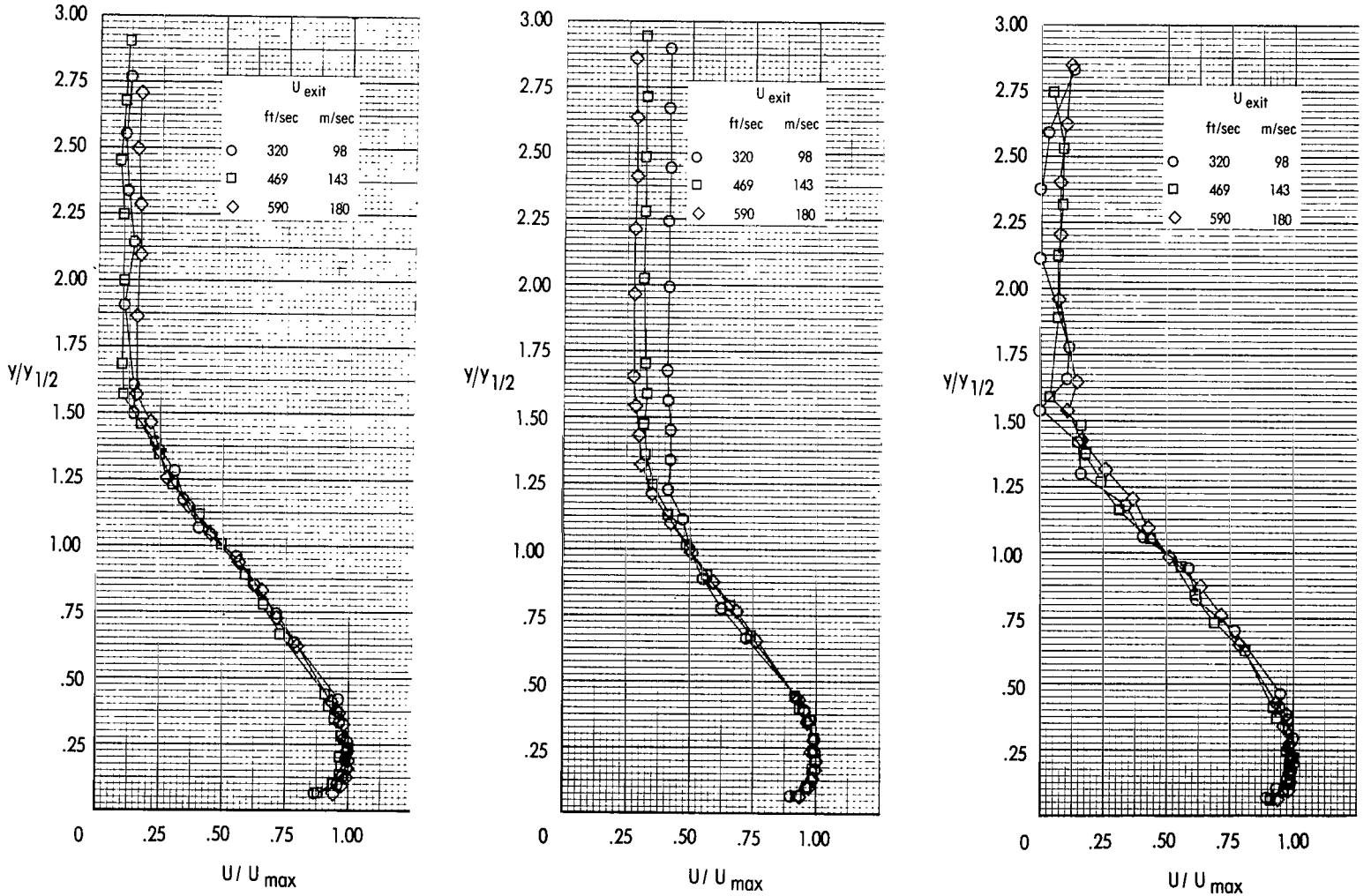

(a) $\alpha = 0^{o}$, static data.

(b) $\alpha = 0^{o}$, q = 766 Pa.

(c) $\alpha = 16^{o}$, q = 766 Pa.

Figure 14.- Effect of jet exit velocity on nondimensional velocity profiles obtained at flap knee, x = 14.83 cm.

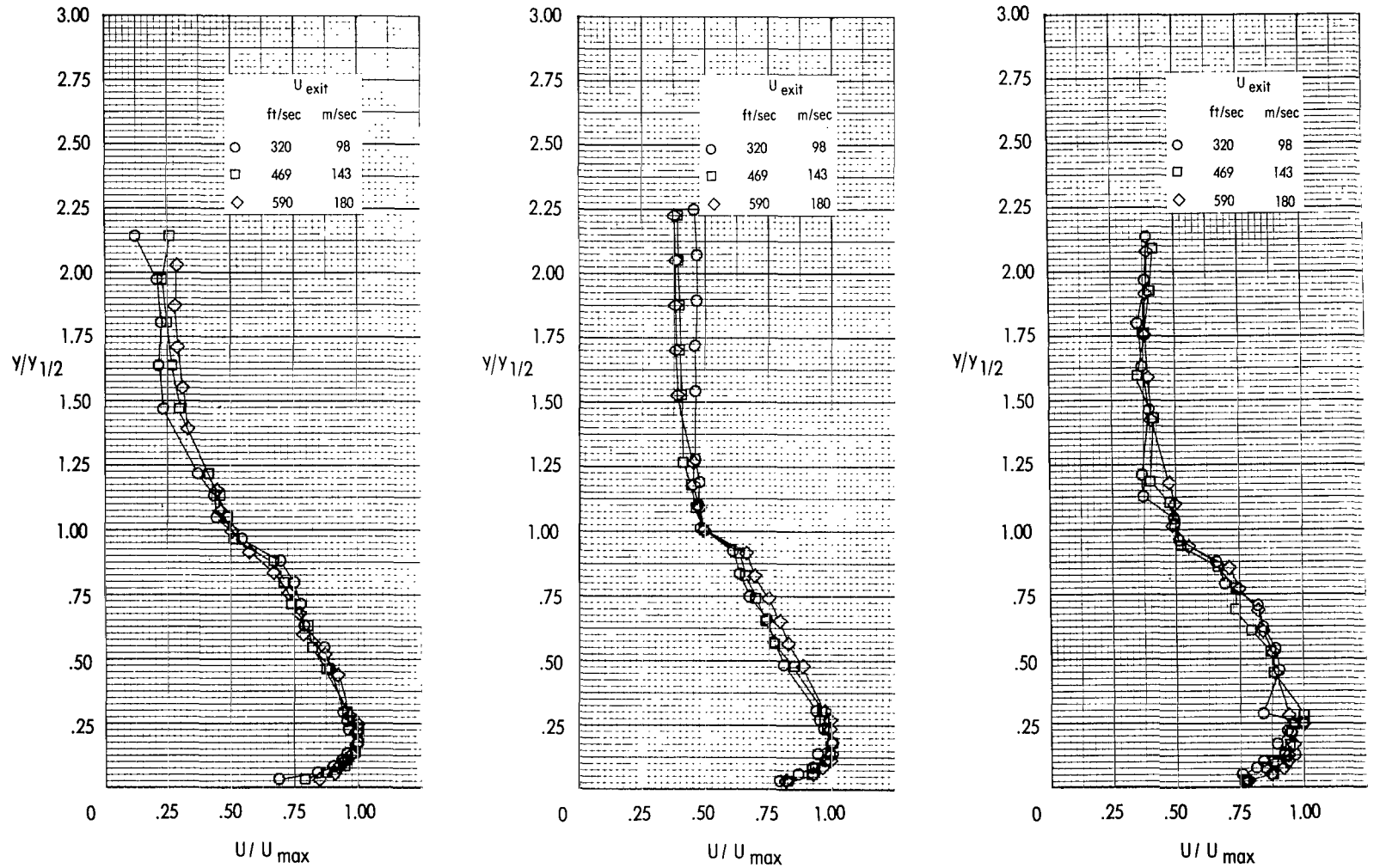

(a) $\alpha = 0^{o}$, static data.

(b) $\alpha = 0^{o}$, q = 766 Pa.

(c) $\alpha = 16^{o}$, q = 766 Pa.

Figure 15.- Effect of jet exit velocity on nondimensional velocity profiles obtained at rearmost position on radius flap, x = 21.89 cm.

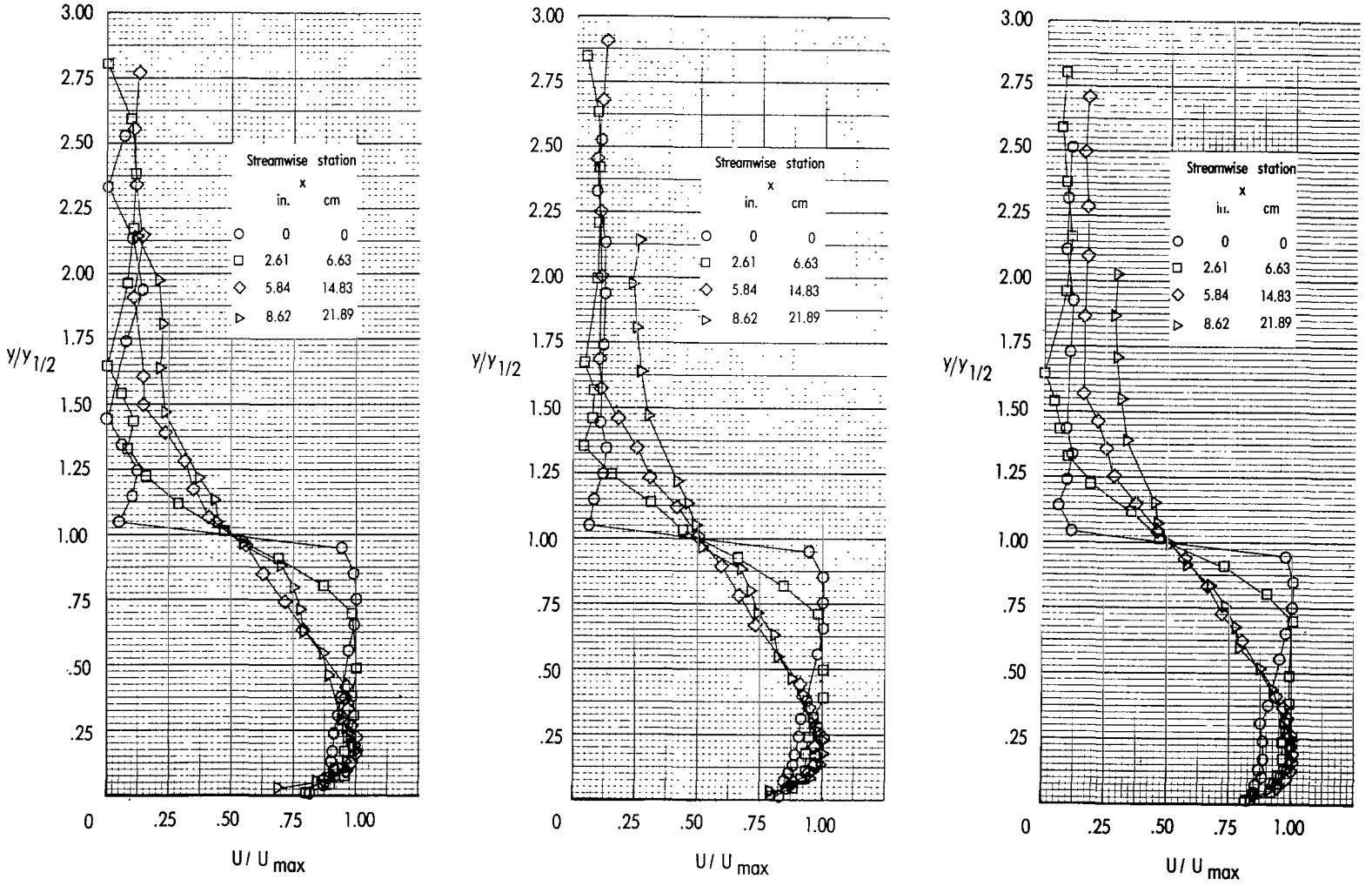

(a) U_{exit} = 320 m/sec.

(b) U_{exit} = 469 m/sec.

(c) U_{exit} = 590 m/sec.

Figure 16.- Effect of survey-rake location on nondimensional velocity profiles obtained for static jet. $\alpha = 0^{o}$; wind off.

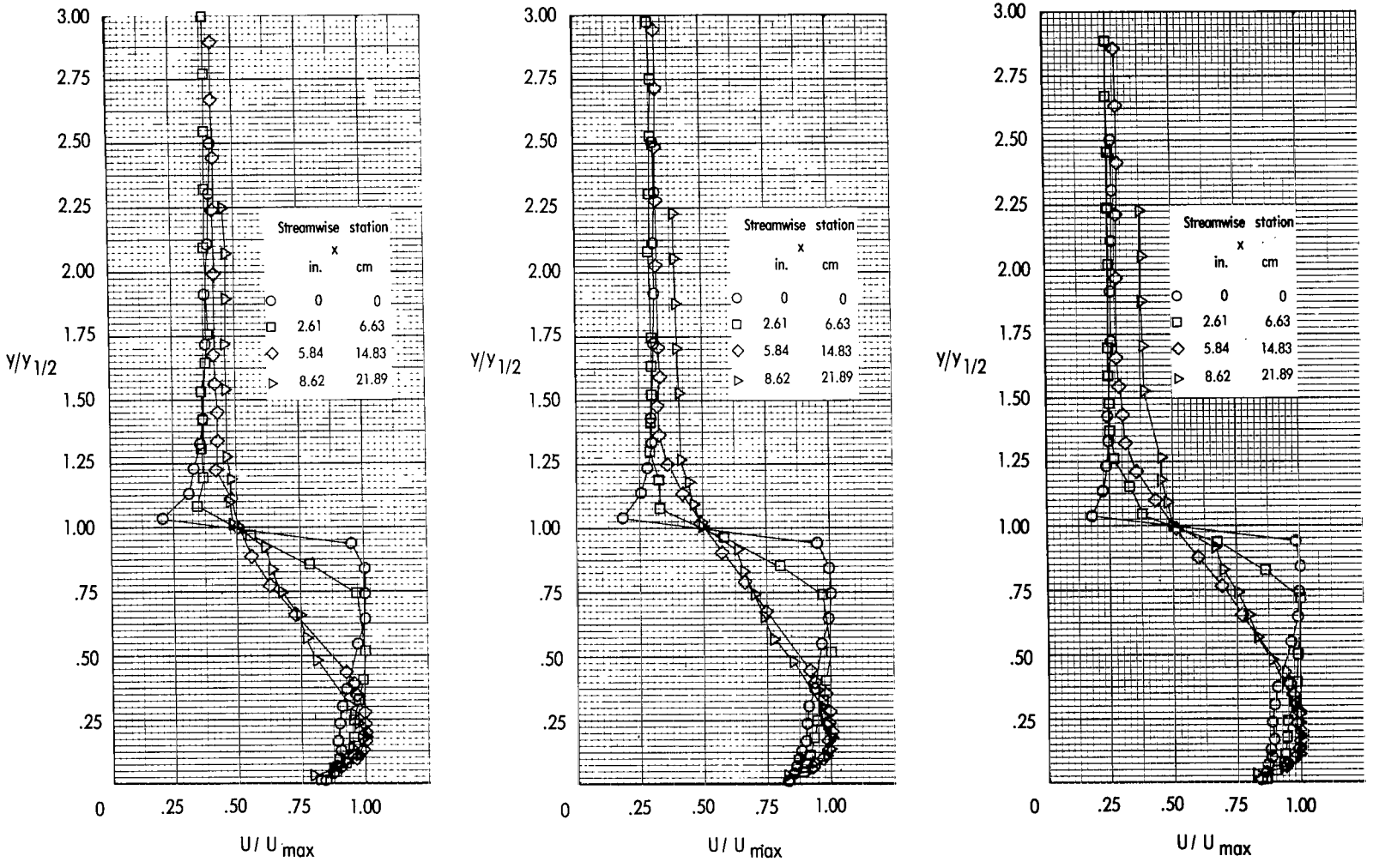

(a) U_{exit} = 320 m/sec. (b) U_{exit} = 469 m/sec. (c) U_{exit} = 590 m/sec.

Figure 17.- Effect of survey-rake location on nondimensional velocity profiles obtained with free-stream flow at $\alpha = 0^{o}$ and q = 766 Pa.

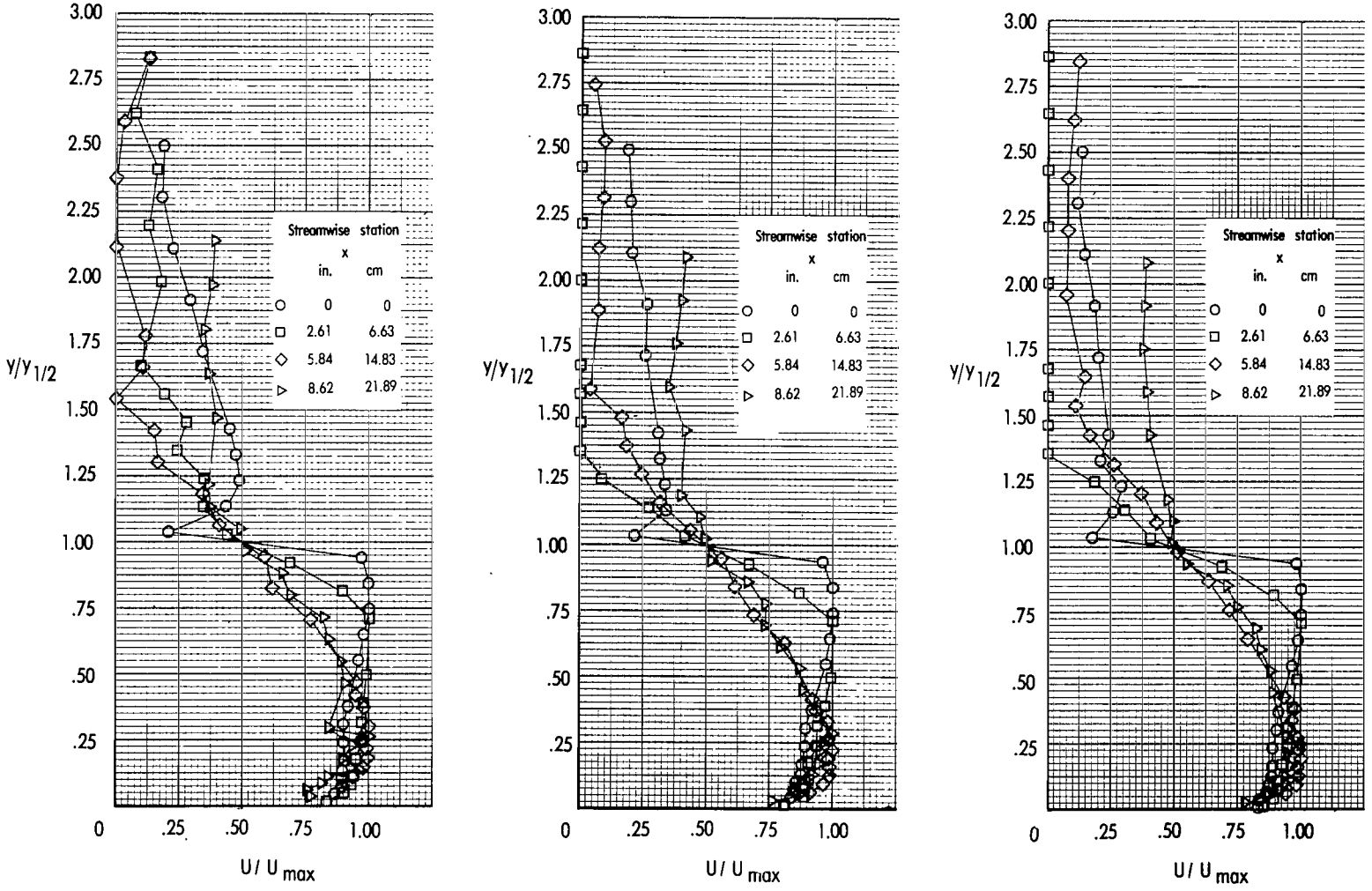

(a) U_{exit} = 320 m/sec. (b) U_{exit} = 469 m/sec. (c) U_{exit} = 590 m/sec.

Figure 18.- Effect of survey-rake location on nondimensional velocity profiles obtained with free-stream flow at $\alpha = 16^{o}$ and q = 766 Pa.

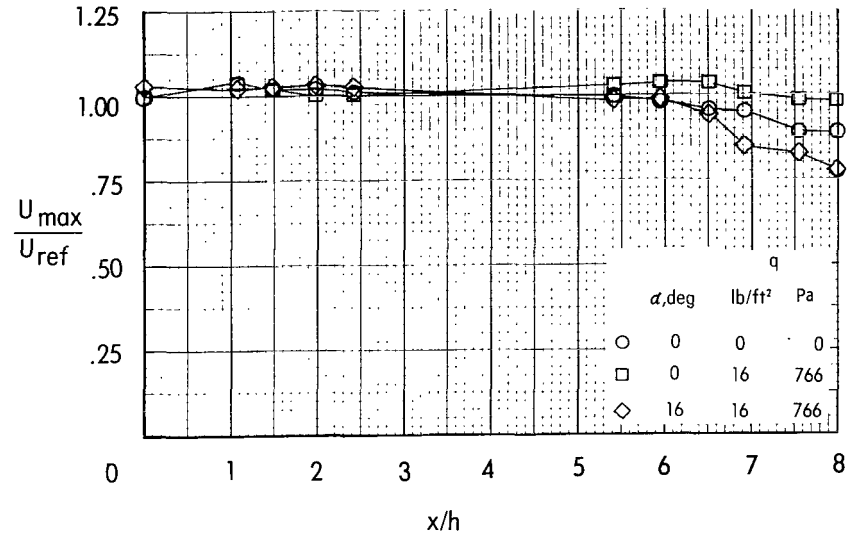

(a) Jet velocity decay.

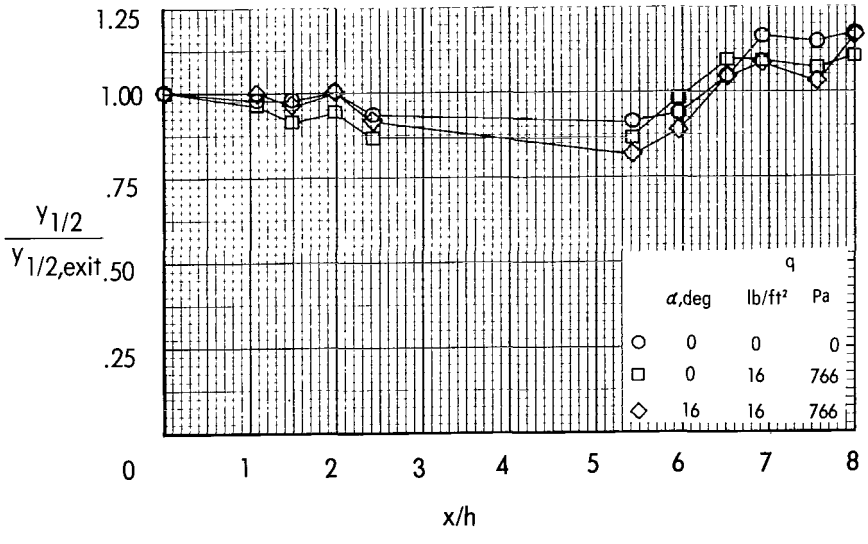

(b) Jet thickness characteristics.

Figure 19.- Jet velocity decay and thickness characteristics for a low value of jet exit velocity, U_{exit} = 320 m/sec.

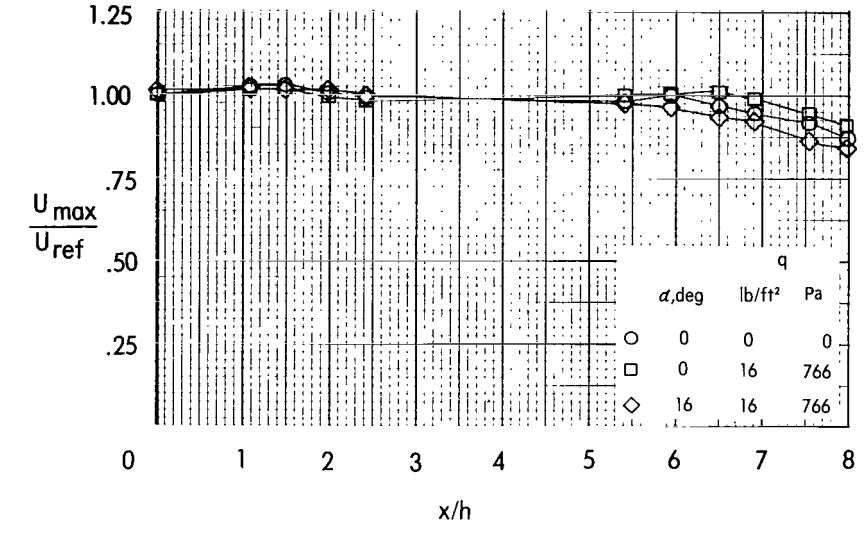

(a) Jet velocity decay.

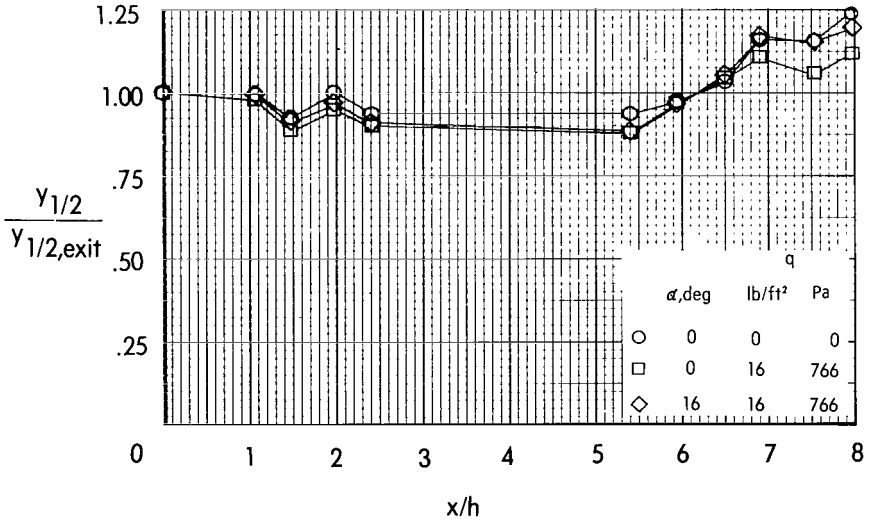

(b) Jet thickness characteristics.

Figure 20.- Jet velocity decay and thickness characteristics for a high value of jet exit velocity, U_{exit} = 590 m/sec.

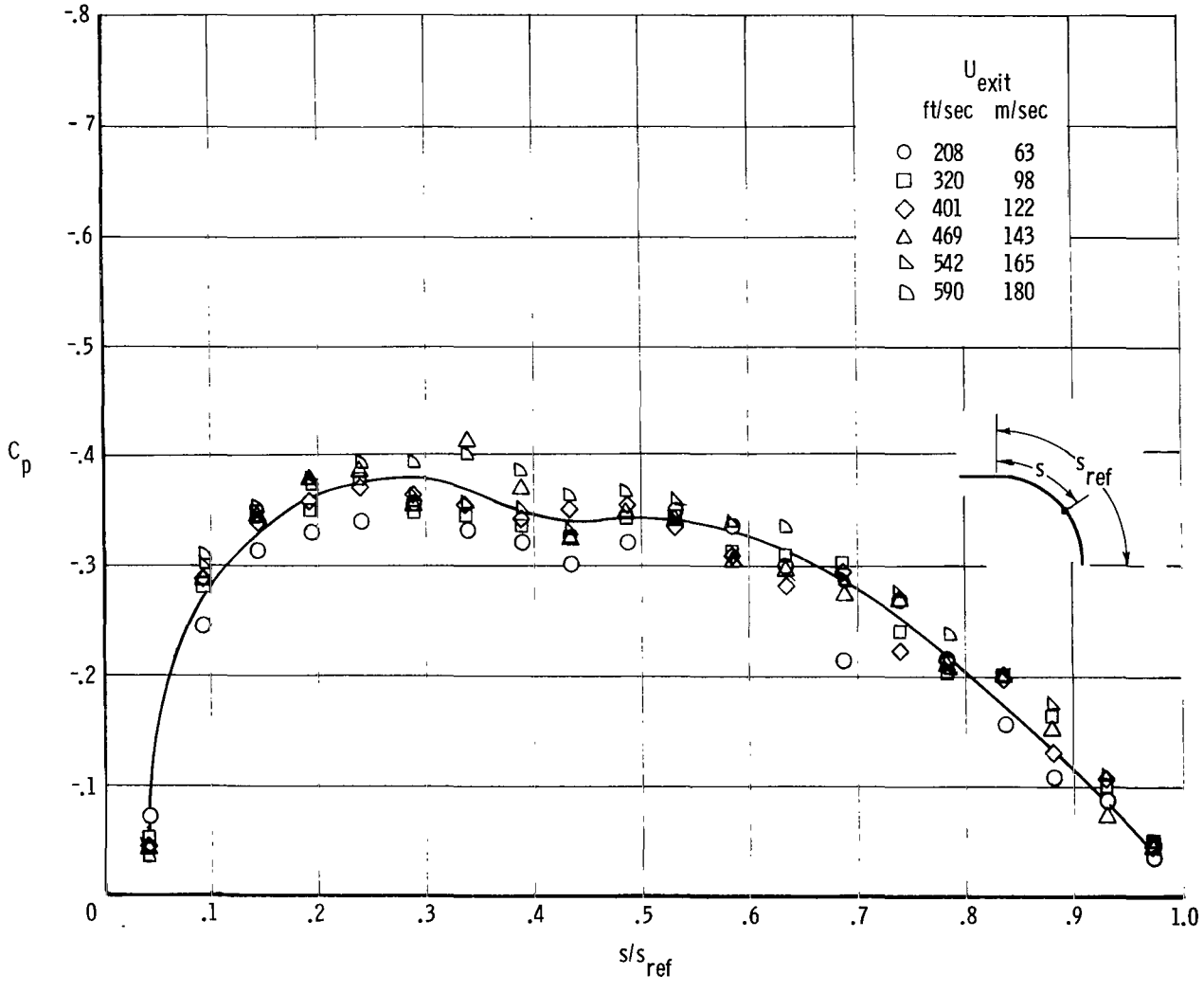

Figure 21.- Static-pressure distribution over upper surface of radius flap with static jet.

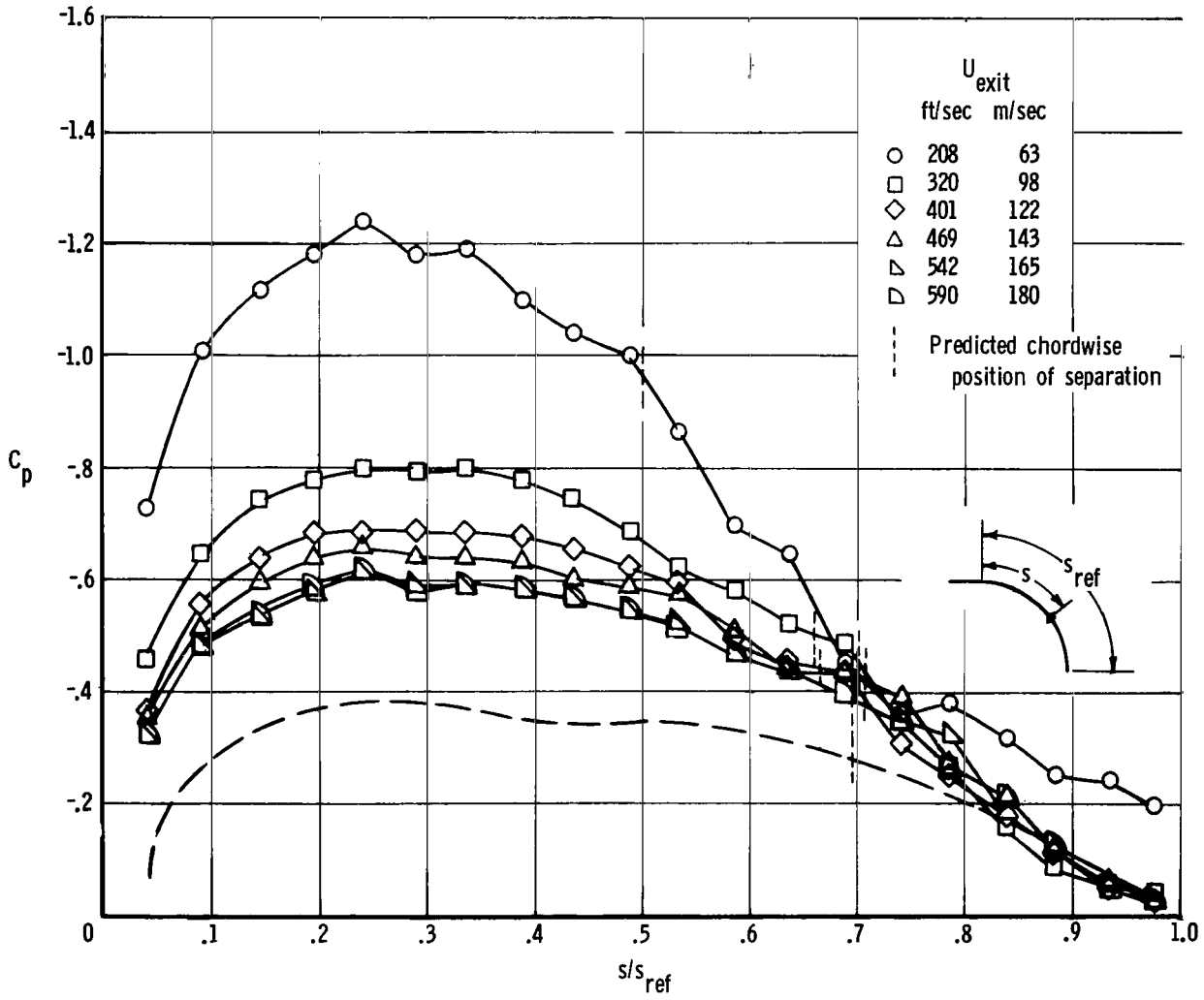

Figure 22.- Static-pressure distributions over upper surface of radius flap with jet in presence of free-stream flow. $\alpha = 0^{o}$, q = 766 Pa. (Distribution for static condition shown by dashed-line curve.)

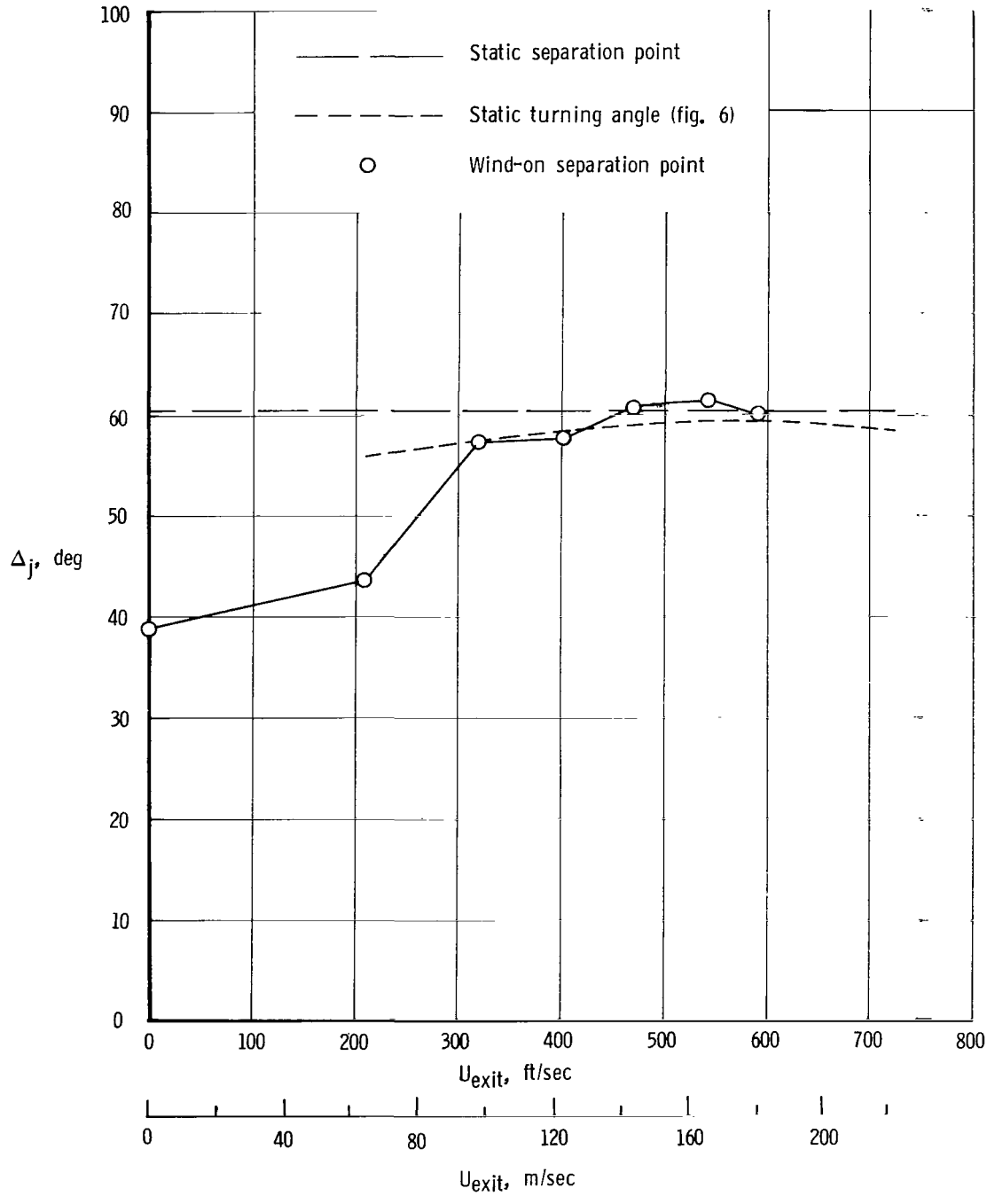

Figure 23.- Comparison of static and wind-on separation points, determined from pressure-distribution data over upper surface of radius flap.